2012

Learning from "Coffee Rings": Ordered Structures Enabled by Controlled Evaporative Self-Assembly

Wei Han
Iowa State University

Learning from "coffee rings": Ordered structures enabled by controlled evaporative self-assembly

by

Wei Han

A dissertation submitted to the graduate faculty

in partial fulfillment of the requirements for the degree of

DOCTOR OF PHILOSOPHY

Major: Materials Science and Engineering

Program of Study Committee:

Zhiqun Lin, Major Professor

Surya K. Mallapragada

Sumit Chaudhary

Xinwei Wang

Malika Jeffries-El

Iowa State University

Ames, Iowa

2012

TABLE OF CONTENTS

Abstract

Drying droplets containing nonvolatile solutes (polymers, microspheres, nanoparticles, single-walled carbon nanotubes, DNA, etc.) on a solid surface have been utilized to yield self-assembled, dissipative structures, possessing dimensions of a few hundred submicrons and beyond. However, these dissipative structures created via evaporation are often irregular and far from equilibrium. Yet for many applications in microelectronics, data storage devices, and biotechnology, it is highly desirable to achieve surface patterns that have a well-controlled spatial arrangement. To date, only a few elegant studies have centered on establishing a means of harnessing the drying process of an evaporating droplet to produce highly regular structures. Among them, controlled evaporative self-assembly (*CESA*) in a restricted geometry stands out as an extremely simple route to creating intriguing one- or two-dimensional structures. In this geometry, the evaporation flux, the solution concentration and the interfacial interaction between the solute and substrate are precisely controlled, thereby producing intriguing, well-ordered structures with high fidelity and regularity. When compared with conventional lithography techniques, surface patterning by controlled solvent evaporation is simple and cost-effective, offering a lithography- and external field-free means of organizing nonvolatile materials into ordered microscopic structures over large surface areas.

Over the past several years, I have crafted a wide range of intriguing and highly regular micro- and nanostructures composed of conjugated polymers, block copolymers, and latex particles, metallocene-containing polymers, etc. enabled by *CESA* in rationally designed “curve-on-flat” geometries. The mechanism of structure formation is elucidated both experimentally and theoretically. Moreover, by applying external magnetic field in conjunction with the solvent evaporative field, *CESA* of magnetic nanoparticles is promoted to yield intriguing asymmetry patterns. Finally, hierarchically structured wrinkles formed within the gradient stripes prepared by *CESA* are systematically

scrutinized. As such, *CESA* represents a state-of-art strategy for crafting highly structured, multifunctional materials and devices for potential applications in optoelectronics, photonics, and biosensors.

CHAPTER 1. INTRODUCTION

Self-assembly, as the name implies, refers to the self-made organizational process of materials into surface patterns or structures in the absence of additional external forces. Self-assembly processes are commonplace phenomena throughout nature and technology, and permeate length scales from the molecular in the microcosm to the planetary in the universe. Self-assembly is one of the few practical strategies for making ensembles of nanostructures, which is also an essential part of nanotechnology. Normally, self-assembly can serve as a tool to fabricate highly ordered, often intriguing structures with potential applications like optical and electronic devices. Self-assembly is common to many systems, from the non-covalent association of organic molecules, colloids and nanoparticles in solution to the growth of semiconductor quantum dots on solid substrates. The precise focus on spontaneous structures or pattern formation bridges the study of distinct components and complex systems.[1, 2] In the self-assembling processes, the interactions of molecular self-assembly include noncovalent or weak covalent interactions, such as van der Waals force, electrostatic, and hydrophobic interactions, hydrogen, and coordination bonds.[2-4] These interactions among individual components is determined by characteristics of components such as shape, surface properties, charge, polarizability, magnetic dipole moment, mass, solubility and so on.[5] Although self-assembly originated in the study of molecules, it is a strategy that is, in principle, applicable at all scales. The challenge lies in organizing components into desired microstructures and assembling them into functional ensembles. Additional external fields such as gravitational

attraction, external magnetic or electromagnetic field,[6, 7] capillary force and electric-field-induced capillary force,[8-10] and entropic interactions [11, 12] are selected and tailored for producing highly ordered and intriguing structures by improving interactions among the components. Among them, evaporative self-assembly has attracted a great deal of attention due to its simplicity and highly reproducibility.

The technique of drying droplets containing nonvolatile solutes (polymers, microspheres, nanoparticles, single-walled carbon nanotubes, DNA, etc.) on a solid surface has been utilized to yield self-assembled, dissipative structures, possessing dimensions of a few hundred submicrons and beyond. Theoretical and experimental approaches to evaporative self-assembly can be divided into several representative categories. The first is "coffee rings", which was first reported by Deegan and based on the mass conservation of solutes upon solvent evaporation. (Figure 1a and b) [13-15] The maximum evaporative loss of solvent at the edge of the droplet triggers the accumulation of solutes and creates a local roughness. As a result, the solutes transport to the edge and pin the contact line (i.e., "stick"), thus forming a coffee ring (Figure 1a). A subset of the coffee ring phenomena is the formation of a set of concentric rings formed by repetitive "stick-slip" motion. "Maragngoni-Benard" convection cells are derived from the temperature gradient induced by fast solvent evaporation. The temperature gradient, in turn, leads to a surface-tension gradient along the droplet free surface, thus inducing a Marangoni (i.e., surface-tension-driven) flow that reverses the coffee-ring phenomenon and produces deposition at the droplet center rather

than the edge. (Figure 1c and d)[16-20] Another category, "Dip coating", consists of the withdrawal of a substrate from a liquid, gravitational draining and solvent evaporation, accompanied by further condensation reactions, thus forming a uniform thin film on the substrate. The film thickness is determined by the competition among viscous force, surface tension and gravity. [21-25]

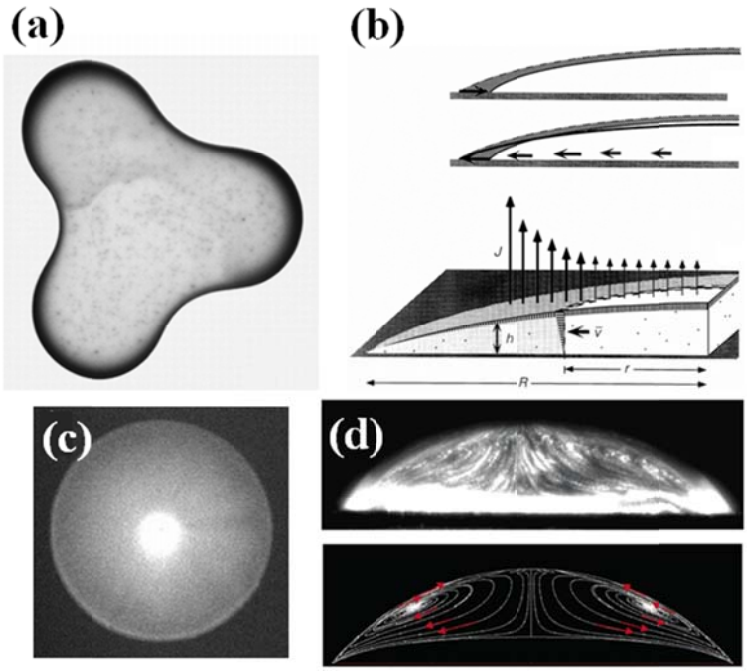

Figure 1. (a): A 2-cm-diameter drop of coffee containing 1 wt% solids has dried to form a perimeter ring, accentuated in regions of high curvature. (b) An increment of evaporation viewed in cross-section. Top one: The result of evaporation without flow: the droplet shrinks. Middle one: The compensating flow needed to keep the contact line fixed. Bottom one: we define the quantities responsible for flow. Vapour leaves at a rate per unit area J(r). The removed liquid contracts the height h(r) vertically, vacating the vertically striped region in a short time Δt .[13] (c) Deposition pattern from a 10 μL droplet of octane containing PMMA particles (1 g/100 mL) deposited on a glass coverslip coated with PFLA. (d): Flow field in a drying octane droplet, top one: imaged experimentally and

bottom one: predicted (Ma=45 800). To observe a clear Marangoni vortex, the illumination plane was moved forward about 0.66 mm from the symmetrical axis of the droplet. [26]

However, the dissipative structures created via evaporation are often irregular and far from equilibrium. Yet for many applications in microelectronics, data storage devices, and biotechnology, it is highly desirable to achieve surface patterns that have a well-controlled spatial arrangement. In this context, in order to take advantage of the extreme simplicity of this nonlithographic, external field-free, top-down technique and exploit its full potentials, the evaporation process that involves a wide range of parameters, including the evaporation flux, the solution concentration, and the interfacial interaction among the solvent, solute, substrate, should be precisely and systemically controlled. To date, only a few elegant studies have centered on the precise control of the evaporation process, including convective assembly in evaporating menisci, controlled anisotropic wetting/dewetting processes, evaporative lithography with a mask, and controlled evaporative self-assembly in confined geometries, to produce ordered and intriguing structures with unprecedented regularity. Among them, controlled evaporative self-assembly in a restricted geometry has been shown as a simple, rational preparation route for the creation of microscopic structures having high fidelity and regularity. It offers a means of organizing materials on the micro- and nano-scale without the need for lithography or an external field over large surface areas using a facile routine.

This introduction aims to be not only a snapshot of the recent development of controlled evaporative self-assembly approaches made during the past years, but also to be employed as a guide to understand the mechanism (i.e., parameters tailored), intriguing structures (i.e., hierarchically organized structures of block copolymers) and their potential applications. Here, we place a special emphasis on controlled evaporative self-assembly in restricted geometries (i.e. constrained solutions). The drying of unconstrained polymer solution that leads to ordered structures will not be discussed here. For detail on this subject the reader is referred to some more comprehensive reviews. [27, 28] This article consists of three main sections. Section 1.1 of this review describes the various systems used to confine the evaporation process and related tailored parameters in these systems. Section 1.2 considers the various nonvolatile solutes (i.e., polymers, DNA, microspheres, etc.) contained within a droplet trapped between the restricted geometries. Their applications are the topic of Section 1.3 Section 1.4 summarizes the importance of the approach and addresses the remaining technological challenges that lie ahead.

Evaporation Process

Basic Principles and Theoretical Background

Drying a sessile droplet on a substrate can be understood and modeled through a basic transport analysis of evaporation and evaporation-induced flow. Therefore, in order to understand the mechanisms of structure formation via controlled evaporative assembly in

confined geometries, lubrication approximations or numerical analysis are desirable to predict the length scales of periodicity, height, and width, which can compare the experimental observations. Although models of evaporating free pure liquid on flat substrates have been developed and reported, few theoretical studies have been performed on a solution containing nonvolatile solute evaporating in confined geometries. In most of case, they followed the "stick-slip" mechanism of evaporative self-assembly in confined geometries: A drop of polymer solution was loaded in a restricted geometry, thus leading to a capillary-held polymer solution, and the evaporation rate is highest at its extremity. As solvent evaporated, loss of solvent at the capillary edge triggered the pinning of the contact line (i.e., "stick"). Thus, the outmost stripe was formed. During the deposition of the solute, the initial angle of the capillary edge decreased gradually due to evaporation of solvent to a critical angle, at which the capillary force (depinning force) became larger than the pinning force. This caused the contact line to jump to a new position (i.e., "slip"), and a new strip was developed. Repeated pinning and depinning cycles of the contact line led to the formation of gradient periodical stripes. (Figure 2)

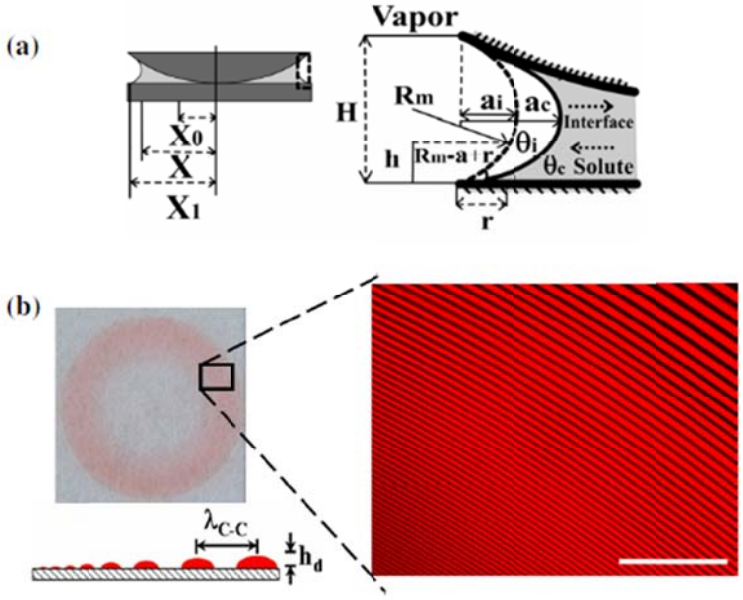

Figure 2. (a) Left: Schematic cross section of a capillary-held solution containing nonvolatile solute placed in a sphere-on-flat configuration. X_1, X, and X_0 are the radii of outermost, intermediate, and innermost rings from the center of sphere/flat contact, respectively. Right: The close-up of the capillary edge marked in the left panel. The parameters used in the calculation are illustrated. (b) The digital image of entire gradient concentric ring patterns formed by the deposition of the solute (i.e., MEH-PPV from the 0:075mg/ml toluene solution) in the geometry in (a). On the right side, a small zone of the fluorescent image of MEH-PPV ring patterns is shown. The scale bar is 200 μm. As the solution front moves inward, rings become smaller and the height decreases as illustrated in lower left schematic.

Choice of Systems

To fully utilize evaporative self-assembly as a simple tool to develop micro- to nanoscale structures for potential technological applications, the evaporation process and associated capillary flow should be delicately controlled. To date, several elegant approaches

have been successfully exploited to create polymer patterns by implementing tailor-made geometry to restrict the solution, which includes two parallel sliding glass substrates,[29, 30] cylindrical tube, two plates with one plate placed at a certain angle to the substrate,[31, 32] two crossed cylindrical mounts, evaporative lithography and "curve-on-flat" geometries, as illustrated in Figure 2. These confined geometries provide a unique environment for remarkable control over the flow within an evaporating droplet, thus regulating structure formation.

Yebu et al. manipulated two parallel plates to controllable constrain the polymer solution, and controlled the speed of the upper sliding plated to produce self-organized, mesoscale polymer patterns (i.e., dots, lines and ladder-like structures) on the stationary lower substrate at the drying edge.[29] The shape and size of the resulting intriguing patterns were highly reproducible and controlled by experimental parameters such as sliding speed and polymer concentration. Higher sliding speed and lower concentration lead to slower evaporation rate, whereas slower sliding speed and higher concentration resulted in fast evaporation rate. Recently, Kim et al. reported the spontaneous, controlled formation of striped patterns of QDs over multiple length scales by regulating the motion of translation stage.[30] Both parallel and crossed multi-component stripe patterns were prepared by controlling the rate and direction of the stage translation. (Figure 3)

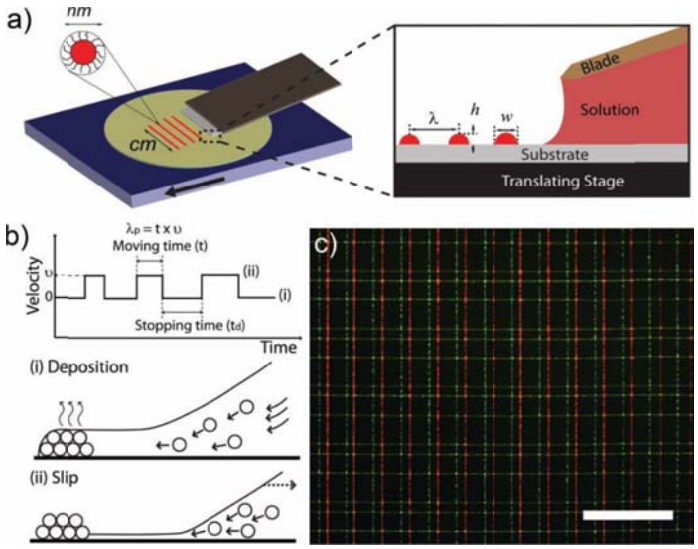

Figure 3. (a) Schematic diagram of the flow-coating apparatus for generating stripe patterns of CdSe QDs on a silicon wafer. (b) The velocity profile of the translation stage for manipulating the stick-and-slip motion of the contact line. Schematic illustration of QD deposition at intermittent stopping times (i) and slipping of the contact line upon stage translation (ii). (c) A fluorescent microscopy image of grid patterns with homo- or hetero-junction configuration at each crossed point generated by a three step flow-coating process. Scale bar, 200μm.

Thin structured micro- and nanoparticle particle layers are rapid and controlled deposited by dragging with constant velocity the meniscus of microliter suspension droplets trapped between two plates placed on one another at certain angles.[31, 32] The coating thickness and structure are controlled by deposition speed and particle volume fraction. Compared to standard dip-coating technique, the coating time and material consumption are markedly decreased. Coatings of tens of square centimeters were deposited onto microscope slides from microliter volumes in just minutes.[31]

The capillary tube-induced confinement created a fluidic column in a cylindrical capillary placed vertically or horizontally thus yielding bands of particle aggregates along the capillary. [33, 34] The capillary force was dictated by the radius of curvature that was at least an order of magnitude small than the capillary length. The confined space in the capillary effectively regulates the evaporation rate of the fluidic column, which in turn impacts the kinetics of colloidal crystallization. Distinctive features of the colloidal crystalline structures observed in the study were the band width and the periodic spacing along the capillary, both of which increased with an increase of colloidal concentration or with a decreased time for a given initial concentration.[33] (Figure 4)

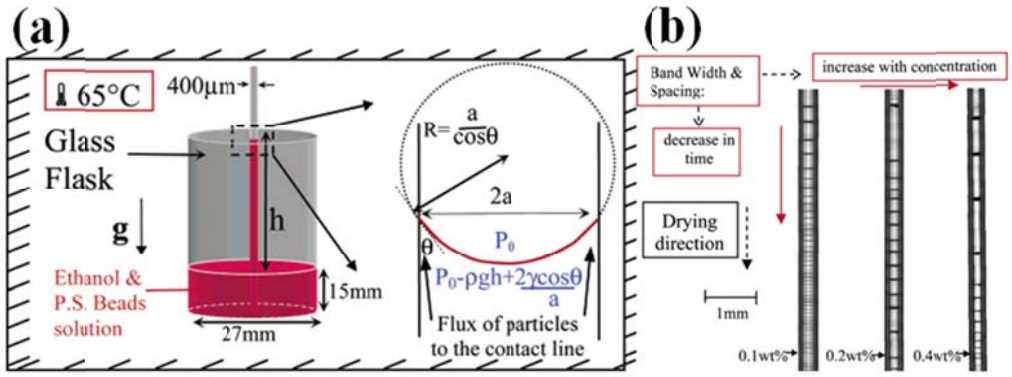

Figure 4. (a) Experimental setup: a glass capillary of 400μm diameter is maintained vertically in an open glass bottle containing a solution of ethanol and polystyrene particles (0.5 μm diameter). To the right, we indicate geometrical and physical parameters needed to understand the force balance in the neighborhood of the meniscus.(b) Ring patterns observed along three capillaries for three different concentrations of the particles. The black lines represent particle deposits, and the solid arrows indicate the decrease of the band width and spacing, respectively, in time and as the initial concentration increases. Each picture was produced by assembling successive microscope images of portions of the capillary.

The use of restricted geometry comprising two crossed cylinders with freshly cleaved single crystals of mica also produced well-ordered patterns of high fidelity and regularity, as shown in Figure 4.[35] With highest evaporation rate at the extremity, a capillary bridge leads to periodically repetitive pinning-depinning cycle of the contact line, thus forming hundreds of concentric rings over large areas. The observed micrometer-size rings are governed by the imposed geometry, the solution concentration, and the solvent properties. (Figure 5)

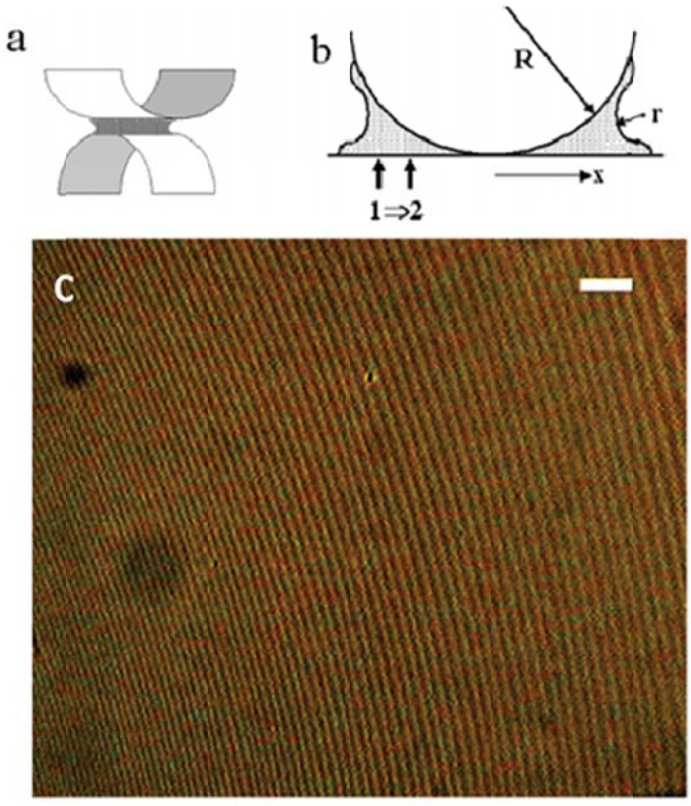

Figure 5. (a) A droplet containing solute in volatile solvent is placed in a confined geometry, in this example between crossed cylinders of freshly cleaved single crystals of mica. (b), the crossed cylinders are brought together such that a capillary bridge forms with evaporation rate highest at the extremity. This leads to unstable pinning-depinning of the contact line, which moves toward the center of the mica/mica contact as time elapses with resulting complex pattern formation, as described

in the text. (c) Optical micrograph of gradient concentric ring patterns formed by deposition of MEH-PPV in the geometry shown in Figure a and b. The white scale bar is 50 μm.

A novel approach named evaporative lithography was utilized to pattern colloidal films by manipulating evaporative deposition of polymers beneath a mask, which induces periodic variations between regions of hindered and free evaporation.[36, 37] The colloidal patterns can be regulated by varying the separation distance between the mask and underlying film, colloid volume fraction and mask design.

It has demonstrated that concentric rings of polymer of high regularity were formed naturally and spontaneously via controlled, repetitive "stick-slip" motion of the three-phase contact line when a drop of polymer solution was confined between a curved upper surface and a flat substrate (curve-on-flat geometry), resulting in a capillary-held polymer solution.[38-47] The evaporation is restricted to occur only at the capillary edge due to the geometrical constraint and the evaporation rate is highest at its extremity. As a result, repeated pinning and depinning cycles of the contact line lead to the formation of gradient periodical stripes with regular spacing.[47] Other ordered yet complex structures including spokes, fingers, serpentines and hierarchically organized structures can also be produced.[38, 39, 41] (Figure 6)

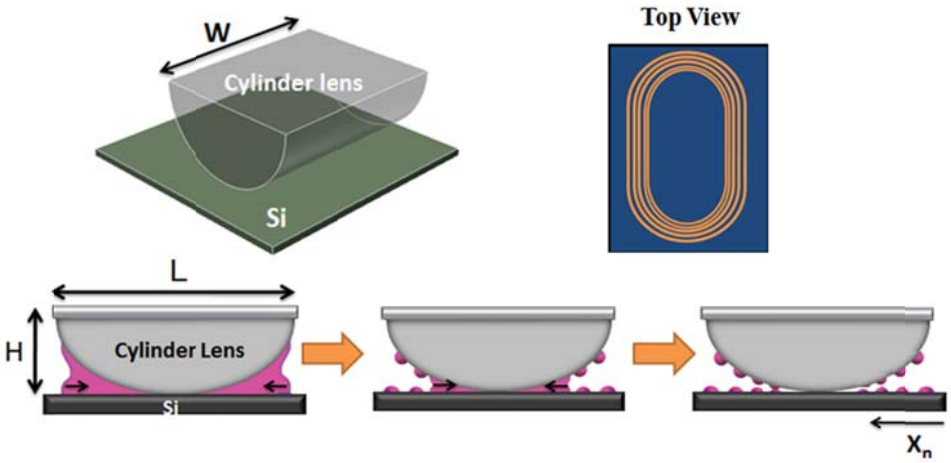

Figure 6. Representation of the formation of gradient CBCP stripes. A drop of polymer solution was trapped in a confined geometry consisting of a wedge-shaped lens on a flat Si substrate, forming a capillary-held solution (side view). H, L, and W are the height, length, and width of a cylinder len. As the contact line of trapped solution retracted toward the wedge/Si contact center by successive controlled "stick-slip" motions, gradient stripes over large areas formed (central and right panels; second row). The black arrows mark the movement of the solution front toward the wedge/Si contact center. Xn indicates the position toward the contact center.

Parameters

Concentration Effect: Among all preparation variables, the solution concentration remains as one of the most important and heavily studied. In confined geometries, for example, the "curve-on-flat" geometry and the cylindrical tube, the low initial concentration causes a less deposition of solutes (i.e., lower height), corresponding to a larger critical contact angle. The pinning time of the contact line is therefore shorter, which in turn leads to a smaller amount of volume loss of solvent during pinning. Thus, a smaller pull of the contact line to next position is resulted in (i.e., smaller distance between the neighboring deposits).[48, 49] Different concentrations may also give rise to different intriguingly

ordered structures, for example, dots, stripes and ladders governed by different mechanisms, i.e., dewetting, "stick-slip" motion, and fingering instability, respectively.[50]

Solvent Effect: The choice of solvent is also of key importance in regulating the structure formation. Fast solvent evaporation enhances the convective force due to evaporative cooling, thereby forming fingering instabilities, convection cells, fractal branches, and so forth. By contrast, slow solvent evaporation suppresses instabilities, thus yielding highly ordered patterns. It is worth noting that the use of mixed solvents may trigger heterogeneous evaporation of solutions, which promotes the formation of intriguing complex structures in confined geometries.[51] Notably, to facilitate the removal of solvent, a steady flow of gas can be introduced to the confined geometry, thus increasing the evaporation rate.[52]

Composition Effect: A wide spectrum of soft materials of different chemical structures (e.g., amorphous, rubbery, and semicrystalline polymers, as well as conjugated organic molecules and polymers) and inorganic nanomaterials of different types, sizes, and shapes (e.g., nanoparticle, nanorods, tetrapods, disk-like particles, and spherocylinders) can be utilized to self-assemble into a variety of regular isotropic or anisotropic microstructures or nanostructures (e.g., nanowires and nanofibers) influenced by the nature of materials (e.g., strong intermolecular π-π interaction[52]) upon the confined evaporation. The ability to process two or more components sequentially[30] or simultaneously[53, 54] to form desirable multicomponent structures has been demonstrated on some occasions. When a drying droplet contains a binary mixture of block copolymer/nanoparticle (i.e., polymer A-b-polymer B/polymer A (or B)-modified nanoparticles) or a ternary mixture of polymer

blend/nanoparticle (i.e., polymer A/polymer B/polymer A (or B)-modified nanoparticles), the synergy of phase separation of polymer blends, co-assembly of surface-functionalized nanoparticles and block copolymers that imparts preferential segregation of nanoparticles within a target block, and the destabilization of polymer mediated by the unfavorable interfacial interaction between the polymer and the substrate during evaporation in confined geometries, may result in appealing complex structures.[51]

Molecular Weight Effect: The variation in molecular weight (MW) of polymers can lead to a pronounced change in the structure formation. At low molecular weight, the viscosity of the solution front is low and the dewetting process occurs. Consequently, no contact line is pinned and a liquid-like thin film ruptures, yielding irregular structures.[42]

Surface Chemistry Effect: The surface hydrophobicity of confined geometries, which is related to the interfacial interaction between the solute and the substrate, will predictably govern the structure formation.[51] By capitalizing on the unfavorable interfacial interaction between the solute and the substrate (i.e., possessing a positive Hamaker constant, A), compelling regular structures may be produced due to the synergy of *CESA* of the nonvolatile solute and its destabilization effectively mediated by the unfavorable solute/substrate interaction.[43] In addition, when the substrate is deliberately chemically modified (e.g., deposited with a functional silane agent), the electrostatic interaction or hydrogen bonding between the solute (e.g., positively charged) and the substrate (e.g., negatively charged) during the evaporation process is invoked, which may facilitate the adhesion of solutes on the substrate, and thus alters the solute deposition.[55, 56]

Patterned Surface Effect: It is not surprising that by patterning the substrate in confined geometries with conventional lithography techniques, for example, creating microscopic or nanoscopic posts of different shapes, parallel trenches, and so forth on the lower flat substrate, the outward flow that carries the solute to the capillary edge would be markedly modified. The polymer chains, such as DNA and conjugated polymer nanowires, may stretch, align, and immobilize in or around the patterns to form striking self-assembled structures. The combination of topographically patterned surfaces in confined geometries (physical heterogeneity) with chemical modification (chemical heterogeneity) may yield even more unexpected structures.[51]

Geometry Effect: The confined geometry can be tailor-made to craft a rich family of surface patterns with controllable and predictable assembly enabled by *CESA*. The variation in size, shape, symmetry, and curvature of confined geometries as well as in the separation distance between two surfaces within a confined geometry will inevitably influence the evaporation process and the associated flow field, leading to interesting patterns with different morphologies. These specialized geometries can be further chemically and/or physically modified to afford even broader range of complex assembled structures with potential applications in microelectronics, optoelectronics, nanotechnology, and biotechnology, among other areas.

Temperature Effect: Heating the lower substrate while keeping the upper surface cool would promote the solvent evaporation and impose a temperature gradient, which induces a Marangoni recirculation in the solution.[26] Drying liquid droplets on the heating substrate has been performed to investigate the dynamics generated by the outgoing matter flow. The Marangoni recirculatory flow

driven by surface-tension gradient could reverse the "coffee ring" phenomenon and produce different deposition patterns.[26] Notably, the use of patterned heating of the substrate may allow rigorous control over temperature profiles, and thus the manipulation of both the flow filed and the structure formation.

External Field Effect: The application of an additional external field (e.g., magnetic field,[7] electric field,[57] and mechanical shear) in conjunction with the solvent evaporative field may stand out as an effective strategy to promote the *CESA* of polymers and colloids. The external electric or magnetic field could make the deposition process more rapid,[32] and thus reducing the number of defects in the formed structures, altering the spacing between them (for example, an increase in $\lambda_{C\text{-}C}$ on one side and a decrease of it on the other side when a magnetic field is applied next to the "curve-on-flat" geometry), and potentially achieving improved ordering and orientation of micro- and nanostructures, especially the long range ordering of nanodomains when block copolymers or block copolymer/nanoparticle mixtures are utilized as nonvolatile solutes.[51] In addition to flow coating as noted in Section 2.2, mechanical perturbations (e.g., vertically pumping or laterally oscillatory shearing the upper surface in confined geometries) can be introduced during the *CESA* processes to impart or perturb the deposition patterns by modifying the flow symmetrically (i.e., pumping) or unidirectionally (i.e., oscillatory shearing) at the proper frequency and amplitude. Moreover, when DNA is used, air blowing may be applied in the confined geometry to expedite the evaporation process and align DNA to achieve 1D DNA nanofibers that may exceed several hundred micrometers in length (i.e., molecular combing of DNA[58]).

Structure Formations with Various Materials

In principal, nearly all soluble polymers can be processed by evaporative self-assembly in confined geometries, provided that the molecular parameter (such as molecular weight, pH value and solubility) and process parameter (such as concentration, temperature and humidity) are correctly adjusted. However, in order to make well-ordered and intriguing structures with large areas, some parameters like molecular weight and concentration, as mentioned above, are crucial. For our overview, at first, homopolymers like poly(methyl methacrylate) (PMMA) and polystyrene (PS) are chosen as nonvolatile solution to prepare PMMA and PS toluene solution used in the evaporative self-assembly in confined geometries. Consequently, the solution of block–copolymer (PS-b-P4VP and PS-b-PMMA) have readily assembled into a variety of intriguing hierarchically ordered structures enabled by controlled evaporative self-assembly. In addition, evaporative assembly has been applied to a wide spectrum of organic and inorganic particles of different types, sizes and shapes.

Evaporation of Homopolymers

PS and PMMA are first selected as solutes into the controlled evaporative self-assembly system due to their good toluene-soluble properties. The spontaneous formation of well-organized mesoscale polymer patterns occurs during the course of solvent evaporation by constraining polymer solution in a sphere-on-Si geometry.[43] Gradient concentric rings and self-organized punch-holelike structures were obtained via mediating interfacial interactions

between the homopolymer and the substrate. Concentric rings of semicrystalline polymer poly (ethylene oxide) (PEO) that exhibiting a fibrillar-like surface morphology[59] and the organometallic polymer poly (ferrocenyldimethylsilane) (PFDMS)[45] also fabricated in the sphere-on-flat geometries. It is noteworthy that conjugated polymer regioregular poly (3-hexylthiophene) (rr-P3HT) form hierarchical "snack-skin" like structures under constrained geometries due to the rigid rod-like nature and low Mw of P3HT.[39] (Figure 7)

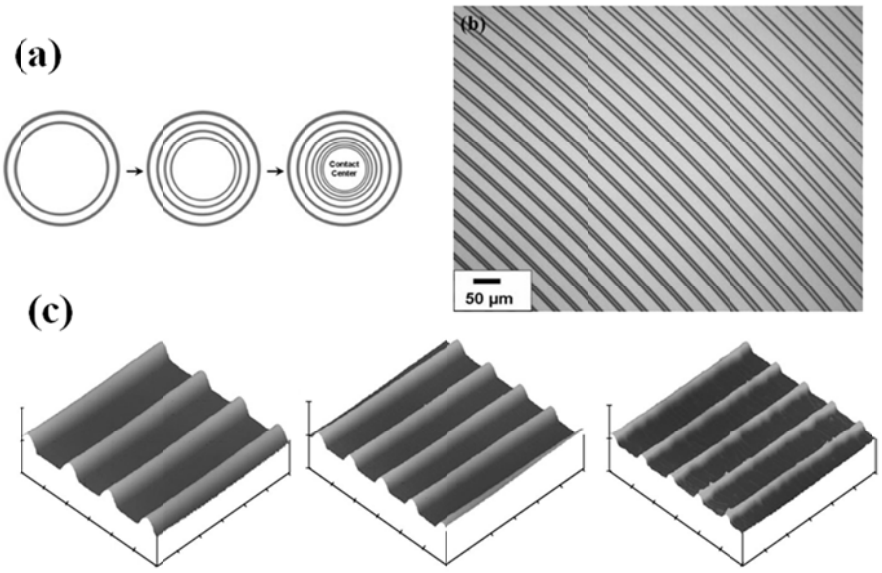

Figure 7. Gradient concentric-ring-pattern formations. a) Schematic drawing illustrating sequential formation of gradient concentric rings of PMMA during the solvent evaporation in the geometry shown in Figure. b) OM image of gradient concentric rings of PMMA. The rings are periodic over a large distance. The concentration of the PMMA toluene solution is c = 0.25 mg/mL^{-1}. The scale bar is 50 μm. c) 3D AFM height images of PMMA rings as the 'stick-slip' motion progressively approaches the center of the sphere/Si contact, corresponding to the stages in (a). The image size is 100μm× 100μm. The z scale is 1000 nm.

Evaporation of Block-copolymers

Diblock copolymers composed of two chemically distinct chains covalently linked at one end are thermodynamically driven to self-assemble into a range of well-ordered nanoscopic domains, for example, spheres, cylinders, and lamellae, depending on the volume fractions of their components. [57, 60-62] Diblock copolymers are widely recognized as attractive building blocks for bottom-up nanofabrication processes, which have potential use in photonics, nanoeletronics, magnetic data storage and biotechnology.[63-65] Combining controlled evaporative self-assembly at the microscopic scale with spontaneous self-assembly at the nanoscopic scale by using a self-assembling block copolymer offers exceptional potential for creating complex, hierarchically organized structures.

For example, evaporation of diblock copolymer polystyrene-b-poly (methyl methacrylate) (PS-b-PMMA) (Figure 8) confined in a spere-on-flat geometry yields concentric serpentine microstructures over large areas (see Figure). Selective solvent vapor annealing then transforms these microstructures into a macroscopic patterns of regularaly arranges microporous mesh arrays, while at the same time forming domains of nanoscopic cylinders of diblock copolymer.[41](See Figure) Moreover, asymmetric comb block copolymer (CBCP) has also been used to produce CBCP nanocylinders vertically or horizontally to the substrate within the microscopic patterns, depending on the duration of solvent vapor annealing.[38] (Figure 9) These highly ordered structures have potential applications in

electronics, optics and nanotechnology, and serve as a useful platform to study cell motility and adhesion.

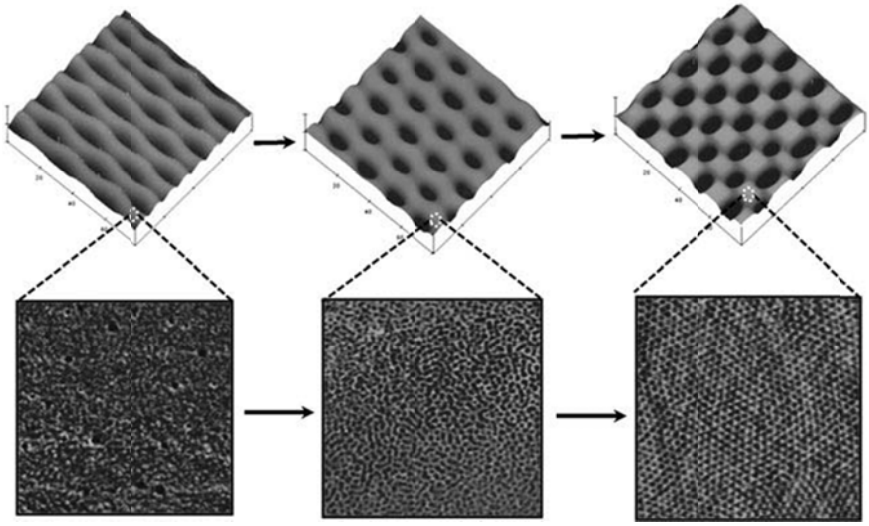

Figure 8. Evolution of regular PS-b-PMMA serpentines to hierarchically woven mesh arrays by acetone vapor annealing. Upper panels: AFM height images: 0 (left), 5 (center), and 12 h (right). Scan size=80x80 μm^2.Lower panels: Close-up AFM phase images from the surface of PS-b- PMMA patterns at each solvent annealing stage shown in the upper panels. Scan size=2x2μm^2. The originally disordered, almost featureless surface topology (left) transforms into well-ordered PS nanocylinders, which appear dark in the phase image and bright in the height image. These nanocylinders are oriented vertically to the film surface (right) over the entire area of regular arrays.

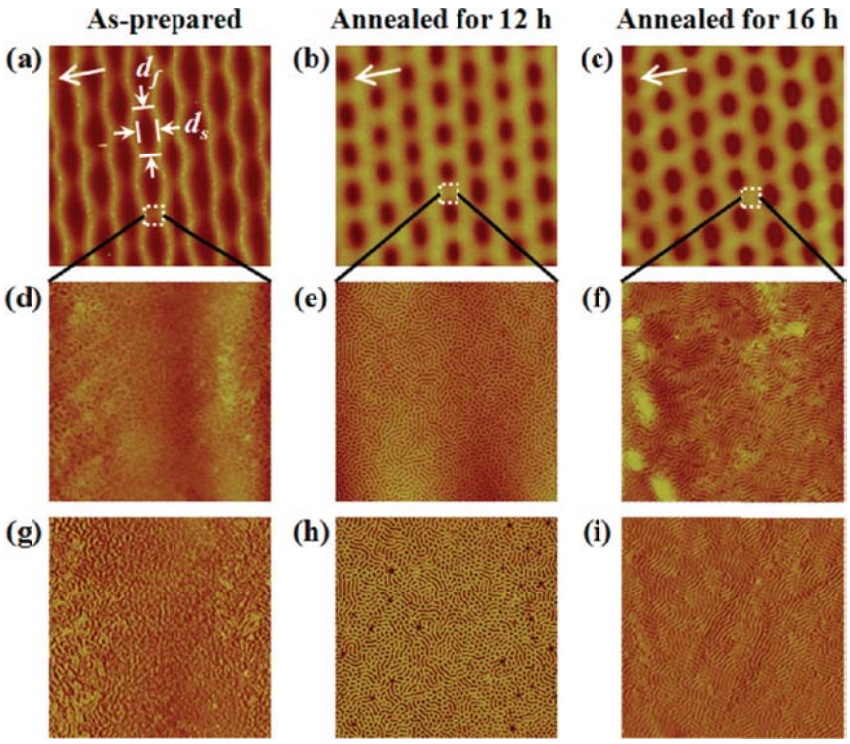

Figure 9. Morphological evolution from jagged stripes to ellipsoidal microporous mesh arrays as a function of THF-vapor annealing time: first column, as-prepared; second column, annealed for 12 h; third column, annealed for 16 h. (a-c). Scan size 60 × 60 μm^2. (d-i) Morphological evolution of CBCP nanodomains within the stripes and ellipsoidal microporous meshes. Transition from nearly featureless morphology to mixed morphologies of vertical and parallel nanocylinders and to almost exclusively parallel nanocylinders was observed. Scan size (d-i) 5 × 5 μm^2

Evaporation of Quantum dots and Latex Particles

Quantum dots (QDs) are highly emissive, spherical, inorganic nanoparticles a few nanometers in diameter. They provide a functional platform for a new class of materials for use in light emitting diodes (LEDs), photovoltaic cells, and biosensors. [66-68] When a drop of CdSe/Zns in toluene loaded and evaporated in a confined geometry, two main types of

pattern formations (concentric rings and spokes) are observed, depending on whether fingering instabilities of thin film of the evaporating front took place or not.[46] (Figure 10)

Moreover, iron oxides are also chosen as solutes due to their potential applications in magnetic data storage, energy storage and drug delivery. Lin promoted the γ–Fe_2O_3 magnetic nanoparticles into massively ordered concentric rings over large areas. The size and packing of γ–Fe_2O_3 nanoparticles within a microscopic ring were dependent upon the preparation of the γ–Fe_2O_3 nanoparticle toluene solution (different purification method).[69]

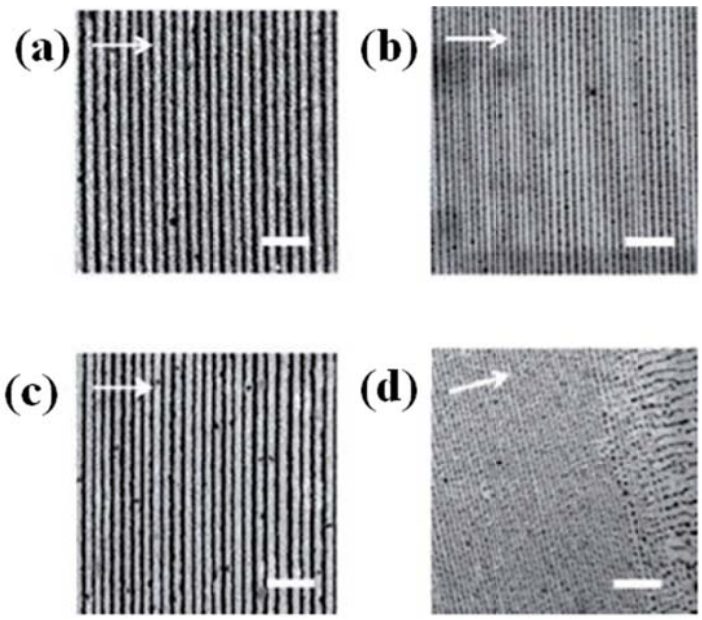

Figure 10. SEM images of concentric rings produced by evaporation-induced self-assembly of 5.5 nm CdSe/ZnS QDs formed by drying 0.25 mg mL^{-1} (a), 0.15 $mgmL^{-1}$ (b), and 0.05 $mgmL^{-1}$ (c and d) toluene solutions. A transition from rings to wirelike structures (c=0.05 $mgmL^{-1}$) is shown on the right side of panel (d). The scale bar is 20 mm in (a–c) and 30 mm in (d). The white arrow on the upper left marks the direction of the movement of the solution front.

Applications

The well-ordered microscopic structures can be used as template for the preparation of other organic or inorganic materials with remarkable regularity. From discussed above, hundreds of gradient concentric polymer rings with remarkable regularity were first spontaneously formed on Si substrate via controlled self-assembly of polymer in a confined geometry (sphere-on-Si). The unprecedented regularity makes these polymer rings intriguing templates for producing concentric metal rings. For example, these concentric rings are exploited as a template to direct the formation of gradient concentric rings of multiwalled carbon nanotubes with controlled density.[70](Figure 11) Also, polymer rings served as templates to direct the formation of concentric Au rings through UV (i.e., on MEH-PPV), thermal treatment (i.e., on PMMA), or selective removal of Au and polymer consecutively.[44] The template methods should readily extend to the fabrication of gradient concentric rings of other metal and metal oxides for biomedical applications with little toxicity. Also, periodical metal rings can serve as etching barriers for transferring patterns into Si substrate by reaction ion etching (RIE).

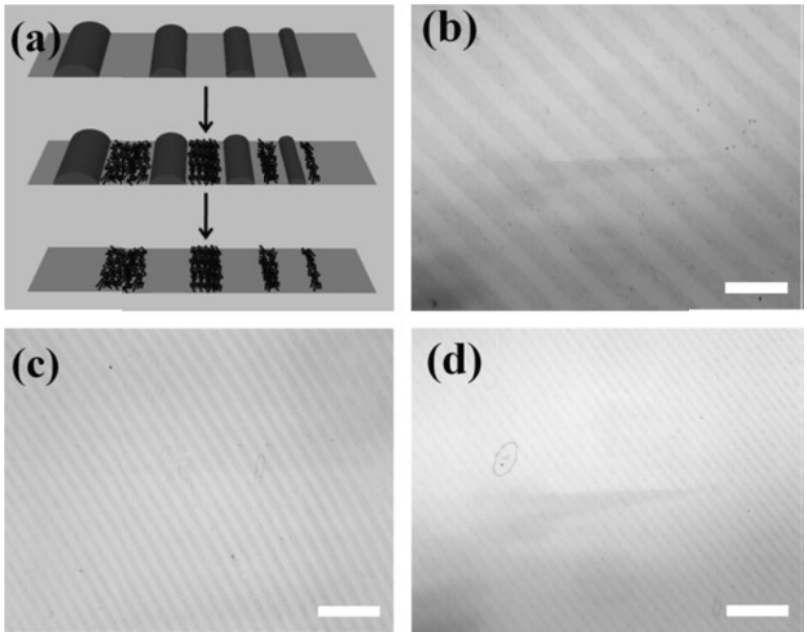

Figure 11. a) Schematic stepwise representation of formation of gradient concentric MWNT rings. Evaporation-induced self-assembly of MEH-PPV rings on Si substrate from MEH-PPV toluene solution in sphere-on-flat geometry. Then a drop of MWNT/PDDA water solution was drop-cast onto the MEH-PPV ring-patterned Si substrate. Upon completion of water evaporation, MWNT rings were formed in between MEH-PPV rings (second panel). After selective removal of MEH-PPV with toluene, gradient concentric MWNT rings can be revealed (last panel). (b–d) Optical micrographs of highly ordered, gradient MWNT rings on Si substrate over large areas produced by template-assisted self-assembly. Scale bars=45μm.

Wrinkles of stiff thin films on compliant substrates have many important applications ranging from stretchable electronics to precision metrology and sensors. Wrinkles usually happed due to the elastic mismatch of soft substrate (i.e., PDMS) and hard materials (i.e., PMMA or Au films). Since the existence of gradient periodical stripes formed under the controlled evaporative self-assembly, the well-ordered structures can sever as good model to

investigate the width and thickness effect of wrinkles. By simply comparing the amplitude and wavelength of wrinkles with different shape, the young's modules can easily calculated.

References

1. Singh, R.; Maru, V. M.; Moharir, P. S., *J. Nonlinear. Sci.* **1998,** *8* (3), 235-259.
2. Whitesides, G. M.; Grzybowski, B., *Science* **2002,** *295* (5564), 2418-2421.
3. Philp, D.; Stoddart, J. F., *Angew. Chem. Int. Ed.* **1996,** *35* (11), 1155-1196.
4. Ball, P., *Oxford University Press* **1999**.
5. Breen, T. L.; Tien, J.; Oliver, S. R. J.; Hadzic, T.; Whitesides, G. M., *Science* **1999,** *284* (5416), 948-951.
6. Ohara, P. C.; Heath, J. R.; Gelbart, W. M., *Angewandte Chemie-International Edition in English* **1997,** *36* (10), 1078-&.
7. Tripp, S. L.; Pusztay, S. V.; Ribbe, A. E.; Wei, A., *J. Am. Chem. Soc.* **2002,** *124* (27), 7914-7915.
8. Bowden, N.; Choi, I. S.; Grzybowski, B. A.; Whitesides, G. M., *J. Am. Chem. Soc.* **1999,** *121* (23), 5373-5391.
9. Bowden, N.; Terfort, A.; Carbeck, J.; Whitesides, G. M., *Science* **1997,** *276* (5310), 233-235.
10. Tang, Z. Y.; Zhang, Z. L.; Wang, Y.; Glotzer, S. C.; Kotov, N. A., *Science* **2006,** *314* (5797), 274-278.
11. Alder, B. J.; Hoover, W. G.; Young, D. A., *J. Chem. Phys.* **1968,** *49* (8), 3688-&.
12. Lee, J. Y.; Shou, Z.; Balazs, A. C., *Phys. Rev. Lett.* **2003,** *91* (13).
13. Deegan, R. D.; Bakajin, O.; Dupont, T. F.; Huber, G.; Nagel, S. R.; Witten, T. A., *Nature* **1997,** *389* (6653), 827-829.
14. Deegan, R. D., *Phys. Rev. E* **2000,** *61* (1), 475-485.
15. Deegan, R. D.; Bakajin, O.; Dupont, T. F.; Huber, G.; Nagel, S. R.; Witten, T. A., *Phys. Rev. E* **2000,** *62* (1), 756-765.
16. Xu, S. Q.; Kumacheva, E., *J. Am. Chem. Soc.* **2002,** *124* (7), 1142-1143.
17. Mitov, Z.; Kumacheva, E., *Phys. Rev. Lett.* **1998,** *81* (16), 3427-3430.
18. Nguyen, V. X.; Stebe, K. J., *Phys. Rev. Lett.* **2002,** *88* (16), 164501.
19. Getling, A. V.; Brausch, O., *Phys. Rev. E* **2003,** *67* (4).
20. Tuval, I.; Cisneros, L.; Dombrowski, C.; Wolgemuth, C. W.; Kessler, J.; Goldstein, R. E., *P. Natl. Acad. Sci. Usa.* **2005,** *102* (7), 2277-2282.
21. Grosso, D.; Babonneau, F.; Albouy, P. A.; Amenitsch, H.; Balkenende, A. R.; Brunet-Bruneau, A.; Rivory, J., *Chem. Mater.* **2002,** *14* (2), 931-939.
22. Takahashi, Y.; Wada, Y., *J. Electrochem. Soc.* **1990,** *137* (1), 267-272.
23. Lu, Y. F.; Ganguli, R.; Drewien, C. A.; Anderson, M. T.; Brinker, C. J.; Gong, W. L.; Guo, Y. X.; Soyez, H.; Dunn, B.; Huang, M. H.; Zink, J. I., *Nature* **1997,** *389* (6649), 364-368.
24. Brinker, C. J.; Frye, G. C.; Hurd, A. J.; Ashley, C. S., *Thin Solid Films* **1991,** *201* (1), 97-108.

25. Terrier, C.; Chatelon, J. P.; Berjoan, R.; Roger, J. A., *Thin Solid Films* **1995,** *263* (1), 37-41.
26. Hu, H.; Larson, R. G., *J. Phys. Chem. B* **2006,** *110* (14), 7090-7094.
27. Jiang, L.; Dong, H.; Hu, W., *Soft Matter* **2011**.
28. Bunz, U. H. F., *Adv. Mater.* **2006,** *18* (8), 973-989.
29. Yabu, H.; Shimomura, M., *Adv. Funct. Mater.* **2005,** *15* (4), 575-581.
30. Kim, H. S.; Lee, C. H.; Sudeep, P. K.; Emrick, T.; Crosby, A. J., *Adv. Mater.* **2010,** *22* (41), 4600-4604.
31. Prevo, B. G.; Velev, O. D., *Langmuir.* **2004,** *20* (6), 2099-2107.
32. Kleinert, J.; Kim, S.; Velev, O. D., *Langmuir.* **2010,** *26* (12), 10380-10385.
33. Abkarian, M.; Nunes, J.; Stone, H. A., *J. Am. Chem. Soc.* **2004,** *126* (19), 5978-5979.
34. Lin, Y.; Balizan, E.; Lee, L. A.; Niu, Z.; Wang, Q., *Angew. Chem. Int. Ed.* **2010,** *49* (5), 868-872.
35. Lin, Z. Q.; Granick, S., *J. Am. Chem. Soc.* **2005,** *127* (9), 2816-2817.
36. Harris, D. J.; Conrad, J. C.; Lewis, J. A., *Philosophical Transactions of the Royal Society a-Mathematical Physical and Engineering Sciences* **2009,** *367* (1909), 5157-5165.
37. Harris, D. J.; Hu, H.; Conrad, J. C.; Lewis, J. A., *Phys. Rev. Lett.* **2007,** *98* (14).
38. Byun, M.; Bowden, N. B.; Lin, Z., *Nano Lett.* **2010,** *10* (8), 3111-3117.
39. Byun, M.; Laskowski, R. L.; He, M.; Qiu, F.; Jeffries-El, M.; Lin, Z. Q., *Soft Matter* **2009,** *5* (8), 1583-1586.
40. Hong, S. W.; Giri, S.; Lin, V. S. Y.; Lin, Z. Q., *Chem. Mater.* **2006,** *18* (22), 5164-5166.
41. Hong, S. W.; Wang, J.; Lin, Z. Q., *Angew. Chem. Int. Ed.* **2009,** *48* (44), 8356-8360.
42. Hong, S. W.; Xia, J. F.; Byun, M.; Zou, Q. Z.; Lin, Z. Q., *Macromolecules* **2007,** *40* (8), 2831-2836.
43. Hong, S. W.; Xia, J. F.; Lin, Z. Q., *Adv. Mater.* **2007,** *19* (10), 1413-+.
44. Hong, S. W.; Xu, J.; Lin, Z. Q., *Nano Lett.* **2006,** *6* (12), 2949-2954.
45. Hong, S. W.; Xu, J.; Xia, J. F.; Lin, Z. Q.; Qiu, F.; Yang, Y. L., *Chem. Mater.* **2005,** *17* (25), 6223-6226.
46. Xu, J.; Xia, J. F.; Lin, Z. Q., *Angew. Chem. Int. Ed.* **2007,** *46* (11), 1860-1863.
47. Xu, J.; Xia, J. F.; Hong, S. W.; Lin, Z. Q.; Qiu, F.; Yang, Y. L., *Phys. Rev. Lett.* **2006,** *96* (6).
48. Abkarian, M.; Nunes, J.; Stone, H. A., *J. Am. Chem. Soc.* **2004,** *126*, 5978-5979.
49. Xu, J.; Xia, J. F.; Hong, S. W.; Lin, Z. Q.; Qiu, F.; Yang, Y. L., *Phys. Rev. Lett.* **2006,** *96* (6), 066104.
50. Yabu, H.; Shimomura, M., *Adv. Funct. Mater.* **2005,** *15*, 575-581.
51. Lin, Z., *Journal of Polymer Science Part B: Polymer Physics* **2010,** *48* (24), 2552-2557.
52. Wang, Z.; Bao, R.; Zhang, X.; Ou, X.; Lee, C.-S.; Chang, J. C.; Zhang, X., *Angew. Chem. Int. Ed.* **2011,** *50* (12), 2811-2815.

53. Harris, D. J.; Hu, H.; Conrad, J. C.; Lewis, J. A., *Phys. Rev. Lett.* **2007,** *98*, 148301.
54. Byun, M.; Hong, S. W.; Qiu, F.; Zou, Q. Z.; Lin, Z. Q., *Macromolecules* **2008,** *41* (23), 9312-9317.
55. Chen, J.; Liao, W.; Chen, X.; Yang, T.; Wark, S. E.; Son, D.; Batteas, J. D.; Cremer, P. S., *ACS Nano* **2009,** *3*, 173-180.
56. Ray, M. A.; Kim, H.; Jia, L., *Langmuir.* **2005,** *21*, 4786-4789.
57. Thurn-Albrecht, T.; Schotter, J.; Kastle, C. A.; Emley, N.; Shibauchi, T.; Krusin-Elbaum, L.; Guarini, K.; Black, C. T.; Tuominen, M. T.; Russell, T. P., *Science* **2000,** *290* (5499), 2126-2129.
58. Michalet, X.; Ekong, R.; Fougerousse, F.; Rousseaux, S.; Schurra, C.; Hornigold, N.; van Slegtenhorst, M.; Wolfe, J.; Povey, S.; Beckmann, J. S.; Bensimon, A., *Science* **1997,** *277*, 1518-1523.
59. Byun, M.; Hong, S. W.; Zhu, L.; Lin, Z., *Langmuir.* **2008,** *24* (7), 3525-3531.
60. Cheng, J. Y.; Ross, C. A.; Smith, H. I.; Thomas, E. L., *Adv. Mater.* **2006,** *18* (19), 2505-2521.
61. Ouk Kim, S.; Solak, H. H.; Stoykovich, M. P.; Ferrier, N. J.; de Pablo, J. J.; Nealey, P. F., *Nature* **2003,** *424* (6947), 411-414.
62. Hawker, C. J.; Russell, T. P., *Mrs. Bull.* **2005,** *30* (12), 952-966.
63. Lin, Y.; Boker, A.; He, J.; Sill, K.; Xiang, H.; Abetz, C.; Li, X.; Wang, J.; Emrick, T.; Long, S.; Wang, Q.; Balazs, A.; Russell, T. P., *Nature* **2005,** *434* (7029), 55-59.
64. Maldovan, M.; Thomas, E. L., *Nat Mater* **2004,** *3* (9), 593-600.
65. Genson, K. L.; Holzmueller, J.; Jiang, C.; Xu, J.; Gibson, J. D.; Zubarev, E. R.; Tsukruk, V. V., *Langmuir.* **2006,** *22* (16), 7011-7015.
66. Colvin, V. L.; Schlamp, M. C.; Alivisatos, A. P., *Nature* **1994,** *370* (6488), 354-357.
67. Alivisatos, A. P., *Abstracts of Papers of the American Chemical Society* **2004,** *227*, 060-IEC.
68. Medintz, I. L.; Uyeda, H. T.; Goldman, E. R.; Mattoussi, H., *Nat Mater* **2005,** *4* (6), 435-446.
69. Byun, M.; Wang, J.; Lin, Z. Q., *J. Phys-condens. Mat.* **2009,** *21* (26).
70. Hong, S. W.; Jeong, W.; Ko, H.; Kessler, M. R.; Tsukruk, V. V.; Lin, Z. Q., *Adv. Funct. Mater.* **2008,** *18* (14), 2114-2122.

CHAPTER 2. HIERARCHICAL ORDERING OF PS-B-P4VP MICELLES VIA CONTROLLED EVAPORATIVE SELF-ASSEMBLY

Modified from a manuscript to be submitted

Wei Han, Myunghwan Byun, and Zhiqun Lin*

Abstract

Highly ordered gradient stripes of PS-b-P4VP block copolymer were obtained by combining the microscopic controlled evaporative self-assembly (CESA) of confined microfluid of PS-b-P4VP toluene solution in a "cylinder-on-Si" geometry with spontaneous self-assembly of micellar hexagonal arrays of PS-b-P4VP at the nanometer scale. The order of packed micelles within microstripes could be significantly improved by subsequent THF vapor annealing .The surface reconstruction of micelles led to the formation of nanoporous arrays when immersed in a selective solvent of the pore component. Gold nanoparticles were then selectively deposited into the core of micelles, and eventually forming the hexagonal arrays of gold nanoparticles after removal of polymer templates by oxygen plasma. The formation of gold particle arrays was verified by XPS measurement.

Introduction

Two-dimensional (2D) periodic structures have attracted intense interest owing to their potential applications in optics, photonics, electronics, magnetic materials, and biotechnology.[1-4] Especially, self-assembly in block copolymer system, is a desirable method for fabricating nanopatterns and overcomes the limitation of conventional

technique (i.e. photolithography) in small scale (i.e. small than 30nm). Among a variety of block copolymers, many efforts are focusing on copolymer micelles, which consist of a core of insoluble block and a corona of the soluble block in a selective solvent. Self-assembled block copolymer micelles may serve as a tool for fabricating nanopatterns with the controlled size and shape.[5-8] Such nanopartterns can be used as templates to manipulate inorganic nanoparticles, by simply loading the metal precursors into the micelle core, and reducing them to nanoparitcles, including Au,[9-12] TiO_2,[13] ZnO,[14] Ag,[15] and Pd[8], followed removing polymer matrix via oxygen plasma or UVO treatment. However, depositing nanoparticles effectively in ordered arrays on a solid substrate over large areas cannot be easily achieved. In order to confine the self-assembly process within two-dimensional structure, some reports focused on combining top-down micro-patterning techniques, such as photolithography and e-beam lithography, with the micelle process to create well-ordered arrays of inorganic nanoparticles. [16-18] However, these kinds of methods involve high processing and maintenance costs and require an iterative, multistep procedure that makes the structure formation process more complex and less reliable.

Drying-mediated self-assembly of a solution droplet containing nonvolatile solutes (i.e. nanoparticles, colloids, and polymers) is an emergent surface patterning techniques for potential application in optical, microelectronics, and sensory devices.[19-23] However, only a few studies have focused on precise control (i.e. evaporation flux, solution concentration and interfacial interaction) of the evaporation process to produce such highly ordered structures. Controlled evaporative self-assembly (CESA) in a restricted geometry has been shown to create complex deposit patterns with unprecedented

regularity.[24-31] The surface patterning by controlled solvent evaporation is simple and cost-effective, which offers a lithography- and external-field-free means to organize nonvolatile materials into ordered microscopic structures over large surface area using a facile and simple routine.

Herein, we demonstrate a simple route to prepare well-ordered polystyrene-block-poly (4-vinylpyridine) (PS-b-P4VP) diblock copolymer stripes with large areas via controlled evaporative self-assembly in a confined geometry (i.e. Cylinder-on-Si geometry). By annealing the PS-b-P4VP in solvent vapor (i.e. THF), the lateral order of PS-b-P4VP micelles is evidently enhanced. Immersion in a preferential solvent for P4VP (i.e. ethanol) may induce the surface-reconstruction of micelles, resulting in the well-ordered nanoporous arrays here. Gradient strips were fabricated with PS-P4VP micelles having $HAuCl_4$ in the P4VP core. The polymer template can be removed with oxygen plasma, which also allows the metal salt to be reduced to the metallic state, thus forming the gradient stripes of the gold particle arrays.

Experimental Section

Evaporative Self-Assembly of the PS-b-P4VP toluene Solution in a Cylinder-on-Si Geometry. Polystyrene-block-poly (4-vinylpyridine) (PS-b-P4VP; number average molecular weight: PS=41.0 $kgmol^{-1}$, P4VP=24.0 $kgmol^{-1}$; Polydispersity=1.09; Polymer Source, Inc.) was dissolved in toluene at a concentration of 0.1 $mgmL^{-1}$ and purified with 200 nm polytetrafluoroethylene (PTFE) filters. The cylinder lens (L=9.5mm, H=4.0mm, W=11.0mm, Figure 12b) and silicon substrate were used as the upper and lower surface, respectively, to construct a confined geometry. The silicon substrates were cleaned with a

mixture of sulfuric acid and Nochromix, then rinsed extensively with deionized (DI) water and blow-dried with N_2. The cylinder-on-Si geometry was placed in a sealed chamber to minimize possible air convection and maintain constant temperature during the evaporation process.

Surface Reconstruction via Vapor Annealing. The regular PS-b-P4VP patterns formed on the Si substrate were exposed to Tetrahydrofuran (THF) vapor for a certain period of time (i.e. 6 hours) in a closed vessel to achieve morphological reconstruction of PS-b-P4VP. The small piece of gauze soaked with THF solvent was placed into a 33 cm^3 vessel. The vessel was sealed by Teflon and placed in an argon grove box to avoid temperature and humidity variation.

Preparation of Gold Particles in Block Copolymer Micelles. Tetrachloroauric acid ($HAuCl_4.3H_2O$) was obtained from Sigma and was used as received. $HAuCl_4.3H_2O$ was added into prepared PS-b-P4VP toluene solution in the required amounts given in molar relation to the P4VP units. The molar ratio of Au^{3+}/P4VP units in the final solution is 0.1. The resulting solution was subsequently stirred for more than 72 hours, allowing the Au^{3+} ions adequate time to migrate into the micelle P4VP cores and complex with the pyridine groups of P4VP. Finally, the polymer template was removed by oxygen plasma (Harrick Plasma; PDC-001) at 30W and 300mTorr for 45mins.

Characterization. The surface structures produced on Si substrate were characterized by optical microscopy (Olympus BX51 in the reflection mode) and atomic force microscopy (Dimension 3100 scanning force microscope in the tapping mode (Digital Instruments)). Vista probes (T190) with spring constants 48Nm^{-1} were used as scanning probes. X-ray photoelectron spectroscopy (XPS; PHI 5500) measurements were

performed with Al standard x-ray source (1486.6 eV). The samples were attached to the holder using double stick tape to isolate the charging effects. Patterns of nanoparticles were observed by a field-emission scanning electron microscope (FE-SEM; FEI Quanta 250) operating at 20kv in High Vacuum.

Results and Discussion

The diblock copolymer, PS-b-P4VP was used as a nonvolatile solute and dissolved in toluene at a concentration of 0.1 mg mL^{-1} (See experiment section). Since toluene is a strong selective solvent for PS, PS-b-P4VP copolymers spontaneously assemble into spherical micelles with a soluble PS corona and an insoluble P4VP core in toluene (Figure 12a).[32-34] The PS blocks formed coronae around insoluble P4VP cores to reduce energetically unfavorable interactions with the solvent.[34, 35] A drop of PS-b-P4VP toluene solution was loaded in a restrictedd in Figure 12b), leading to a capillary-held polymer solution, and the evaporation rate is highest at its extremity. As toluene evaporated, loss of toluene at the capillary edge triggered the pinning of the contact line (i.e., "stick"). Thus, the outmost PS-b-P4VP stripe was formed. During the deposition of PS-b-P4VP, the initial angle of the capillary edge decreased gradually due to evaporation of toluene to a critical angle, at which the capillary force (depinning force) became larger than the pinning force.[29] This caused the contact line to jump to a new position (i.e., "slip"), and a new strip was developed. Repeated pinning and depinning cycles of the contact line led to the formation of gradient periodical stripes of PS-b-P4VP (lower right panel in Figure 12b, on Si substrate).

After the evaporation completed, highly ordered gradient periodical stripes, persisting toward the cylinder/Si contact center, were obtained over the entire surface of the cylinder and Si except the region where the cylinder was in contact with Si. Three typical OM images at different radial distance, X_n (i.e., X_1, where X is the distance from the cylinder/Si contact center, Figure 12b) are shown in Figure 13. The use of confined geometry created highly ordered stripes over large areas. It is noteworthy that the width, w, the height of stripes, h, and the center-to-center distance, λ_{C-C} between adjacent polymer stripes were found to decrease with increasing proximity to the contact center (Figure 13, from X_1 to X_3). Close examination of the stripes by atomic force microscopy (AFM) revealed the gradient, which decreased progressively from w=8.2μm, h=74.4nm, and λ_{C-C}=16.2μm (X_1=4500μm) at outmost region to w=4.2μm, h=54.6nm, and λ_{C-C} =11.9μm at the intermediate region (X_2=4000μm)to w=2.7μm, h=35.2nm, and λ_{C-C} =7.6μm at the innermost region (X_3=3500μm). These observations can be attributed to the competition between the linear pinning force and nonlinear capillary force. [29]

In general, the radius of the PS-b-P4VP micelle in toluene can be expressed by [34, 36]

$$\frac{4\pi}{3} R_c^{\,3} = Z N_A \upsilon_0 \qquad (1)$$

where υ_0 is the molar volume of core monomers, Z is the aggregation number, which defined by $Z = Z_0(N_A^{\,\alpha} N_B^{\,-\beta})$. N_A, N_B are the degree of polymerization of the insoluble core (P4VP) and the soluble corona block (PS), respectively. The experiment value of $Z = 1.66$, $\alpha = 1.93$, $\beta = 0.79$ were reported particularly for the PS-P4VP/toluene system.[34, 36] The calculated radius of PS-b-P4VP micelle in our system is 17.2nm. Thus,

from the height profile in Figure 14c, 3f and 3i, the PS-b-P4VP strips in the region of X_1, X_2 and X_3 are trilayer (h=74.4nm), bilayer (h=54.6nm), and monolayer (h=35.2nm), respectively (Figure 14c,f,i). Large value of h implies a longer pinning time of micelles at the three-phase contact line, and large amount of micelles transforming to the contact line. During the course of solvent evaporation, with the meniscus moving inward, fewer micelles remain to pinning at the contact line, thus making lower height of stripes, finally, getting the monolayer from the innermost region. From AFM images of micelles in each layer (See supporting information, Figure S1), micelles in the bottom layer (Figure S1a, d, f) have the diameter of 35.6nm, which is consistent with the calculation results. However, in the upper layer (Figure S1b, c, e), the micelles become "smaller" (27.2nm) because of the upper layer micelles enchasing into the bottom ones, thus making them "smaller" in AFM images. This is also to explain why the heights of bilayer and trilayer are smaller than twice and thrice of monolayer, respectively. The axially symmetric cylinder-on-Si geometry provides a unique environment for controlling the flow within an evaporating droplet, which in turn regulates the structure formation.[24-29, 37] Later on we will focus on the monolayer stripes in the innermost region. It is also of interest to note that the gradient PS-b-P4VP stripe patterns described here were highly reproducible.

When the as-prepared PS-b-P4VP stripes exposed to the vapor of tetrahydrofuran (THF), the regularity of hexagonal order of PS-P4VP micelles improved significantly. After six hours of exposure vapor annealing under argon at room temperature, a hexagonal array of micelles with significantly enhanced lateral order was obtained, confirmed by a Fourier transformed pattern of white boxed area, as shown in Figure 15c. After vapor annealing, the average pore diameter decreased from 35.2nm to 31.8nm, and

the distribution of diameter of the solvent-annealed micelles was sharpened, compared to the as-prepared stripes with broad size distribution of the micelles (Figure 15e). The reduced diameter of the micelles could be caused by reduction of the aggregation number of copolymer molecules per micelle during THF annealing. Since P4VP has better solubility in THF than toluene, the redistribution of copolymer chains may occur during the vapor annealing, thus achieving the equilibrium state of micelles with smaller size, shaper distribution and highly packed order.[18, 38] We note that the hexagonal order of micelles in the stripes was still short-ranged and also had less ordered than that of a spin-coated film.[5, 7, 16] This is presumable due to the defects existing in the stripes during the evaporative self-assembly process, while spin-coat, an extremely fast solvent evaporation case, could enhance better formation of compact monolayer of micelles, thus making long-ranged ordered micelles easily.[39]

When the stripes were immersed in ethanol for 20mins, a good solvent for P4VP and a nonsolvent for PS, surface reconstruction of the stripes was observed with ordered arrays of nanoscopic pores. (See supporting information, Figure S2). Here, P4VP cores were swelled by ethanol and then diffused to the top of the PS matrix, leaving pores at the positions of the P4VP cores[5, 40](schematically illustrated in Figure S2e). This is similar to the result of morphological reconstruction of PS-b-PMMA diblock copolymer by acetone vapor, a preferential solvent for PMMA, in our previous work.[41] It is noteworthy that the reconstruction by the ethanol leading the nonporous would not change the average spacing between the adjacent P4VP cores (45.3 nm), which is similar to the value of starting micelles (44.9 nm). This kind of surface-reconstructed micelles can be used as template via depositing metal nanoparticles into the opening pores.[8]

A variety of nanoparticles can be synthesized with PS-b-P4VP micelles by loading of their precursors to the P4VP cores[18, 32, 33, 42]. The periodic organization of PS-b-P4VP stripes may serve as an intriguing template for producing well-ordered metal stripes. Here, tetrachloroauric acid ($HAuCl_4.3H_2O$) was used as the precursor of gold nanoparticles and was selective loaded into the P4VP core. When mixing the PS-b-P4VP toluene solution with the precursor, the Au^{3+} ions can easily attach to the pyridine groups of P4VP by protonating the pyridine units, through ionic-polar interactions.[11, 42, 43] Again, as shown in Figure 12b, gradient strips were fabricated with PS-P4VP micelles having $HAuCl_4$ in the P4VP core, instead of pure micelles. Figure 16a and Figure 16b show the AFM height images of stripes and micelles before oxygen plasma, respectively, which is similar to the pattern with pure micelles. To fabricate the arrays of gold nanoparticles, the copolymer template containing $HAuCl_4$ precursor was treated with oxygen plasma for 45mins (Figure 16c, 5d). It well known under the effect of oxygen plasma, the Au^{3+} ions were reduced to elemental Au, as well as removal of the organic copolymer template. [9, 18] The location and the order of the pattern will be preserved, as the original pattern of the starter micelles. It is noteworthy the particles (in Figure 16d) had much smaller diameter (9.8 nm), comparing the micelles in Figure 16b (35.2 nm). Moreover, the profiles (Figure 16e-f) give the height variations of the stripes, which were also reduced dramatically. The reduced diameter and height of the pattern is possibly from the densification by removal of P4VP core.[33] However, the spacing of the patterns was almost the same with an average value of 45.8 nm, regardless of template removal or not, thus indicating the original order of micellar arrangement is conserved, even when the polymer matrix is removed. Field Emission Scanning Electron Microscopy (FE-SEM) images of arrays of

gold particles after oxygen plasma are shown in Figure S3. The gold particle arrays, which appear light in the SEM images, coincide with the AFM images. From the SEM image, arrays of discrete gold nanoparticles are clearly observed on large surface areas. To future demonstrate the successful decoration on the P4VP cores, the samples before and after exposure to the oxygen plasma were close investigated by X-ray photoelectron spectroscopy (XPS), as shown in Figure 17. Before oxygen plasma treatment, the core of micelles in the stripes was still loaded with the metal precursor rather than metal particles, thus making peaks of gold elements disappeared (Figure 17a, the top spectrum). After exposure to the oxygen plasma, the characteristic peaks of Au 4d were observed, indicating the appearance of gold elements after the treatment (Figure 17a, the bottom line), which resulting in bare Au nanoparticles on top of the Si substrate. The remaining carbon peak after oxygen plasma (C 1s) may be possible from the organic contamination, when transferring the samples from oxygen plasma to XPS measurement. When we scanned the gradient gold stripes with emphasis on the Au 4f lever (i.e. perpendicular to the stripes, from outmost to innermost region), the intensity of the Au 4f peak was interestingly observed to keep decreasing with the scanning (Figure 17b). The decreasing width, height of the stripes, and the distance between adjacent stripes made the decreasing density of micelles, thus causing the intensity of the Au particles to decrease, and resulting in the decreasing intensity of 4f spectrum, from the outmost region to innermost region. The 3D view of XPS Au 4f spectrum is consistent with the distribution of the stripes with micelles, from the outmost region to the innermost to the blank center area, then to the outmost region on the other side. (See supporting information, Figure S4).

Conclusion

In conclusion, we demonstrate a simple route to fabricate gradient stripes of PS-b-P4VP block copolymers by combine controlled evaporative self-assembly at the microscopic scale with spontaneous self-assembly of micelles at the nanoscopic scale by using PS-b-P4VP block copolymer micelles. Ordered arrays of micelles can be achieved during solvent annealing in THF vapor. By coupling the micelles stripes with referential solvent for the core component (i.e. P4VP), arrays of nanoporous could easily be fabricated. Finally, well-ordered arrays of gold particles were fabricated by using the micelles template, which containing the gold precursor in the P4VP core, after oxygen plasma. It is noteworthy that variety of nanoparticles could be synthesized into the micelles cores, thus making the method a good way to organize these functional nanoparticles in specific arrangement with controllable size and shape in ordered arrays. The block copolymer micelle approach can be a promising solution for many device applications in future.

Figures

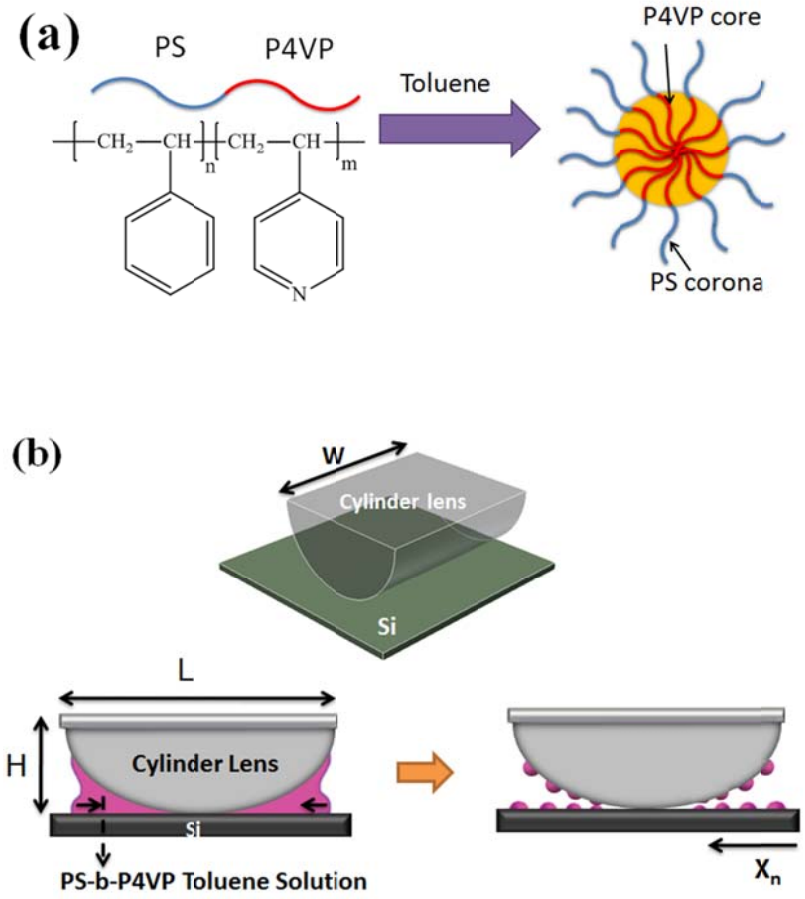

Figure 12. (a) Chemical structure and schematic drawing of the micelle formation of PS-b-P4VP in toluene. (b) Schematic representation of the formation of gradient PS-b-P4VP stripes. A drop of PS-b-P4VP toluene solution was trapped in a confined geometry consisting of a cylinder-shaped lens on a flat Si substrate, forming a capillary-held solution (side view, bottom ones). H, L, and W are the height, length, and width of cylinder lens, respectively. The black arrows mark the movement of the solution front toward the cylinder/Si contact center. X_n indicates the position toward the contact center.

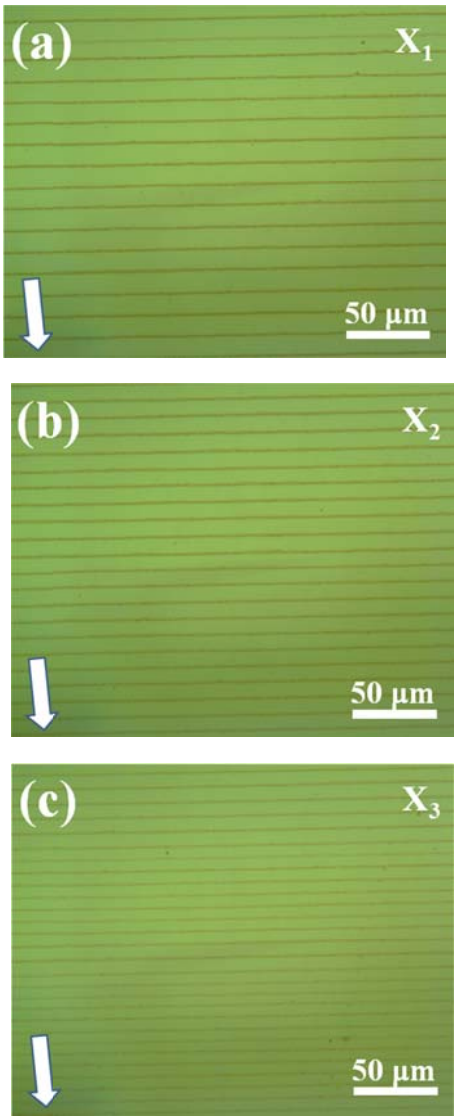

Figure 13. Optical micrograph images of PS-b-P4VP stripes formed by evaporative self-assembly in a cylinder-on-Si geometry at the (a) outermost region (X_1=4500µm); (b) intermediate region (X_2=4000 µm); (c) innermost region (X_3=3500 µm), respectively. Arrays mark the moving direction of the solution front during the course of evaporation.

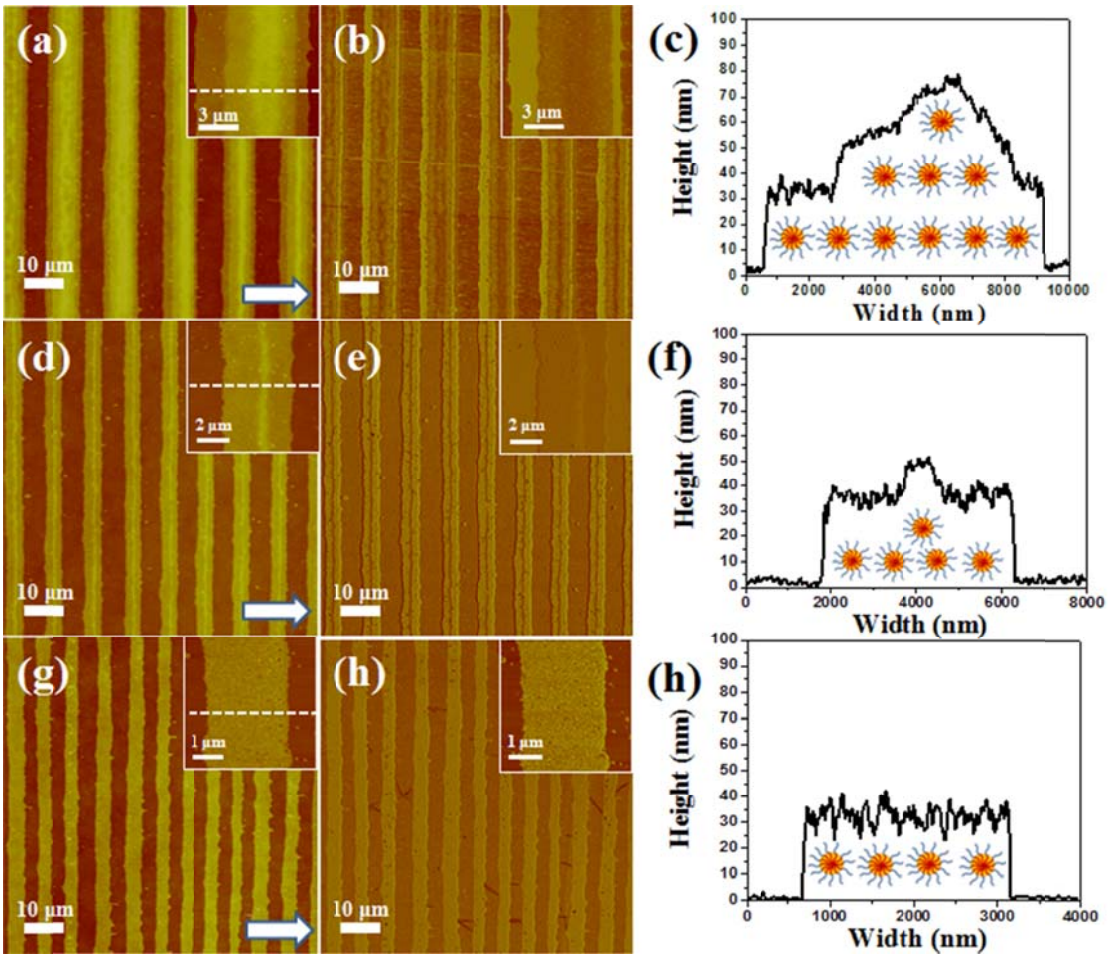

Figure 14. Representative AFM height (a, d, g), phase images (b, e, h) and corresponding height profiles (c, f, i), from the white line in the single strip in insert image in different locations: (a)-(c) Outmost region (X_1). (d)-(f) intermediate region (X_2). (g)-(i) innermost region (X_3). The distance between adjacent stripes, the height of stripes, and the width of stripes gradually decreased at the three regions .Z range is 200nm in all of the AFM height images.

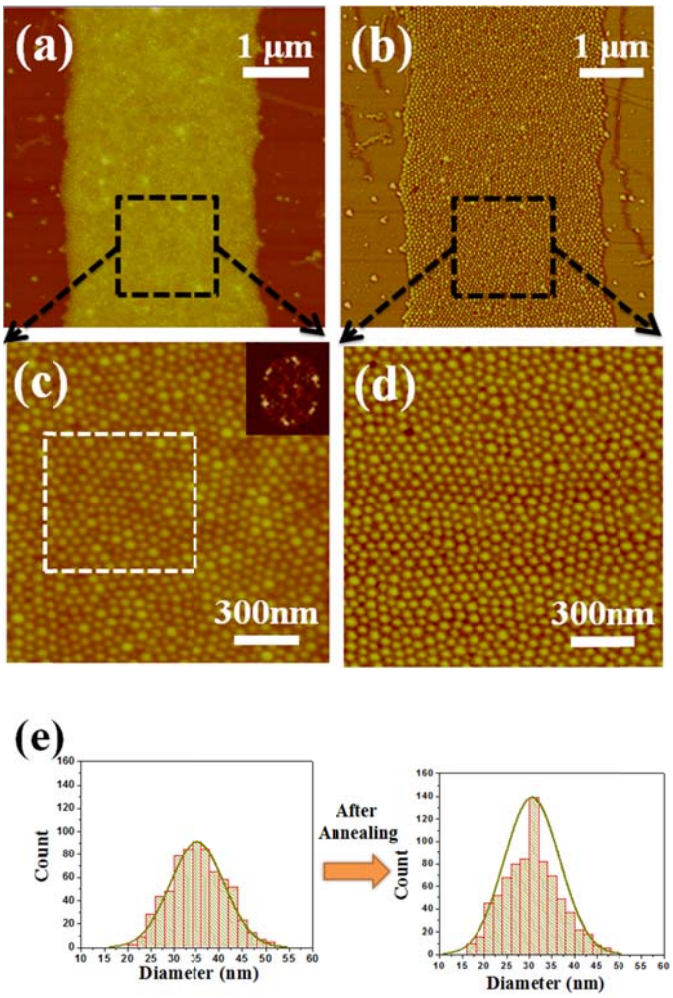

Figure 15. AFM images of the stripes with monolayer micelles in the innermost area after solvent annealing in THF vapor. (a) The height and (b) phase images of the monolayer stripe formed after THF vapor annealing. (c) The height and (d) phase images of micelle formation zoomed in the black boxed area in (a) and (b), respectively. Insert images in (c) is Fourier transformed pattern of white boxed area. (e) Associated pore diameter distribution before (left) and after (right) the vapor annealing. Z ranges are 150nm in (a) and 60 nm in (c), respectively.

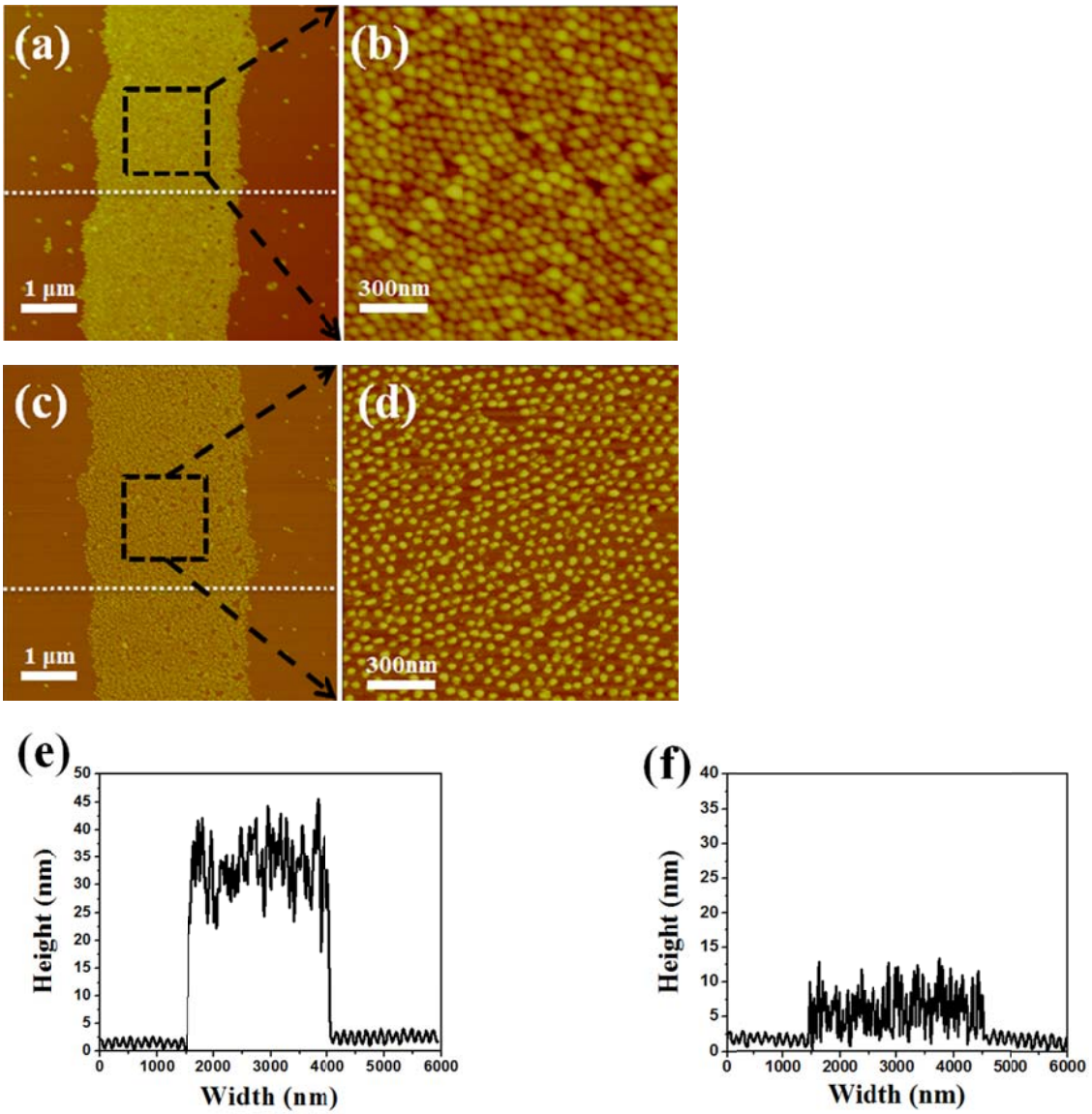

Figure 16. Representative AFM height images of the monolayer stripes and the micelle structure before (a. b) and after (c. d) oxygen plasma. The original order of micellar arrangement is conserved, even when the polymer matrix is removed. Associated height profiles before (e) and after (f) the oxygen plasma along the white dot line in (a) and (c), respectively. Z ranges in (a), (b), (c), (d) are 200nm, 100nm, 50nm and 50nm, respectively.

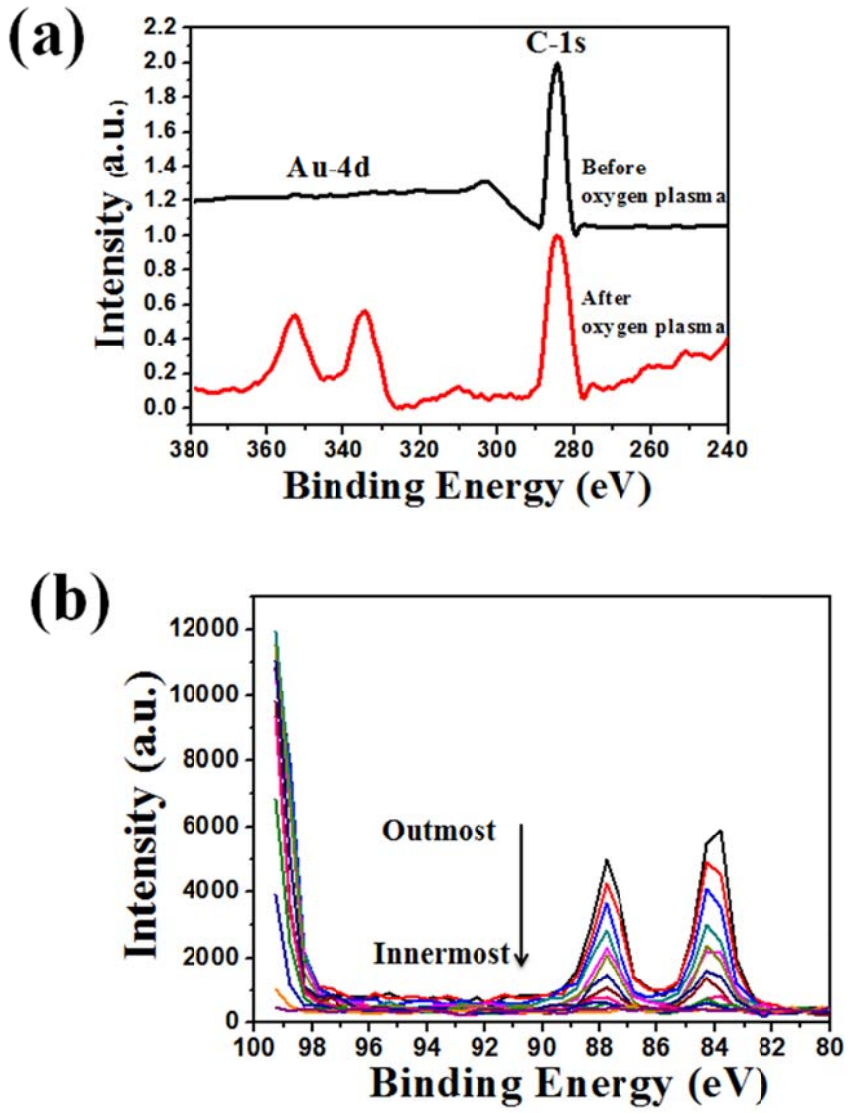

Figure 17. (a) XPS spectra for Au-loaded micelles on top of Si substrate showing the Au 4d, C 1s levels before (top black line) and after (bottom red line) oxygen plasma. (b) XPS spectra for Au 4f level scanning from the outmost region to innermost region.

Supporting Information

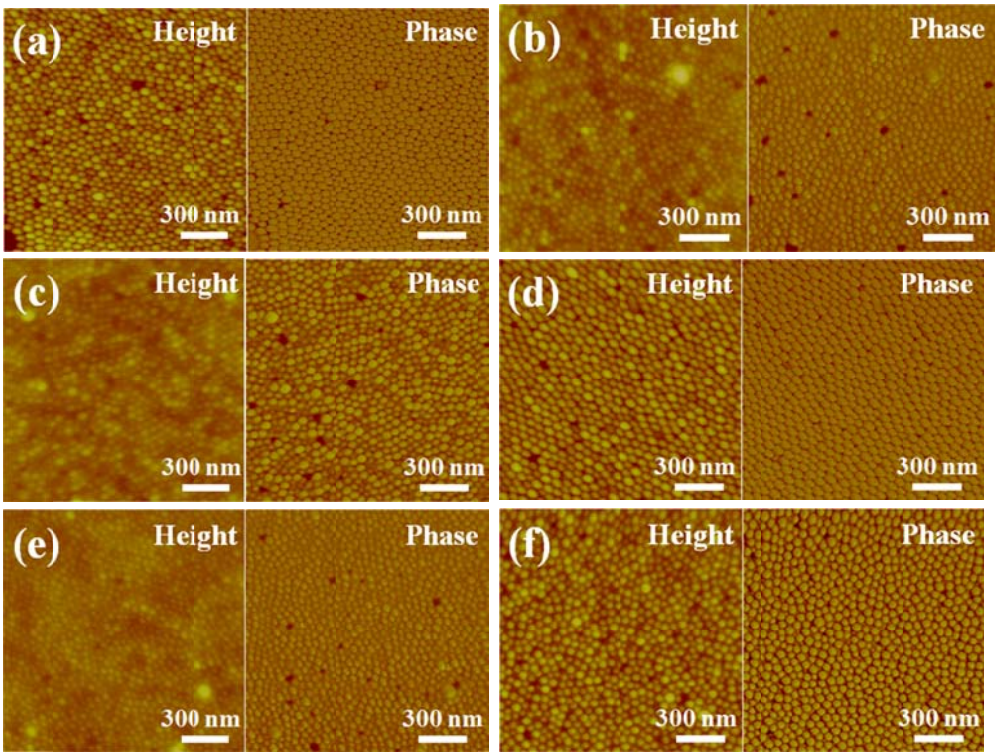

Figure S1. Representation height and phase AFM images of micelles in each layer of stripes in different locations, corresponding to Figure 14. (a) The bottom layer of strips in outmost region (X_1). (b) The middle layer of strips in outmost region (X_1). (c) The top layer of strips in outmost region (X_1). (d) The bottom layer of strips in intermediate region (X_2). (e) The top layer of strips in outmost region (X_2). (f) The single layer of strips in innermost region (X_3). Z range is 100nm for all of the AFM height images.

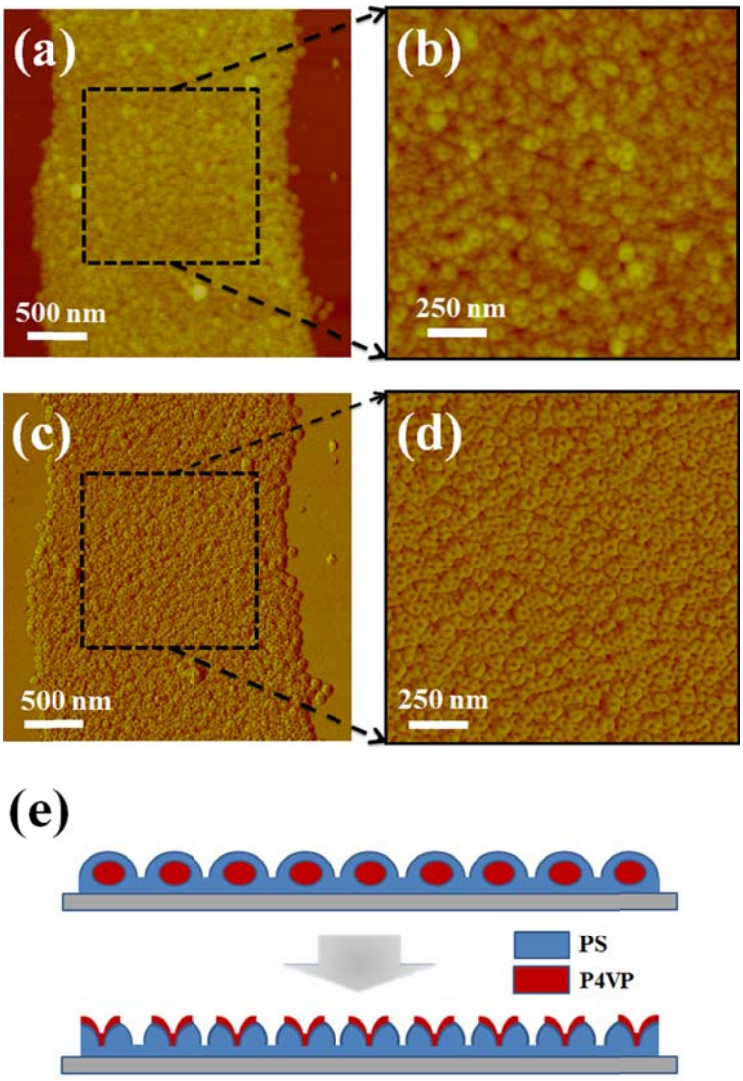

Figure S2. Representative AFM images of a PS-b-P4VP strip after surface-reconstruction by ethanol solvent, a good solvent for P4VP and a nonsolvent for PS. (a) The height and (c) phase images of the monolayer stripe. (b) The height and (d) phase images of micelle formation zoomed in the black boxed area in (a) and (c), respectively. (e) Schematically drawing of the surface reconstruction of PS-b-P4VP micelle films by immersing into ethanol, thus forming ordered stripes of nanoporous. Z ranges are 200nm in (a) and 80 nm in (b), respectively.

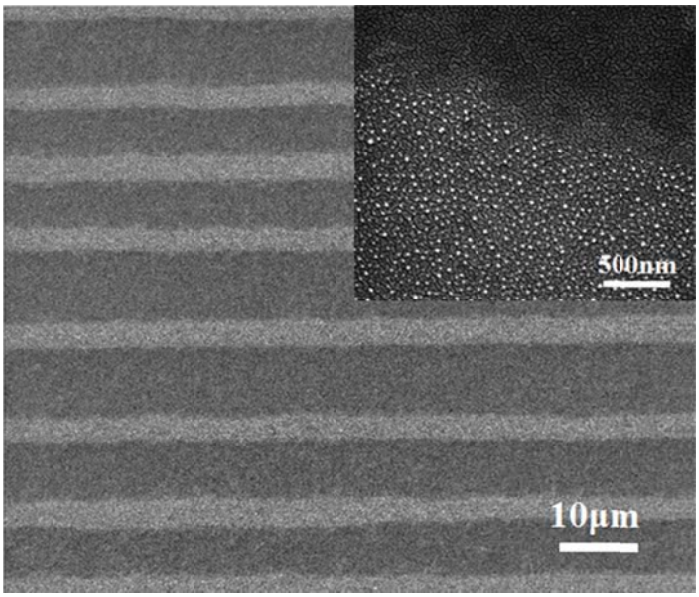

Figure S3. FE-SEM images of arrays of gold particles in the innermost region after oxygen plasma for 45mins. Arrays of discrete gold nanoparticles, which appeared light in SEM image, are clear observed on a large area of surface. Insert image is the detail of gold nanoparticles.

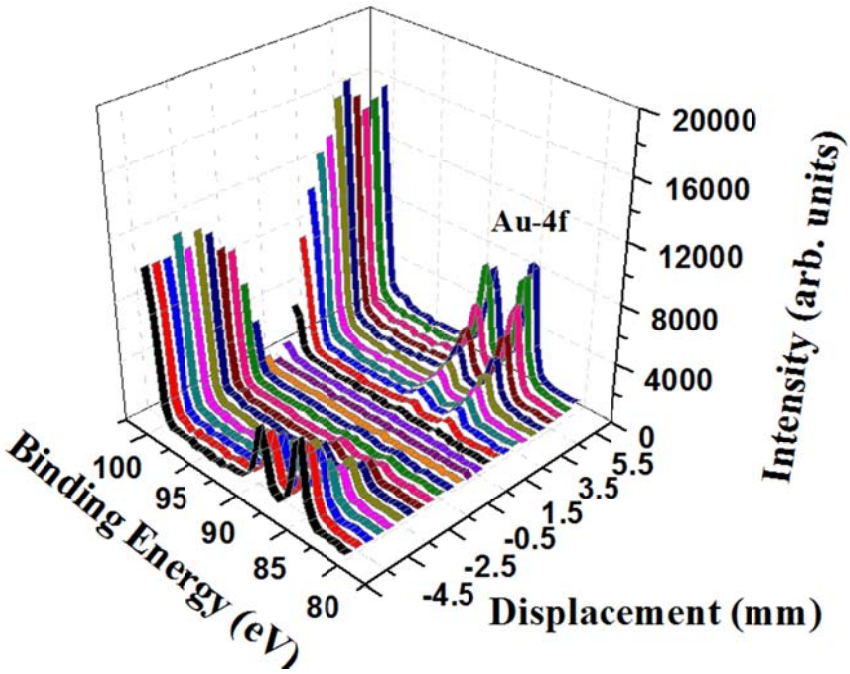

Figure S4. XPS spectrum on Au 4f level, scanned from the outmost region to the innermost to the blank center area, then to the outmost region on the other side, showing the 3-D view of the distribution of gold particles.

References

1. Yabu, H.; Shimomura, M., *Langmuir.* **2005,** *21* (5), 1709-1711.
2. Yabu, H.; Shimomura, M., *Adv. Funct. Mater.* **2005,** *15* (4), 575-581.
3. Jacobs, H. O.; Whitesides, G. M., *Science* **2001,** *291* (5509), 1763-1766.
4. Thurn-Albrecht, T.; Schotter, J.; Kastle, C. A.; Emley, N.; Shibauchi, T.; Krusin-Elbaum, L.; Guarini, K.; Black, C. T.; Tuominen, M. T.; Russell, T. P., *Science* **2000,** *290* (5499), 2126-2129.
5. Park, S.; Wang, J. Y.; Kim, B.; Xu, J.; Russell, T. P., *Acs Nano* **2008,** *2* (4), 766-772.
6. Haryono, A.; Binder, W. H., *Small* **2006,** *2* (5), 600-611.
7. Kim, B. Y.; Park, S. J.; McCarthy, T. J.; Russell, T. P., *Small* **2007,** *3* (11), 1869-1872.
8. Gowd, E. B.; Nandan, B.; Vyas, M. K.; Bigall, N. C.; Eychmuller, A.; Schlorb, H.; Stamm, M., *Nanotechnology* **2009,** *20* (41).
9. Spatz, J. P.; Mossmer, S.; Hartmann, C.; Moller, M.; Herzog, T.; Krieger, M.; Boyen, H. G.; Ziemann, P.; Kabius, B., *Langmuir.* **2000,** *16* (2), 407-415.
10. Park, S.; Wang, J. Y.; Kim, B.; Russell, T. P., *Nano Lett.* **2008,** *8* (6), 1667-1672.
11. Leong, W. L.; Lee, P. S.; Lohani, A.; Lam, Y. M.; Chen, T.; Zhang, S.; Dodabalapur, A.; Mhaisalkar, S. G., *Adv. Mater.* **2008,** *20* (12), 2325-+.
12. Spatz, J. P.; Mossmer, S.; Moller, M., *Chem-eur. J.* **1996,** *2* (12), 1552-1555.
13. Weng, C. C.; Hsu, K. F.; Wei, K. H., *Chem. Mater.* **2004,** *16* (21), 4080-4086.
14. Hwang, W.; Choi, J. H.; Kim, T. H.; Sung, J.; Myoung, J. M.; Choi, D. G.; Sohn, B. H.; Lee, S. S.; Kim, D. H.; Park, C., *Chem. Mater.* **2008,** *20* (19), 6041-6047.
15. Liu, Y. J.; He, L. B.; Xu, C. H.; Han, M., *Chem. Commun.* **2009,** (43), 6566-6568.
16. Park, S.; Kim, B.; Yavuzcetin, O.; Tuominen, M. T.; Russell, T. P., *Acs Nano* **2008,** *2* (7), 1363-1370.
17. Yun, S. H.; Sohn, B. H.; Jung, J. C.; Zin, W. C.; Ree, M.; Park, J. W., *Nanotechnology* **2006,** *17* (2), 450-454.
18. Yoo, S. I.; Kwon, J. H.; Sohn, B. H., *J. Mater. Chem.* **2007,** *17* (29), 2969-2975.
19. Bigioni, T. P.; Lin, X.-M.; Nguyen, T. T.; Corwin, E. I.; Witten, T. A.; Jaeger, H. M., *Nat Mater* **2006,** *5* (4), 265-270.
20. Martin, C. P.; Blunt, M. O.; Pauliac-Vaujour, E.; Stannard, A.; Moriarty, P.; Vancea, I.; Thiele, U., *Phys. Rev. Lett.* **2007,** *99* (11), 116103.
21. Khanal, B.; Zubarev, E., *Angewandte Chemie* **2007,** *119* (13), 2245-2248.
22. Rabani, E.; Reichman, D. R.; Geissler, P. L.; Brus, L. E., *Nature* **2003,** *426* (6964), 271-274.
23. Mitov, Z.; Kumacheva, E., *Phys. Rev. Lett.* **1998,** *81* (16), 3427.
24. Hong, S. W.; Xu, J.; Lin, Z. Q., *Nano Lett.* **2006,** *6* (12), 2949-2954.
25. Hong, S. W.; Xia, J. F.; Byun, M.; Zou, Q. Z.; Lin, Z. Q., *Macromolecules* **2007,** *40* (8), 2831-2836.
26. Hong, S. W.; Giri, S.; Lin, V. S. Y.; Lin, Z. Q., *Chem. Mater.* **2006,** *18* (22), 5164-5166.
27. Hong, S. W.; Xia, J. F.; Lin, Z. Q., *Adv. Mater.* **2007,** *19* (10), 1413-+.
28. Xu, J.; Xia, J. F.; Lin, Z. Q., *Angew. Chem. Int. Ed.* **2007,** *46* (11), 1860-1863.
29. Xu, J.; Xia, J. F.; Hong, S. W.; Lin, Z. Q.; Qiu, F.; Yang, Y. L., *Phys. Rev. Lett.* **2006,** *96* (6).
30. Byun, M.; Bowden, N. B.; Lin, Z., *Nano Lett.* **2010,** *10* (8), 3111-3117.
31. Byun, M.; Laskowski, R. L.; He, M.; Qiu, F.; Jeffries-El, M.; Lin, Z. Q., *Soft Matter* **2009,** *5* (8), 1583-1586.
32. Forster, S.; Antonietti, M., *Adv. Mater.* **1998,** *10* (3), 195-195.
33. Sohn, B. H.; Choi, J. M.; Yoo, S. I.; Yun, S. H.; Zin, W. C.; Jung, J. C.; Kanehara, M.; Hirata, T.; Teranishi, T., *J. Am. Chem. Soc.* **2003,** *125* (21), 6368-6369.

34. Forster, S.; Zisenis, M.; Wenz, E.; Antonietti, M., *J. Chem. Phys.* **1996,** *104* (24), 9956-9970.
35. Li, Z.; Zhao, W.; Liu, Y.; Rafailovich, M. H.; Sokolov, J.; Khougaz, K.; Eisenberg, A.; Lennox, R. B.; Krausch, G., *J. Am. Chem. Soc.* **1996,** *118* (44), 10892-10893.
36. Yoo, S. I.; Sohn, B. H.; Zin, W. C.; Jung, J. C.; Park, C., *Macromolecules* **2007,** *40* (23), 8323-8328.
37. Hong, S. W.; Xu, J.; Xia, J. F.; Lin, Z. Q.; Qiu, F.; Yang, Y. L., *Chem. Mater.* **2005,** *17* (25), 6223-6226.
38. Yun, S. H.; Il Yoo, S.; Jung, J. C.; Zin, W. C.; Sohn, B. H., *Chem. Mater.* **2006,** *18* (24), 5646-5648.
39. Sohn, B. H.; Yoo, S. I.; Seo, B. W.; Yun, S. H.; Park, S. M., *J. Am. Chem. Soc.* **2001,** *123* (50), 12734-12735.
40. Chen, Z. Q.; He, C. C.; Li, F. B.; Tong, L.; Liao, X. Z.; Wang, Y., *Langmuir.* **2010,** *26* (11), 8869-8874.
41. Hong, S. W.; Wang, J.; Lin, Z. Q., *Angew. Chem. Int. Ed.* **2009,** *48* (44), 8356-8360.
42. Yoo, S. I.; Sohn, B. H.; Zin, W. C.; An, S. J.; Yi, G. C., *Chem. Commun.* **2004,** (24), 2850-2851.
43. Antonietti, M.; Wenz, E.; Bronstein, L.; Seregina, M., *Adv. Mater.* **1995,** *7* (12), 1000-&.

CHAPTER 3. ASSEMBLING AND POSITIONING LATEX NANOPARTICLES VIA CONTROLLED EVAPORATIVE SELF-ASSEMBLY

A paper published in *Journal of Materials Chemistry*, 21, 16968 (2011)

Wei Han and Zhiqun Lin*

Abstract

By capitalizing on a simple, robust, and fast approach based on controlled evaporative self-assembly in a cylinder-on-flat geometry, two kinds of polystyrene (PS) latex nanoparticles with different diameters (i.e., D = 50 nm and 500 nm, respectively) were deposited on the Si substrate, forming well-ordered "coffee rings" composed of PS nanoparticles. Within a "coffee ring", the packing of PS nanoparticles was found to be dependent upon the particle diameter. More intriguingly, when the aqueous solution of mixed two PS nanoparticles was used, "coffee rings" of small particles were positioned at the edge of three-phase contact line (D = 50 nm), followed by the adjacent deposition of large particles (D = 500 nm). These assembled deposits consisting of monolayer- or multilayer-thick latex nanoparticles over large areas may offer potential for applications in electronic devices, photonic bandgap materials, biosensors, particle sorting, and disease diagnosis.

Introduction

The ability to assemble and position colloidal particles is of practical interest for developing miniaturized optical, electronic, optoelectronic, information-storage materials and devices, and biosensors.[1, 2] A variety of methods have been adopted for structuring particles on a flat substrate, including gravitational sedimentation,[3, 4] electrophoretic deposition,[5] and

surface modification.[6, 7] Recently, a template-directed assembly approach has been widely used to guide the deposition of colloidal particles into well-ordered arrays. However, these pre-defined templates are commonly prepared by top-down conventional lithography techniques (e.g., e-beam lithography, soft lithography, and nanoimprint lithography) that are costly, complex and require a multi-step process. In this regard, evaporation-driven convective self-assembly has emerged as an extremely simple, appealing strategy to assemble and position the particles into useful structures.[8-14] However, due to the lack of control over the evaporation of volatile solvent, it is difficult to achieve a regular pattern over large areas.

In order to fully capitalize on the evaporation as a simple, lithography- and external field-free route to producing intriguing, ordered structures over large areas, it is crucial to control the evaporative flux, solution concentration, interfacial interaction between the solvent, the solute and the substrate, etc. To this end, a few elegant studies have centered on precise manipulation of the evaporation process in confined geometries (e.g., two parallel plates with the top one sliding on the lower stationary substrate,[15, 16] cylindrical tube,[17] or curve-on-flat geometries[18-36]) from which self-organized mesoscale patterns are readily obtained. Herein, we report a simple yet versatile method to assemble latex nanoparticles into regularly arranged stripe patterns (i.e., coffee ring-like deposits) over large areas by subjecting a drop of polystyrene (PS) latex nanoparticle aqueous solution to evaporate from a liquid capillary bridge formed by confining the solution between a cylindrical lens and a Si substrate (i.e., cylinder-on-flat geometry). A distinct difference in the surface morphology of PS stripes was observed with different nanoparticle diameters; that is, stripes composed of single layer nanoparticles were formed when large PS latex particles were used (D = 500 nm),

while stripes composed of multilayer nanoparticles were yielded when small PS latex particles were utilized (D = 50 nm). Quite intriguingly, when the aqueous solution of mixed these two PS nanoparticles was employed within a coffee ring-like stripe, small PS particles were positioned at the capillary edge, followed by positioning large PS particles next to them. The implementation of a cylinder-on-flat geometry suppressed the temperature gradient and associated convective flow, thus providing remarkable control over the solution evaporation during the deposition of nanoparticles. This method is fast and cost-effective, eliminating the need for multistage lithography and externally applied forces.

Experimental Section

Evaporative Self-Assembly of the PS Latex Particle Aqueous Solution in a Cylinder-on-Flat Geometry. The aqueous solutions containing PS latex particles with diameter of 50 nm and 500 nm labeled with red and blue fluorescent dyes, respectively, were purchased from Thermo Scientific and diluted to a constant concentration (c = 0.01wt% particle solids) without further purification. A mixed nanoparticle aqueous solution was also prepared by mixing 50 nm and 500 nm PS nanoparticles at the same concentration, c = 0.01wt% (weight ratio of 50 nm PS: 500 nm PS = 1:1). The Si substrate was cleaned with a mixture of sulfuric acid and Nochromix, then rinsed extensively with deionized (DI) water and blow-dried with N_2. A thin film of hexamethyldisilazane (HMDS，99.9%) was spin-coated (3000rpm and 60s) on the Si substrate to change its surface property from hydrophilic to hydrophobic. The cylindrical lens (L = 9.5 mm, H = 4.0 mm, W=11.0 mm, Figure 18a and 1b) was treated with octadecyltrichlorosilane (OTS) vapor to coat a thin film of OTS on the lens surface and placed on the Si substrate, thus forming a symmetry wetting between the hydrophobic

HMDS-coated Si substrate and the hydrophobic OTS-coated cylinder. The resulting cylinder-on-flat geometry was placed in a sealed chamber to minimize possible air convection and maintain constant temperature during the evaporation process. To study controlled evaporative self-assembly of PS latex nanoparticles in the cylinder-on-flat geometry, a drop of nanoparticle aqueous solution (volume, V = 30 μL) was loaded and bridged the cylinder and the Si substrate, yielding a capillary-held solution, where the evaporation rate was highest at the capillary edge (Figure 18b).[19] After the evaporation was complete, the patterns formed on the HMDS-coated Si were investigated.

Characterization. The stripe patterns formed from controlled evaporative self-assembly were examined by optical microscopy (OM; Olympus BX51 in the reflection mode) and atomic force microscopy (AFM; Dimension 3100 scanning force microscope in the tapping mode (Digital Instruments)). Fluorescent micrographs were obtained with the confocal fluorescent optical microscope (Leica SP5 X). Vista probes (T190) with spring constants 48Nm^{-1} were used as scanning probes. The patterns were also evaluated by field-emission scanning electron microscope (FE-SEM; FEI Quanta 250) operating at 10kv under high vacuum.

Results and Discussion

Rather than the conventional sessile droplet evaporation, the PS latex nanoparticle aqueous solution was restricted in the cylinder-on-flat geometry. As a result, the evaporation only occurred at the constrained capillary edge. To promote the evaporation of water, the aqueous solution was heated at a fixed temperature, $T = 80^0$C by placing a heat plate beneath the Si substrate. As water evaporated, PS latex nanoparticles were transported from the solution to the capillary edge and pinned the contact line (Figure 18c), thereby forming a

coffee-ring like deposit. During the deposition process, the initial contact angle of the meniscus at the capillary edge gradually decreased to a critical value due to continuous evaporative loss of water, at which the depinning force (i.e., capillary force) became larger than the pinning force. This caused the contact line to jump to a new position, where it was pinned again and a new "coffee ring" was thus yielded (Figure 18c).[19] Consequently, the repetitive pinning and depinning (i.e., "stick–slip" motion) of the contact line produced a lateral surface pattern consisting of hundreds of highly ordered concentric "coffee rings". Locally, they appeared as parallel stripes (Figure 19). This is in stark contrast with the generally irregular surface patterns formed from a sessile droplet evaporation as in copious past work.[37]

Notably, the use of confined geometry facilitated the creation of highly ordered stripes over large areas. Three representative optical micrographs of parallel stripes obtained by using different particle sizes (D = 50 nm, 500 nm, and their mixture at the weight ratio of 50 nm: 500 nm = 1:1, respectively) are shown in Figure 19. The solution concentration (c = 0.01wt%) and the loading volume (V = 30 μL) were kept the same for all PS particle solutions used in the study, however, three distinctively different surface patterns were observed. For the 500 nm PS nanoparticles, periodic but discontinued stripes composed of individual nanoparticles were produced via the "stick-slip" motion. The stripes were clearly separated from one another (Figure 19a). By contrast, the use of small particles as nonvolatile solute yielded straight, continuous stripes consisting of closely packed particles (D = 50 nm; Figure 19b). When a mixed nanoparticle solution was employed, complex surface patterns were formed (Figure 19c). Along the solution receding direction, the stripe was first highly

packed, followed by the presence of loosely scattered large particles (the inset in Figure 19c). It is worth noting that the formation of these regularly arranged stripes described above is highly reproducible.

Close examination of surface patterns by SEM revealed a noteworthy influence of particle size on its organization within stripes. It is clearly evident that the 500 nm particles were not fully connected to each other in a stripe (Figure 20a), consistent with the optical microscopy observation (Figure 19a). It should be noted that the stripes were monolayer particle thick; this is, for the first time, obtained via controlled evaporation in the confined geometry. The width of stripes depended on the number of particles in a stripe. By contrast, densely packed stripes were produced in the 50 nm particle case (Figure 20b). The small particles aggregated to form a multilayer stripe (see a cross-sectional view in Figure S1c in the Supporting Information). The maximum height of stripe was about 360 nm, approximately seven times the diameter of single 50 nm PS nanoparticle, suggesting a high degree of aggregation. The formation of these two differently packed patterns can be rationalized as follows. As the solution concentration (c = 0.01wt%) and the solution volume (V = 30 μL; indicating the same mass of particles) were fixed in the study, the number of 500 nm particles was much less than 50 nm counterparts in the solution (i.e., three orders less assuming the same density of PS particles; $(500/50)^3 = 10^3$). Moreover, because the evaporation rates for the aqueous solution containing different nanoparticles at the capillary edge were the same as a constant heating temperature on the Si substrate was applied, the force dragging nanoparticles from the solution to the contact line can thus be assumed the same for different nanoparticles. However, because of the larger weight of the 500nm

particle, their transportation was much slow during the drying process as compared to the case of lower weight, 50 nm particles. In other words, smaller nanoparticles possessed higher mobility than larger ones. As a result, fewer 500 nm PS particles can easily reach the contact line during the deposition process (i.e., "stick"), thus forming the monolayer, interrupted packing of nanoparticles (Figure 19a). By contrast, large amount of 50 nm particles can be readily transported and reach the contact line to form the multilayer, dense packing (Figure 19b).

We note that the implementation of the cylinder-on-flat geometry greatly suppressed the temperature gradient and associated convective flow in the experiment. In an evaporating liquid droplet on a heating substrate, the shape of deposits is determined by the competition between two convective flows, i.e., radial flow and Marangoni recirculation,[38] as illustrated in Figure 21a. The radial outward flow is induced by the solvent evaporation, which is largest at the edge of droplet. The radial velocity, $V_{rad} \sim j/\rho$, where j is the evaporative mass flux and ρ is the density of drop liquid.[39] In order to compensate the solution loss due to evaporation, the outward flow carries nonvolatile entrained solutes (e.g., particles) from the inner solution to the droplet edge and pin the contact line, forming the familiar "coffee-ring" patterns. The other relevant convective flow is the Marangoni recirculation. Marangoni flow is caused by temperature-gradient-induced surface tension gradient, which carries particles that are near the free liquid surface of the droplet inward toward the top of the droplet and then plunges them downward, forming bump-like depositions.[40] The loop velocity of Marangoni flow scales as $V_{Ma} \sim (1/32)(\beta \emptyset_i^2 \Delta T/\mu)$, where β is the surface tension gradient with respect to temperature, ϕ_i is

the wetting angle of the drop, μ is the dynamic viscosity, and ΔT is the temperature difference between the edge and the top of droplet.[41] The final pattern reflects a balance between the radial flow and Marangoni flow that operate in the different directions. However, in our study, due to the use of confined geometry to regulate the evaporation process, Marangoni flow was suppressed due to the application of the upper cylindrical lens (Figure 21b). As a result, the retained radial flow governed the formation of periodically arranged stripes via the "stick-slip" motion. Additionally, we note that the heating temperature (T = 80^{o}C) was critical in the present study. At lower temperature (T = 60^{o}C), the evaporation rate was quite low at the water/air/substrate three phase contact line, thus making the radial flow insufficient to transport particles to the contact line during the evaporation process. Thus, less ordered patterns were formed (Figure S2a-c in Supporting Information). On the other hand, the higher temperature (T = 100^{o}C; close to the boiling point of aqueous solution) led to the formation of some bubbles situated on the stripes, breaking the uniformity of stripes (Figure S2d-f).

We now turn our attention to address qualitatively the intriguing observations shown in Figure 19c and 3c, in which, within a stripe, small PS nanoparticles were first positioned in a densely packed manner and large PS nanoparticles were then positioned in a loosely packed fashion when the mixed nanoparticle aqueous solution was allowed to evaporate in the cylinder-on-flat geometry. The 50 nm and 500 nm particles were labeled with red and blue fluorescent dyes, respectively, thus the resulting surface patterns can be readily visualized by a fluorescence microscope to scrutinize the distribution of PS nanoparticles of different diameters inside stripes. Clearly, individual luminescent stripes were composed of

closely packed red nanoparticles (D = 50 nm) and scattered blue nanoparticles (D = 500 nm) as evidenced in Figure 22a and 5b. Blue nanoparticles were observed using a 405 nm excitation wavelength with an emission filter of 430-500 nm (Figure 22a). Red nanoparticles were differentiated using a 542 nm excitation wavelength with an emission filter of 605-620nm (Figure 22b). The superposition of these two fluorescent micrographs revealed that red-emitting nanoparticles were pinned first to form closely packed deposits, followed by adjacent deposition of blue-emitting nanoparticles to complete the formation of a stripe (Figure 22c). It is noteworthy that the minimal interstitial space between the 500 nm particles can be calculated $(\frac{\sqrt{6}}{2}-1)R$ = 0.225*R = 112.4 nm, assuming the 500 nm particles were packed into a regular tetrahedron. This minimal space is still larger than the size of small nanoparticles (D = 50 nm), indicating that small nanoparticles can move freely in the mixed particle solution without the interference from large nanoparticles. Moreover, as discussed above, during the particle transportation process, small nanoparticles could reach the contact line faster than large ones due to their high mobility in the solution, and were thus positioned first at the contact line. The presence of large amount of small particles (10^3 larger than large particles) favored dense packing and yielded a multilayer deposit (Figure 22d). By contrast, as large nanoparticles reached the contact line later and there were fewer particles in the solution, they formed discontinuous, monolayer-thick deposit adjacent to small nanoparticles within the stripe (Figure 22d). Notably, the curvature of the meniscus may also promote the separation of nanoparticles of different sizes. Small nanoparticles can be consistently transported to the contact line first due to lower local thickness of the meniscus, at which large nanoparticles cannot be accommodated and had to situate after the positioning of small

nanoparticles (Figure 22d).[42] This controlled positioning (i.e., size-dependent separation near the three-phase contact line) technique utilizing controlled evaporative self-assembly in a confined geometry may provide a facile route to size-dependent nanomaterials sorting.

Conclusions

In summary, by subjecting the PS latex nanoparticle aqueous solution to evaporate in a cylinder-on-flat geometry, well-ordered, monolayer- and multilayer-thick PS nanoparticle stripes were produced via controlled evaporative self-assembly of large and small particle aqueous solutions, respectively. Quite intriguingly, small and large nanoparticles can be positioned adjacently to one another within the stripe when an aqueous solution of mixed PS nanoparticles of different sizes was employed. This controlled evaporative self-assembly technique offer a simple yet robust route to assemble and position particles, mixed particles, and other nanomaterials into spatially regular patterns for use in electronic devices, photonic bandgap materials, biosensors, particle sorting, and disease diagnosis.

Figures

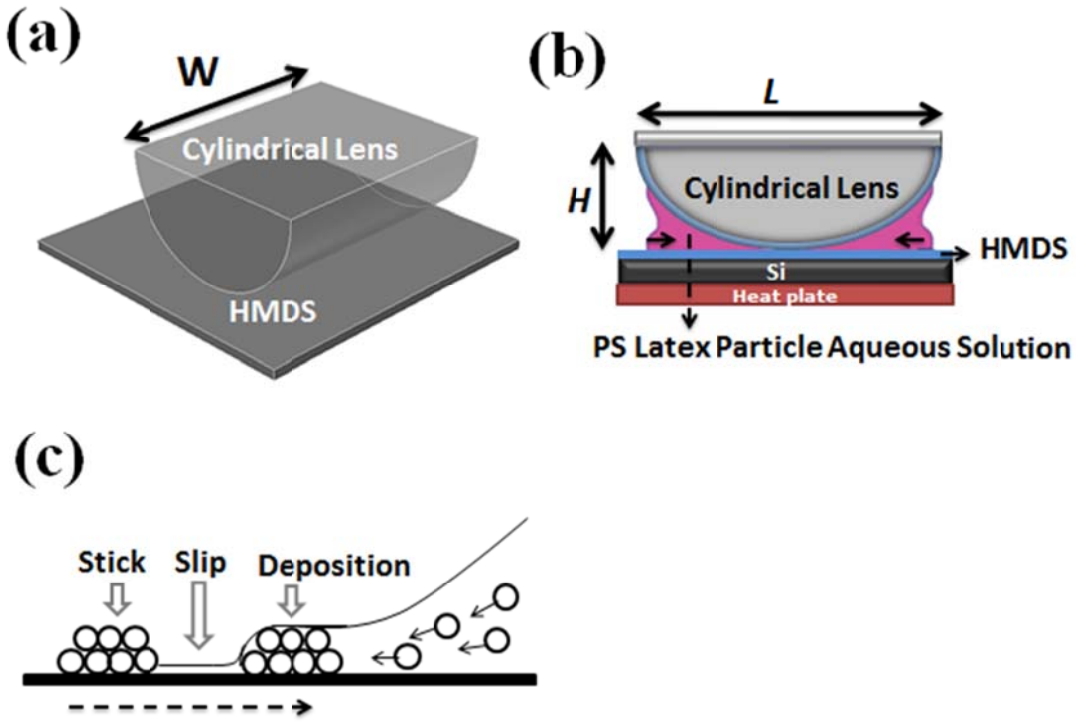

Figure 18. Schematic representation of the formation of regularly arranged PS latex nanoparticle stripes. A drop of nanoparticle aqueous solution was trapped in a "cylinder-on-flat" geometry, forming a capillary-held solution. (a) 3D view and (b) side view of the "cylinder-on-flat" geometry. *H*, *L*, and *W* are the height, length, and width of cylinder, respectively. The black arrows within the trapped solution in pink mark the movement of the solution front toward the cylinder/Si contact center. (c) Schematic illustration of the nanoparticle deposition via a "stick-slip" motion.

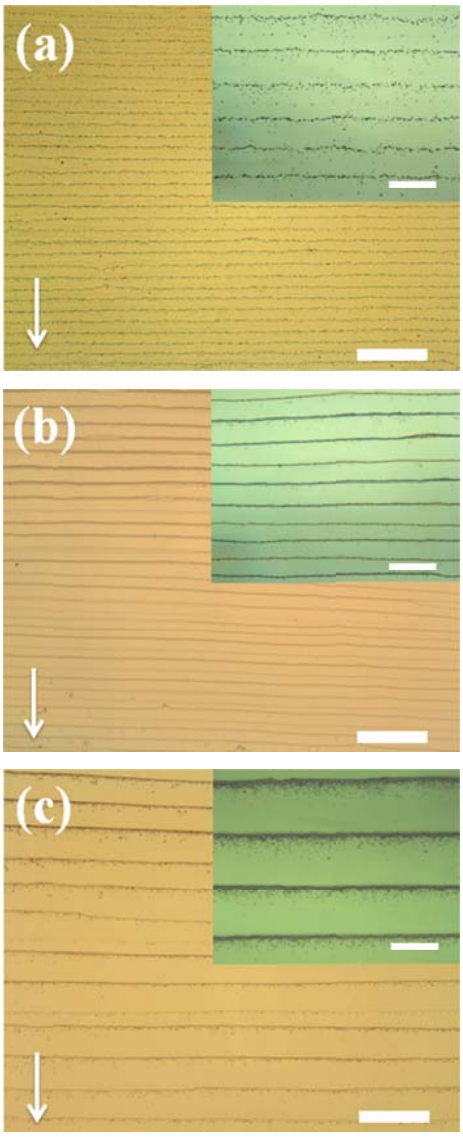

Figure 19. Representative optical micrographs of parallel stripes composed of PS particles formed from (a) the 500 nm nanoparticle solution; (b) the 50 nm nanoparticle solution; and (c) the mixed nanoparticle solution (weight ratio of 50 nm nanoparticles: 500 nm nanoparticles = 1:1) by controlled evaporative self-assembly in a cylinder-on-flat geometry. The arrow indicates the receding direction of the solution during the drying process. Scale bars = 50 μm and 200 μm in the main image and the inset, respectively.

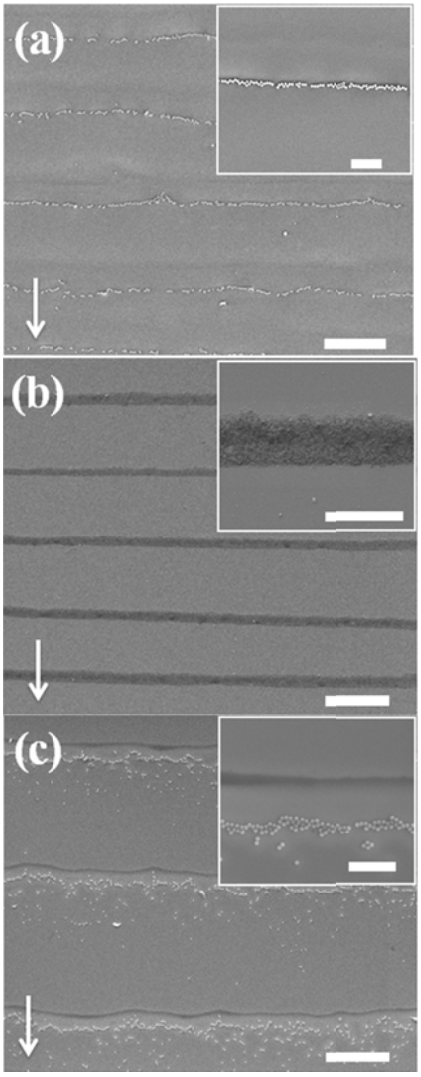

Figure 20. Scanning electron microscope (SEM) images of stripe patterns composed of PS nanoparticles of different diameters. (a) 500 nm PS particles with discontinued monolayer particle packing; (b) 50 nm PS particles with highly close packing; and (c) mixed PS nanoparticles packed next to one another; within a stripe closely packed 50 nm particles (upper) were adjacent to 500 nm particles (lower)). The arrow indicates the receding direction of the solution during the drying process. Scale bars = 5 μm and 20 μm in the main image and the inset, respectively.

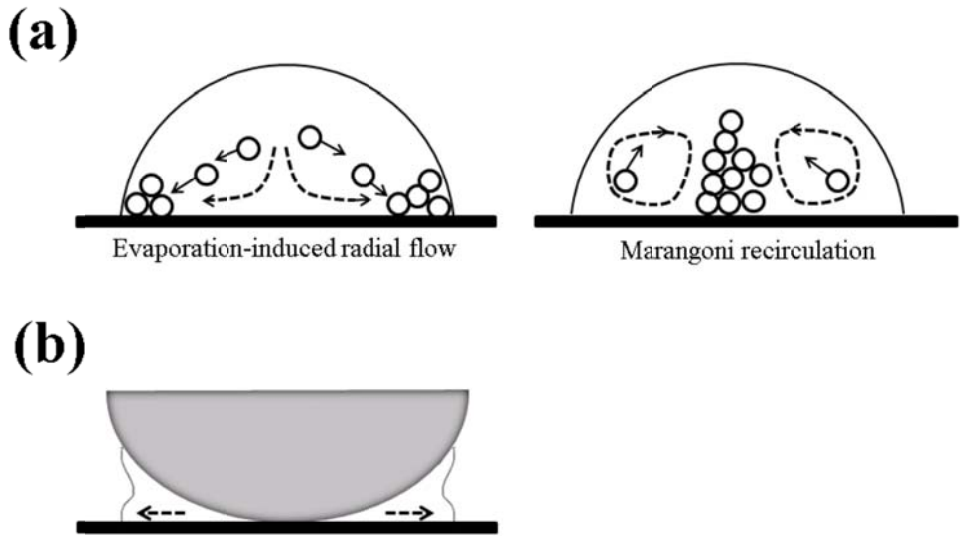

Figure 21. (a) The flow profiles in a sessile droplet. *Left*: radial flow. *Right*: Marangoni recirculation. These two flows compete to form deposits on the surface. (b) With the confinement, the Marangoni flow is suppressed while the radial flow is retained, thus forming periodically ordered stripes via the "stick-slip" motion.

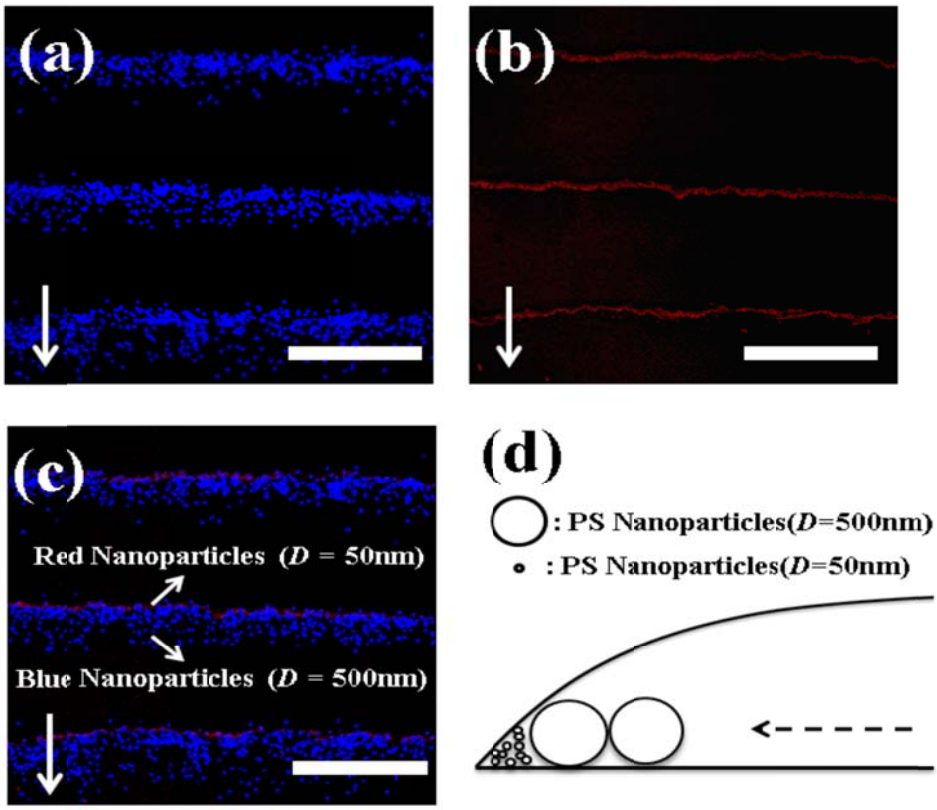

Figure 22. Fluorescent micrographs of adjacent packing of PS nanoparticles of different diameters within stripes formed by controlled evaporative self-assembly of the mixed particle aqueous solution under different excitation wavelengths. (a) Under 405 nm excitation wavelength, blue-emitting nanoparticles can be observed (D = 500nm); (b) 542-nm excitation makes the red-emitting nanoparticles visible (D = 50nm); (c) Combined fluorescent micrograph, showing adjacent packing of two nanoparticles of different diameters. (d) Schematic illustration of the formation of adjacently packed particles. Arrows in (a)-(c) mark the moving direction of the solution front during the course of evaporation. Scale bar = 50μm in (a)-(c).

Supporting Information:

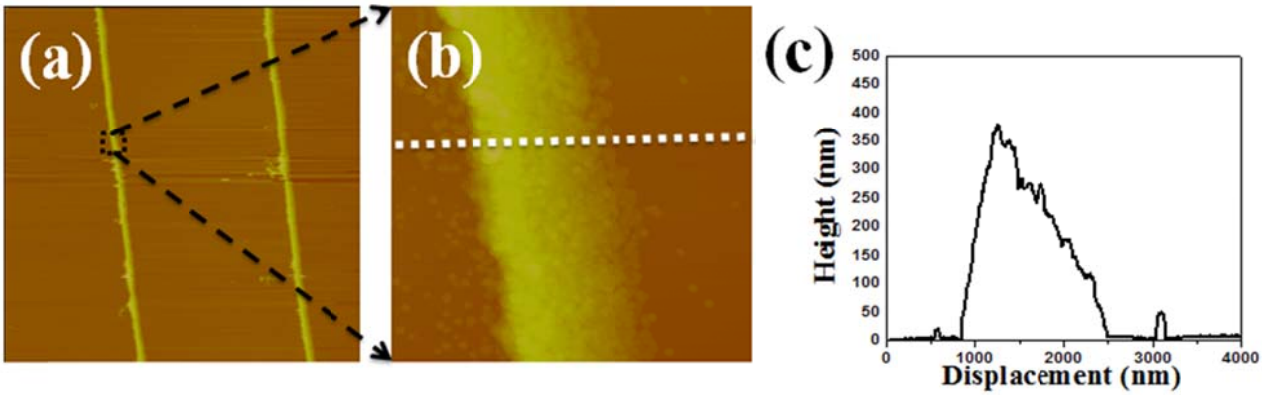

Figure S1. (a-b) AFM images of the stripes formed from the 50 nm nanoparticles. (c) Corresponding section analysis in (b). Image sizes: (a) 80 x 80 μm^2 and (b) 4 x 4 μm^2.

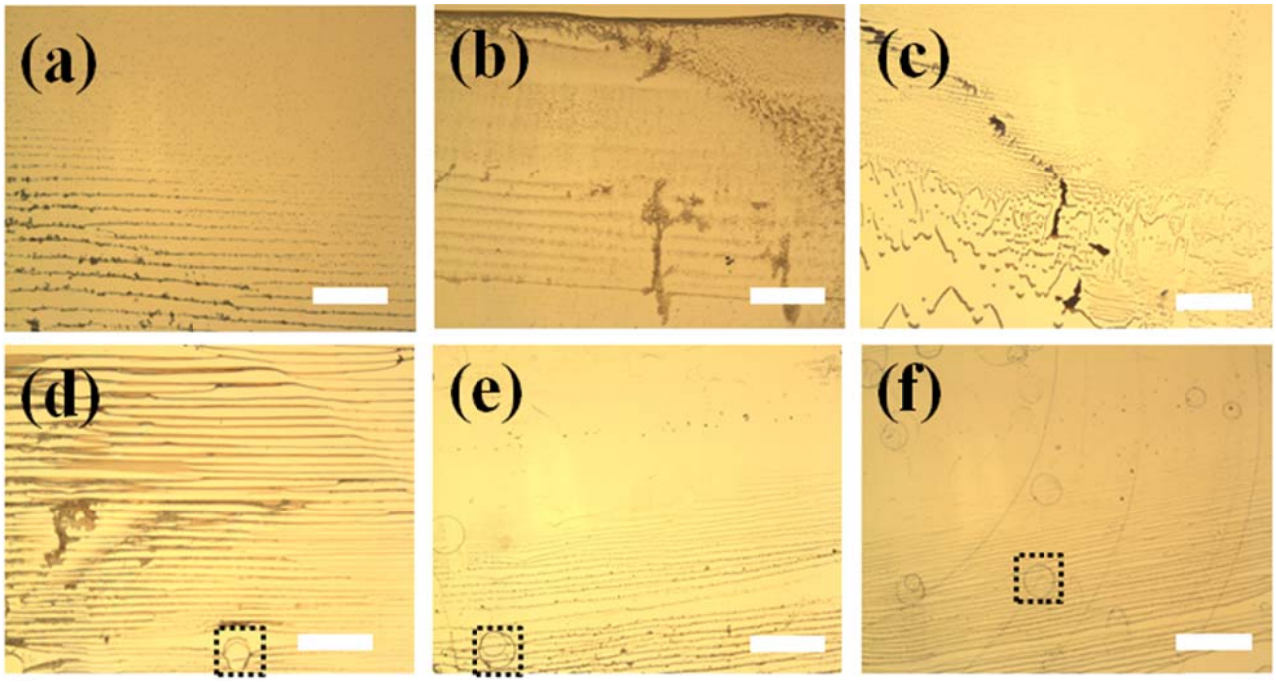

Figure S2. Optical micrographs of stripes composed of PS latex nanoparticles formed from controlled evaporative self-assembly at different temperatures. Upper panels: the aqueous solution containing (a) 50 nm particles, (b) 500 nm particles, and (c) mixed nanoparticles evaporated at 60°C, respectively. Lower panels: the aqueous solution containing (d) 50 nm particles, (e) 500 nm particles, and (f) mixed nanoparticles evaporated at 100°C, respectively. At lower temperature (T = 60°C), less ordered patterns were observed. By contrast, at higher temperature (T = 100°C), due to the formation of bubbles at the boiling temperature of water, some small circles were formed around the stripes, marked inside dashed boxes. Scale bar = 250 μm.

References

1. J. Huang, F. Kim, A. R. Tao, S. Connor and P. D. Yang, *Nature Mater.*, 2005, **4**, 896.
2. R. M. Erb, H. S. Son, B. Samanta, V. M. Rotello and B. B. Yellen, *Nature*, 2009, **457**, 999.
3. H. Míguez, F. Meseguer, C. López, Á. Blanco, J. S. Moya, J. Requena, A. Mifsud and V. Fornés, *Adv Mater*, 1998, **10**, 480-483.
4. J. Zhu, M. Li, R. Rogers, W. Meyer, R. H. Ottewill, S. T. S. S. S. Crew, W. B. Russel and P. M. Chaikin, *Nature*, 1997, **387**, 883-885.
5. M. Holgado, F. García-Santamaría, A. Blanco, M. Ibisate, A. Cintas, H. Míguez, C. J. Serna, C. Molpeceres, J. Requena, A. Mifsud, F. Meseguer and C. López, *Langmuir*, 1999, **15**, 4701-4704.
6. Q. Yan, L. Gao, V. Sharma, Y.-M. Chiang and C. C. Wong, *Langmuir*, 2008, **24**, 11518-11522.
7. M. A. Ray, H. Kim and L. Jia, *Langmuir*, 2005, **21**, 4786-4789.
8. N. Denkov, O. Velev, P. Kralchevski, I. Ivanov, H. Yoshimura and K. Nagayama, *Langmuir*, 1992, **8**, 3183-3190.
9. Q. Yan, Z. Zhou and X. S. Zhao, *Langmuir*, 2005, **21**, 3158-3164.
10. Z. Zhou and X. S. Zhao, *Langmuir*, 2003, **20**, 1524-1526.
11. P. Jiang, J. F. Bertone, K. S. Hwang and V. L. Colvin, *Chem Mater*, 1999, **11**, 2132-2140.
12. B. G. Prevo and O. D. Velev, *Langmuir*, 2004, **20**, 2099-2107.
13. M. Muller, R. Zentel, T. Maka, S. G. Romanov and C. M. Sotomayor Torres, *Chem Mater*, 2000, **12**, 2508-2512.
14. B. P. Khanal and E. R. Zubarev, *Angew. Chem. Int. Ed.*, 2007, **46**, 2195.
15. B. H. Kim, D. O. Shin, S.-J. Jeong, C. M. Koo, S. C. Jeon, W. J. Hwang, S. Lee, M. G. Lee and S. O. Kim, *Adv. Mater.*, 2008, **20**, 2303
16. H. Yabu and M. Shimomura, *Adv. Funct. Mater.*, 2005, **15**, 575.
17. M. Abkarian, J. Nunes and H. A. Stone, *J. Am. Chem. Soc.*, 2004, **126**, 5978.
18. S. W. Hong, J. Xu, J. Xia, Z. Q. Lin, F. Qiu and Y. L. Yang, *Chem. Mater.*, 2005, **17**, 6223.
19. J. Xu, J. Xia, S. W. Hong, Z. Q. Lin, F. Qiu and Y. L. Yang, *Phys. Rev. Lett.*, 2006, **96**, 066104.
20. J. Xu, J. Xia and Z. Q. Lin, *Angew. Chem., Int. Ed.*, 2007, **46**, 1860.
21. S. W. Hong, M. Byun and Z. Q. Lin, *Angew. Chem., Int. Ed.*, 2009, **48**, 512.
22. S. W. Hong, S. Giri, V. S. Y. Lin and Z. Q. Lin, *Chem. Mater.*, 2006, **18**, 5164.
23. S. W. Hong, W. Jeong, H. Ko, M. R. Kessler, V. Tsukruk and Z. Q. Lin, *Adv. Funct. Mater.*, 2008, **18**, 2114
24. S. W. Hong, J. Wang and Z. Q. Lin, *Angew. Chem., Int. Ed.*, 2009, **48**, 8356.
25. S. W. Hong, J. Xia, M. Byun, Q. Zou and Z. Q. Lin, *Macromolecules*, 2007, **40**, 2831.
26. S. W. Hong, J. Xia and Z. Q. Lin, *Adv. Mater.*, 2007
19, 1413.
27. S. W. Hong, J. Xu and Z. Q. Lin, *Nano Lett.*, 2006, **6**, 2949.
28. M. Byun, N. B. Bowden and Z. Q. Lin, *Nano Lett.*, 2010, **10**, 3111.
29. M. Byun, W. Han, F. Qiu, N. B. Bowden and Z. Q. Lin, *Small*, 2010, **6**, 2250.
30. M. Byun, S. W. Hong, F. Qiu, Q. Zou and Z. Lin, *Macromolecules* 2008, **41**, 9312.

31. M. Byun, S. W. Hong, L. Zhu and Z. Q. Lin, *Langmuir*, 2008, **24**, 3525.
32. M. Byun, R. L. Laskowski, M. He, F. Qiu, M. Jeffries-EL and Z. Q. Lin, *Soft Matter*, 2009, **5**, 1583.
33. M. Byun, J. Wang and Z. Lin, *J. Phys.: Cond. Matt.* , 2009, **21**, 264014.
34. M. Byun, J. Wang and Z. Lin, *Acta Phys. -Chim. Sin.*, 2009, **25**, 1249.
35. J. Wang, J. Xia, S. W. Hong, F. Qiu, Y. Yang and Z. Q. Lin, *Langmuir*, 2007, **23**, 7411.
36. W. Han, M. Byun, L. Zhao, J. Rzayev and Z. Lin, *J. Mater. Chem.*, 2011, (in press).
37. E. Adachi, A. S. Dimitrov and K. Nagayama, *Langmuir*, 1995, **11**, 1057.
38. R. Bhardwaj, X. Fang, P. Somasundaran and D. Attinger, *Langmuir*, 2010, **26**, 7833-7842.
39. H. Hu and R. G. Larson, *Langmuir*, 2005, **21**, 3963-3971.
40. F. Girard, M. Antoni, S. Faure and A. Steinchen, *Langmuir*, 2006, **22**, 11085-11091.
41. H. Hu and R. G. Larson, *Langmuir*, 2005, **21**, 3972-3980.
42. T.-S. Wong, T.-H. Chen, X. Shen and C.-M. Ho, *Anal Chem*, 2011, **83**, 1871-1873.

CHAPTER 4. CONTROLLED EVAPORATIVE SELF-ASSEMBLY OF HIERARCHICALLY STRUCTURED BOTTLEBRUSH BLOCK COPOLYMER WITH NANOCHANNELS

A paper published in *Journal of Materials Chemistry*, 21, 14248 (2011)

Wei Han, Myunghwan Byun, Lei Zhao, Javid Rzayev, and Zhiqun Lin*

Abstract

The toluene solution of a bottlebrush block copolymer, polystyrene-polylactide (PS-PLA), was confined in a cylinder-on-flat geometry, from which the consecutive "stick-slip" motion of the three-phase contact line of the PS-PLA solution was effectively regulated as toluene evaporated, thereby yielding gradient stripes at the microscopic scale. Subsequent selective solvent vapor annealing led to the formation of hierarchically structured PS-PLA in which the lamellar nanodomains of PS-PLA normal to the substrate were obtained within the microscopic stripes. After the selective removal of the PLA blocks by enzymatic degradation, nanochannels were yielded within the stripes. This facile approach by combining the controlled evaporative self-assembly with subsequent solvent vapor annealing opens up a new avenue to rationally organize and engineer self-assembling building blocks into functional materials and devices in a simple, cost-effective and controllable manner.

Introduction

Spontaneous self-assembly of nanoscale materials to form intriguing, complex yet well-ordered structures via the evaporation of a sessile droplet containing nonvolatile solutes provides a simple means to fabricate functional materials.[1-7] However, flow instabilities

within the evaporating droplet often result in irregular dissipative structures (e.g., fingering instabilities, convection patters, etc.).[4, 8-9] To date, a few elegant methods have emerged to precisely control the evaporation process to produce highly ordered structures that are technologically relevant. Among them, controlled evaporative self-assembly (*CESA*) of a droplet constrained in restricted geometries (e.g., sphere-on-flat) renders the creation of intriguing structures with high fidelity and regularity.[10-23] Diblock copolymers composed of two chemically distinct chains that are covalently linked at one end are thermodynamically driven to self-assemble into a range of well-ordered nanodomains, including spheres, cylinders and lamellae, depending on the volume fractions of the components. The size of nanodomains governed by the molecular weight of the polymer is typically on the order of tens of nanometers, thereby offering a facile route to nanodevice fabrication and nanotechnology.[24-25] Notably, among a variety of block copolymers, polylactide (PLA) containing block copolymers with cylindrical and lamellar morphologies are particularly attractive as they offer a facile route to produce nanoporous and nanochannel materials and devices by hydrolysis of the PLA block.[26-27]

Hierarchical structures over multiple length scales are highly desirable for many technological applications. The use of micro-patterning techniques (e.g., photolithography and e-beam lithography) to produce hierarchical structures involves high processing and maintenance costs and requires an iterative, multistep procedure that makes the structure formation process more complex and less reliable. By contrast, techniques that combine top-down controlled self-assembly (i.e., forming microscopic features) with bottom-up spontaneous self-assembly (i.e., forming nanoscale features) provide a lithography- and external-field-free means to create hierarchically organized structures.[10, 14, 28]

Herein, we report a simple yet robust technique based on the controlled evaporative self-assembly (CESA) of a newly synthesized bottlebrush block copolymer (BBCP), polystyrene-polylactide (PS-PLA) in a restricted geometry composed of a cylindrical lens situated on a flat substrate (i.e., cylinder-on-flat geometry) to produce gradient stripes of PS-PLA *at the microscopic scale*. Subsequent solvent vapor annealing promoted spontaneous microphase separation of PS-PLA, forming lamella of PS and PLA oriented normal to the surface of stripes *at the nanoscale*. Selective removal of PLA arms by enzymatic degradation resulted in the formation of *nanochannels* within the *microscopic stripes*, thereby yielding hierarchically organized structures over large areas. This technique offers a promising route for crafting hierarchically ordered structures for use in optical, electronic, optoelectronic, and magnetic materials and devices.

Experimental Section

Synthesis and Characterization of PS-PLA Bottlebrush Block Copolymer (BBCP). A PS-PLA BBCP with an ultrahigh molecular weight of 1.2×10^6 g/mol was synthesized according to the procedure previously reported by us.[29] The PS and PLA arms were densely grafted along the polymethacrylate backbone through the ester group. The lengths of the backbone, the PLA arm and the PS arm are 90nm, 6.3nm and 6.5nm, respectively.[29-30] The volume fraction of PS arms was calculated to be 60%.

Controlled Evaporative Self-Assembly (CESA) of the PS-PLA toluene Solution in a Cylinder-on-Flat Geometry. PS-PLA was dissolved in toluene at a concentration of 0.15 $mgmL^{-1}$ and purified with 200 nm polytetrafluoroethylene (PTFE) filters. The Si substrates were cleaned with a mixture of sulfuric acid and Nochromix, then rinsed extensively with

deionized (DI) water and blow-dried with N_2. A thin film of hexamethyldisilazane (HMDS) was spin-coated at 3000rpm for 60s on the Si substrate to change the surface property of Si substrate from hydrophilic to hydrophobic.[42] The cylindrical lens (L=9.5mm, H=4.0 mm and W=11.0mm; Figure 243b) and HMDS-treated Si substrate were used as the upper and lower surface, respectively, to construct a cylinder-on-flat geometry. This geometry was then placed in a sealed chamber to minimize possible air convection and maintain constant temperature during the evaporation process.

Surface Reconstruction via Solvent Vapor Annealing. The highly regular, gradient PS-PLA stripes formed on the HMDS-coated Si substrate were exposed to the chloroform vapor for 12 hrs in a closed vessel to achieve morphological reconstruction of PS-PLA. The small piece of gauze soaked with chloroform was placed into a 29.4 cm^3 vessel. The value of chloroform vapor pressure, P, was calculated to be 14.5 N cm^{-2} based on $P = m_s RT / MV$.[10] The vessel was sealed by Teflon and placed in an Ar grove box to avoid temperature and humidity variations.

Degradation of PLA Arms in PS-PLA BCCP within Stripes. Proteinase K was purchased from Sigma and used without purification. The enzymatic degradation was performed by immersing the sample into the degradation solution prepared by adding 1.0mg of Proteinase K into 5mL of Tris-HCl buffer (pH=8.6) at 37^{o}C in an oil bath for various times. After the degradation was terminated, the sample was dried under vacuum for 12 hr at room temperature.

Characterization. The evaporation took less than 30 min to complete. Afterward, the cylinder and the HMDS-coated Si substrate were separated. Because of the curvature effect of the cylinder, only the patterns formed on the flat HMDS-coated Si substrate were

characterized by optical microscopy (OM; Olympus BX51 in the reflection mode) and atomic force microscopy (AFM, Dimension 3100 scanning force microscope in the tapping mode; Digital Instruments). Vista probes (T190) with spring constants $48 Nm^{-1}$ were used as scanning probes.

Results and Discussion

Nanomaterials with domain sizes large than 100nm are highly desirable for applications in photonics and ultrafiltration. However, they are difficult to obtain by the self-assembly of *linear* block copolymer. Recently, nanostructured materials with large domain spacings of 100nm and beyond have been successfully achieved using a novel PS-PLA BBCP,[29] synthesized by a combination of living radical polymerization and ring-opening polymerization. The self-assembly of PS-PLA at the air/water interface was explored.[30] In the present study, a PS-PLA BBCP with an ultrahigh molecular weight of 1.2×10^6 g/mol was employed as the nonvolatile solute to prepare the PS-PLA toluene solution. The chemical structure and schematic representation of PS-PLA are depicted in Figure 243a and 1b, respectively. This BBCP is a comb-like macromolecule with highly densely grafted PS and PLA arms along the polymethacrylate backbone (Figure 243a and 1b). The lengths of the backbone, the PLA arm and the PS arm are 90nm, 6.3nm and 6.5nm, respectively (see *Experimental Section*).[29-30] This ultrahigh molecular weight BBCP appeared to self-assemble into a highly-ordered morphology (i.e., lamella) upon thermal annealing, which was attributed to the steric crowding of PLA and PS arms and the unentangled nature of BBCP.[29]

The PS-PLA toluene solution (volume: V =30μL) with the concentration of 0.15mg/mL was then loaded and trapped in a restricted geometry composed of a cylindrical

lens sitting on a Si substrate coated with hexamethyldisilazane (HMDS) (i.e. cylinder-on-flat geometry; Figure 243c) (see *Experimental Section*), yielding a capillary-held solution. It is noteworthy that the evaporation of toluene only occurred at the constrained capillary edge (Figure 243c). The evaporative loss of toluene at the capillary edge triggered the pinning of the three-phase contact line (i.e., "stick") by transporting nonvolatile PS-PLA to the capillary edge. The outermost PS-PLA stripe was thus formed.[31] During the deposition of PS-PLA, the initial contact angle of the solution gradually decreased due to the toluene evaporation to a critical contact angle, at which the capillary force (i.e., depinning force) became larger than the pinning force. This caused the contact line to jump to a new position inward (i.e., "slip"), where it was arrested again and a new polymer stripe was thus produced. The repeated pinning and depinning cycles of the contact line led to the formation of regular stripes of PS-PLA (last panel in Figure 243c).[19] The stripes exhibited gradient features, representing the decrease in the height, H and width, W of the stripes, and the center-to-center distance between neighboring polymer stripes, λ, as the liquid capillary edge gradually approached the cylinder/HMDS-coated Si contact center (last panel in Figure 243c). The formation of gradient stripes was a direct consequence of the competition between the nonlinear capillary force, due to the curvature effect of the cylinder, and the linear pinning force.[19]

After the evaporation was completed, the structure formed on the HMDS-coated Si was examined. Three representative optical micrographs taken at different radial distance, X_n (i.e., outermost region, X_1; intermediate region, X_2; and innermost region, X_3; where X is the distance away from the cylinder/HMDS-coated Si contact center; Figure 243c) are shown in Figure 24. They appeared as parallel periodic stripes over large areas. The AFM measurements showed the stripes were gradient, in which the average H and W of the stripes,

and the λ between adjacent stripes decreased progressively from H = 92nm, W = 6.1μm and λ = 18.7μm in the outermost region, corresponding to X_1 = 4200μm, to H = 56nm, W = 4.2μm and λ = 11.6μm in the intermediate region, corresponding to X_2 = 3900μm, to H = 31nm, W = 2.8μm and λ = 6.9μm in the innermost region, corresponding to X_3 = 3600μm (Figure 25a-c). It is worth noting that these self-organized stripes, formed by CESA of the BBCP solution, were highly reproducible. The close examination of an individual microscopic stripe revealed a disordered, featureless surface morphology within the stripe (Figure 25d-f). This may be attributed to the fast depletion of toluene, which did not afford the polymer chains much time for the microphase separation to occur.[10]

To this end, selective solvent vapor annealing was performed on the PS-PLA stripes. The solvent vapor annealing method has been widely recognized as one of the most effective post treatments to achieve morphological rearrangement of nanodomains in block copolymers[32-34]. The selective solvent (i.e., chloroform) vapor annealing in a closed vessel for 12hr was conducted on the periodic stripes. The polymer/solvent interaction parameter for PLA is $\chi_{chloroform/PLA} = 0.32$, which is smaller than for PS, $\chi_{chloroform/PS} = 0.45$, suggesting that the PLA block preferentially responds to the exposure of chloroform vapor. After the 12-hr vapor annealing, the reconstruction of PS-PLA nanodomains within the microscopic straight stripes occurred (i.e., microphase separation of PS-PLA; Figure 26d-f) as will be discussed later. We note that the AFM measurements were conducted at the same position for the sample before (i.e., as-prepared) and after the vapor annealing. Quite intriguingly, at the microscopic scale, after the chloroform vapor annealing, distinct morphological alterations of stripes were observed (Figure S1; H and W changed, while λ did not change

over the entire surface). The H and W were changed to H = 46nm and W =11.2μm at X_1 = 4200μm, to H = 27nm and W =7.9μm at X_2 = 3900μm, and to H = 17nm and W =6.1μm at X_3 = 3900μm, respectively. It has been demonstrated that the HMDS-treated Si substrate is hydrophobic, with which the hydrophobic PS would preferentially interact.[35] Thus, during the course of vapor annealing, the volume of PS arms on the hydrophobic HMDS surface increased, and the PS arms wetted the hydrophobic HMDS surface to lower the interfacial energy. As a result, the width of stripes was increased laterally while the average height of the stripes decreased by approximately two fold, compared to the sample prior to the vapor annealing (Figure 27 and Figure S1).

Upon exposure to the chloroform vapor, the chain mobility of PS-PLA BBCP was effectively enhanced. As a result, the disordered, featureless topology (Figure 25d-f) was transformed into vertically oriented lamellar nanodomains due to the packing of rigid macromolecules[29] within the stripes (Figure 26d-f). The surface energies of PS and PLA blocks are similar (PS: 39.4-40.7mJ/m^2 and PLA: 36-41mJ/m^2), therefore there was no preferential wetting of either PLA or PS at the polymer/air interface.[35-36] On the other hand, since chloroform is a selective solvent for the PLA block, the PLA was swollen by continuous uptake of chloroform vapor and pulled to the polymer/air interface to contact preferentially with the chloroform vapor (i.e., the air surface). Furthermore, it is noteworthy that the characteristic length, L_0 of the ultrahigh molecular weight PS-PLA was L_0 = 105 ± 5 nm (Figure S2c),[29] with which the height of stripes cannot commensurate (the stripe height after annealing was less than 50nm; i.e., H = 46nm at X_1 , H = 27nm at X_2, and H = 17nm at X_3), thus favoring the nanodomains (i.e., lamella) to orient normal to the stripe surface.[37] Taken together, vertically oriented lamella of PS-PLA was observed. Thus, hierarchically

structured PS-PLA were yielded, that is, at the micrometer scale, gradient stripes were formed globally by CESA of PS-PLA (i.e., a top-down approach), and at the nanometer scale, vertically oriented lamella within microscopic stripes were achieved due to spontaneous self-assembly of PS-PLA that was promoted by the solvent vapor annealing (i.e., a bottom-up approach). Notably, as opposed to thermally equilibrated block copolymer thin film morphologies, hierarchical structures produced by the solvent vapor annealing process in the present study were far from equilibrium. As PS has a higher modulus than PLA at room temperature (E_{PS} = 3.0GPa and E_{PLA} = 2.05GPa[38]), the PS block appeared brighter in the AFM phase images, corresponding to a larger phase shift.[33] Moreover, the selective swelling of PLA nanodomains by chloroform caused a relatively lower height of PLA block than PS block on the surface. As a result, the PS lamella was higher in the AFM height image and brighter in the AFM phase image than the PLA lamella (Figure 26).

PLA is a biodegradable polymer which can be degraded by either an enzymatic approach or alkaline hydrolysis.[39-40] We used Proteinase K to remove the PLA arms by immersing the sample into the degradation solution (i.e., Proteinase K Tris-HCl buffer solution; see *Experimental Section*), thereby forming nanochannels in the gradient microscopic stripes. Since the native oxide on the Si substrate preferentially interacts with the PLA block and forms a wetting layer of PLA, the stripes would be floated off the Si substrate when performing the degradation experiment.[30] In this context, to create nanochannels, the Si substrate coated with HMDS was used to form a wetting layer of PS on the HMDS substrate as HMDS preferentially interacts with the PS block.[30, 33, 35] After immersing the chloroform-vapor-annealed samples in the degradation solution at 37^{o}C for various times (i.e., 30min and 60min), the PS part still remained while the PLA arms were degraded. Figure 27b-c show the

surface morphologies of thin films after the enzymatic degradation for 30min and 60min, respectively. The roughness of the as-prepared sample was 1.75nm, measured by AFM (Figure 27a). When degraded for 30min and 60min, the roughness changed to 4.33nm and 4.78nm, respectively**.** The nanochannel depth increased after the degradation as revealed by the section analysis of the AFM images (Figure S3), indicating the successful removal of PLA arms.

Conclusion

In summary, we demonstrated a facile technique to create hierarchically structured PS-PLA BBCP by combining CESA of the PS-PLA toluene solution in the cylinder-on-flat geometry, which yielded microscopic gradient stripes over large areas, with spontaneous self-assembly of PS-PLA at the nanoscale, which was facilitated by selective solvent vapor annealing. The enzymatic removal of PLA arms in PS-PLA rendered the formation of nanochannels within the stripes. These nanochannels may serve as a template to transfer the nanopartterns to the substrate by reactive ion etching[41] for fabricating nanodevices. The present technique provides a promising approach to craft hierarchically ordered structures for potential applications in optics, electronics, optoelectronics, magnetic materials and devices, biotechnology, and nanotechnology.

Figures

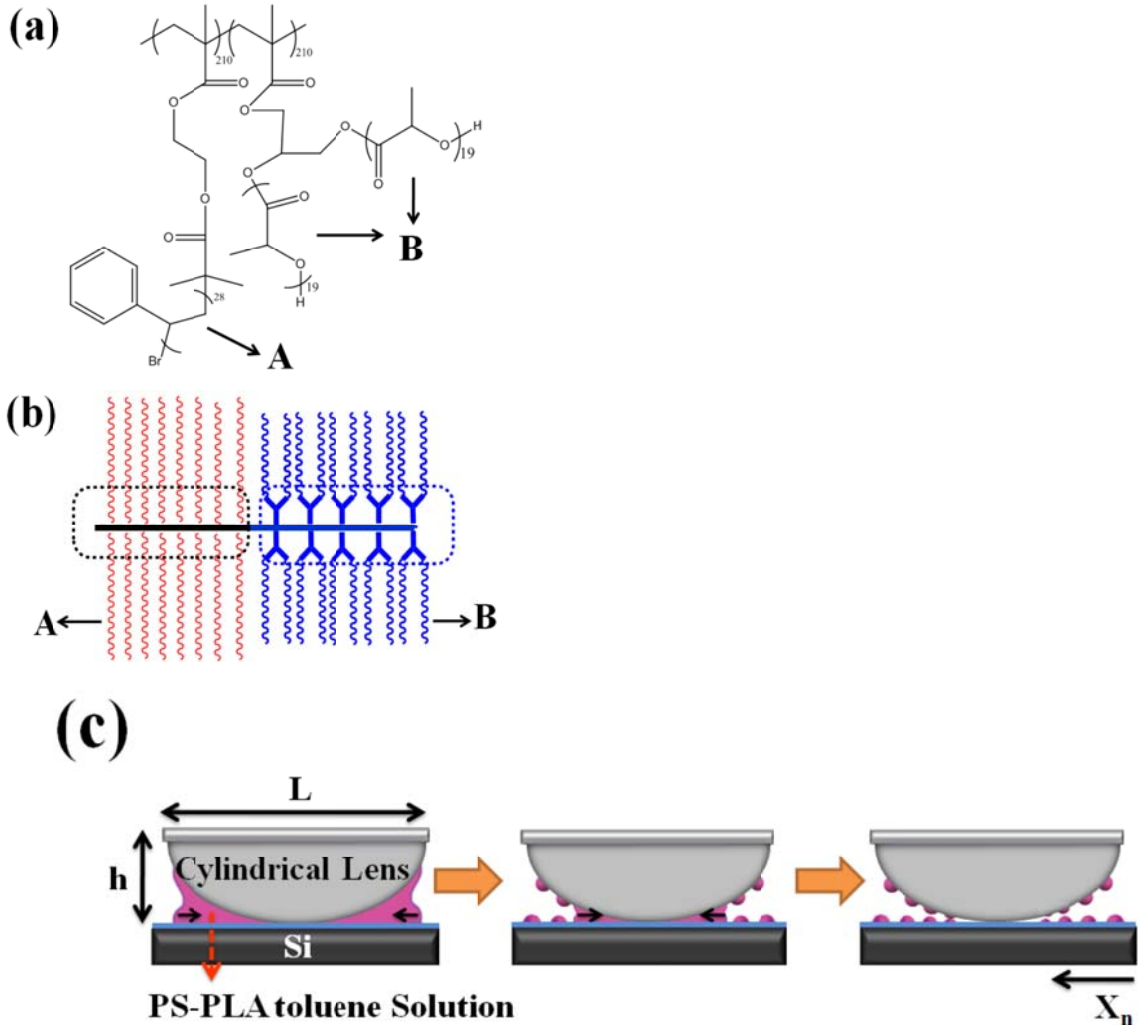

Figure 243. (a) Chemical structure of a newly synthesized bottlebrush block copolymer, PS-PLA (A = PS block and B = PLA block). (b) Schematic representation of PS-PLA with PLA (red) and PS (blue) chains densely grafted on the backbone (black). (c) Stepwise representation of the formation of stripes by allowing a drop of PS-PLA toluene solution to evaporate in the cylinder-on-flat geometry (side view). *h* and *L* are the height and length of cylindrical lens, respectively. The Si substrate was spin-coated with a thin layer of HMDS (blue). The black arrows mark the direction of the movement of the solution front toward the cylinder/HMDS-coated Si contact center. X_n indicates the distance away from the contact center.

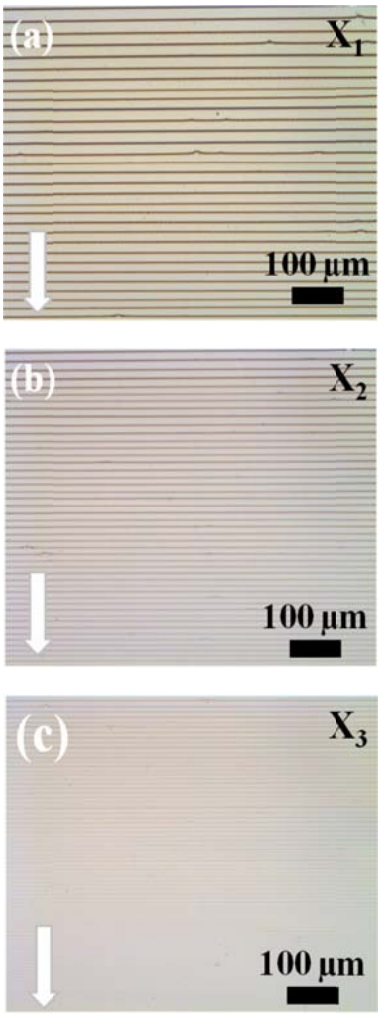

Figure 24. Optical micrographs of PS-PLA stripes formed by controlled evaporative self-assembly (CESA) in a cylinder-on-flat geometry. (a) in the outermost region, X_1, (b) in the intermediate region, X_2, and (c) in the innermost region, X_3, respectively. The arrows mark the moving direction of the solution front during the course of evaporation.

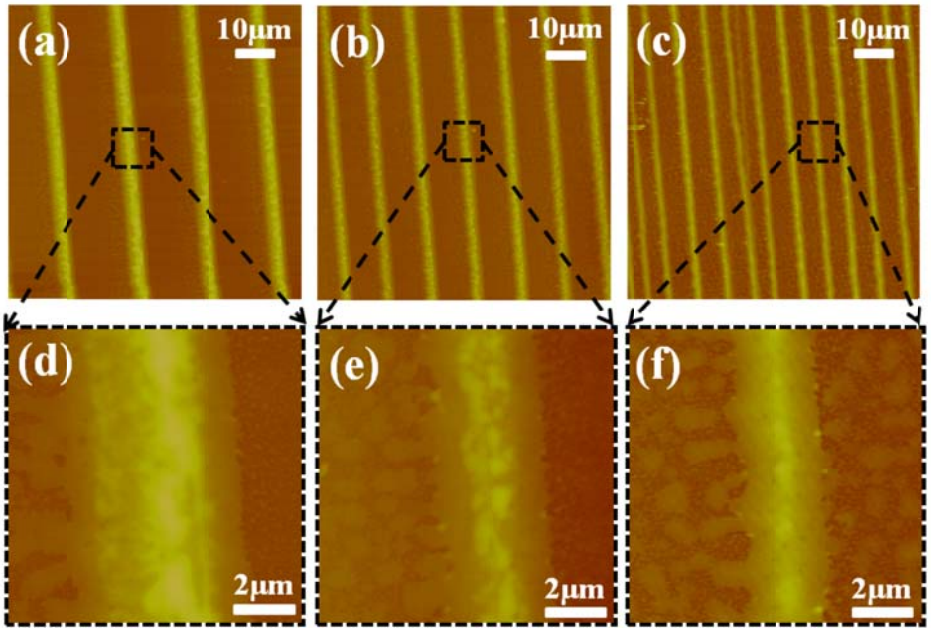

Figure 25. Representative AFM height images at different locations. (a) in the outermost region, X_1, (b) in the intermediate region, X_2, and (c) in the innermost region, X_3. The height, H and the width of stripes, W, and the distance between adjacent stripes, λ, gradually decreased in the three regions. (d)-(f): Close-ups of black boxed areas in (a)-(c), respectively. The featureless morphology was observed. Z range is 200nm in all images.

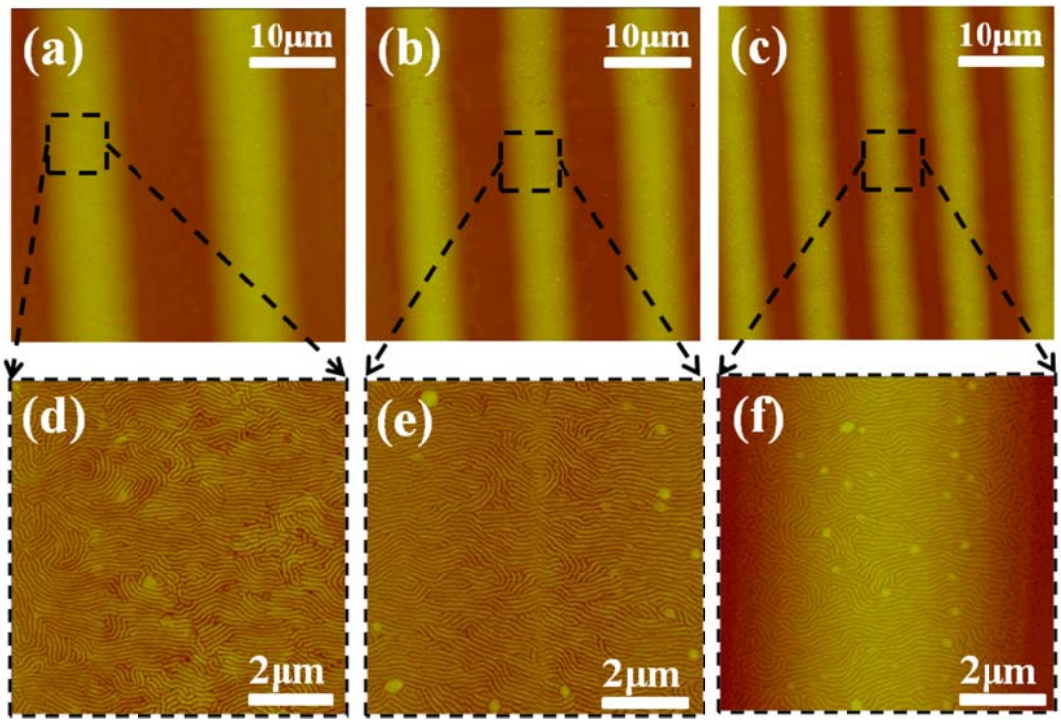

Figure 26. Representative AFM height images of the sample re-examined at the same locations of X_n after the vapor annealing. (a) in the outermost region, X_1, (b) in the intermediate region, X_2, and (c) in the innermost region, X_3. (d)-(f): Close-ups of black boxed areas in (a)-(c), respectively. Within the stripes, vertically oriented lamella nanodomains are clearly evident. Z range is 100nm in all images.

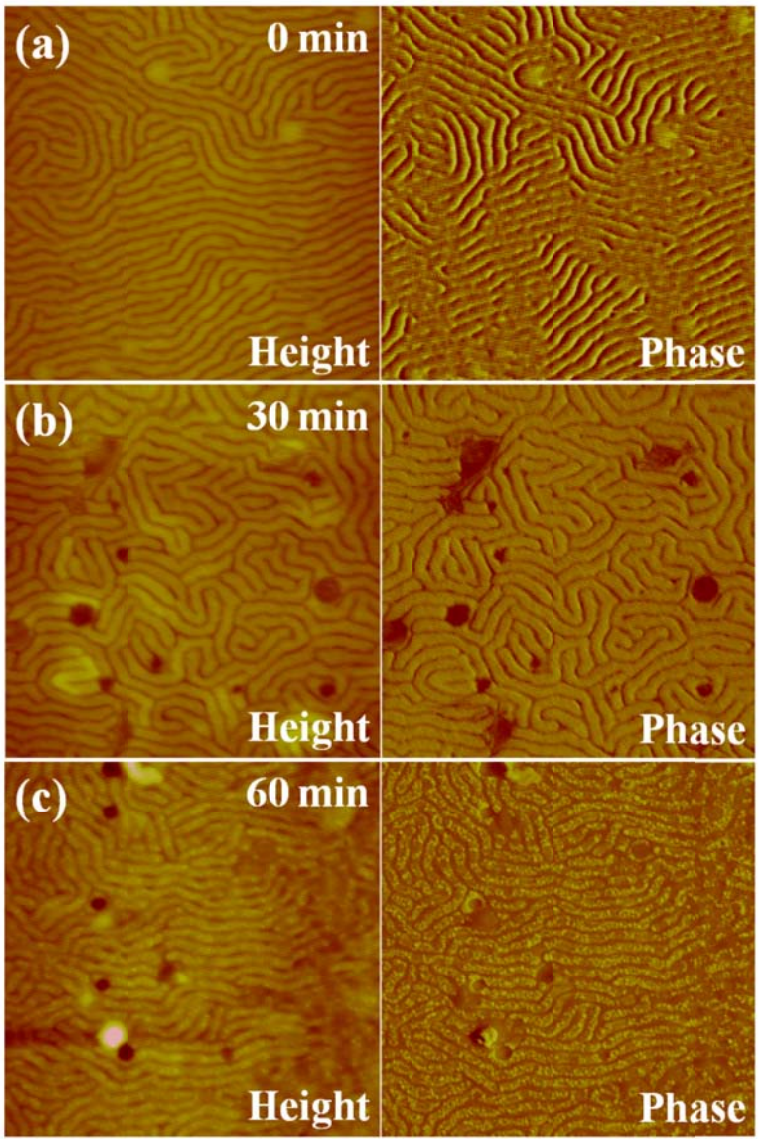

Figure 27. Representative AFM height (left) and phase (right) images of PS-PLA bottlebrush block copolymers. (a) as-prepared sample, (b) after immersing in the degradation solution for 30min, and (c) after immersing for 60min. The surface roughness changed from 1.75nm (as-prepared) to 4.33nm (30-min treatment) to 4.78nm (60-min treatment), indicating the successful removal of PLA arms. Image size = 3μm x 3μm. Z range of height images = 60nm.

Supporting Information

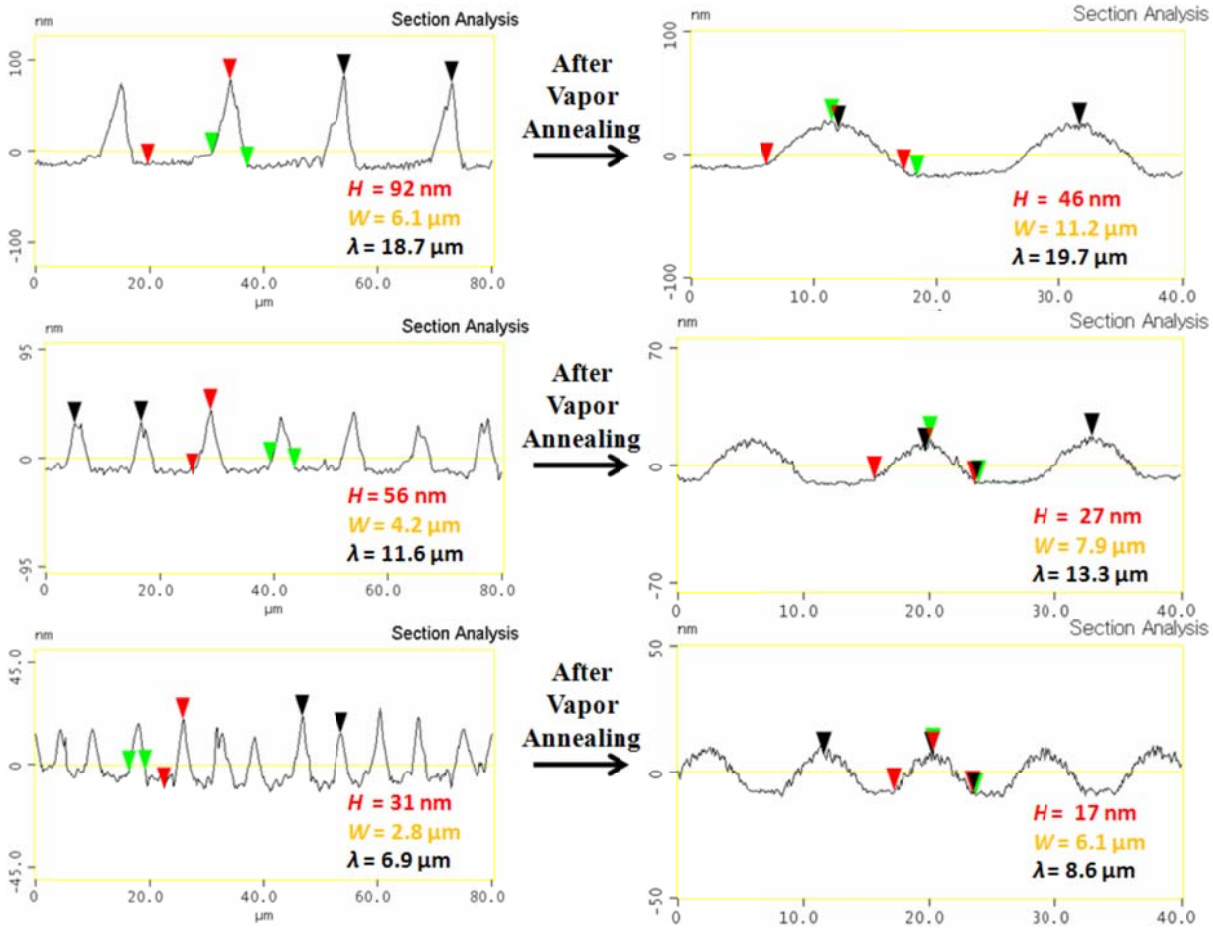

Figure S1. The cross-sectional view of AFM images shows the morphological evolution of the stripe height, *H*, stripe width, *W*, and the spacing between adjacent stripes, λ of PS-PLA stripes before and after the chloroform vapor annealing. The first, second, and third rows correspond to stripes taken in the outermost region, intermediate region, and innermost region, respectively.

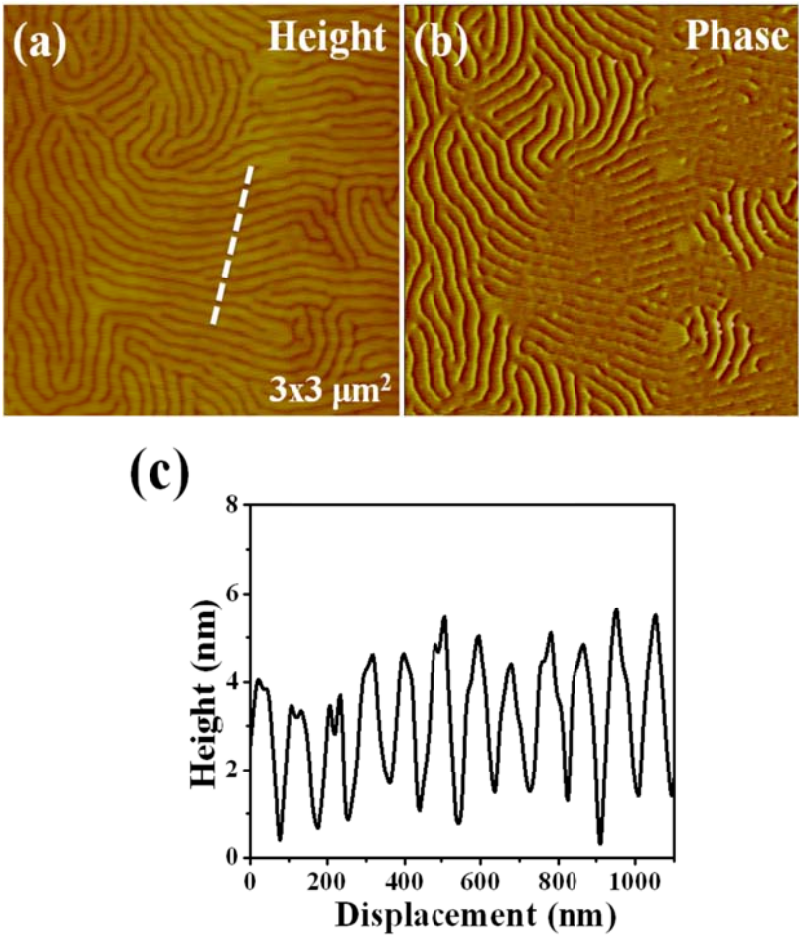

Figure S2. (a) AFM height and (b) phase images of lamellar morphology of PS-PLA within a stripe after the vapor annealing. (c) The cross-section analysis of the surface PS-PLA, corresponding to the white line labeled in (a). The average domain spacing, L_0 = 105 ± 5 nm, measured from the cross-section analysis in (c). Image size = 3μm x 3μm. Z range of the height image = 60nm.

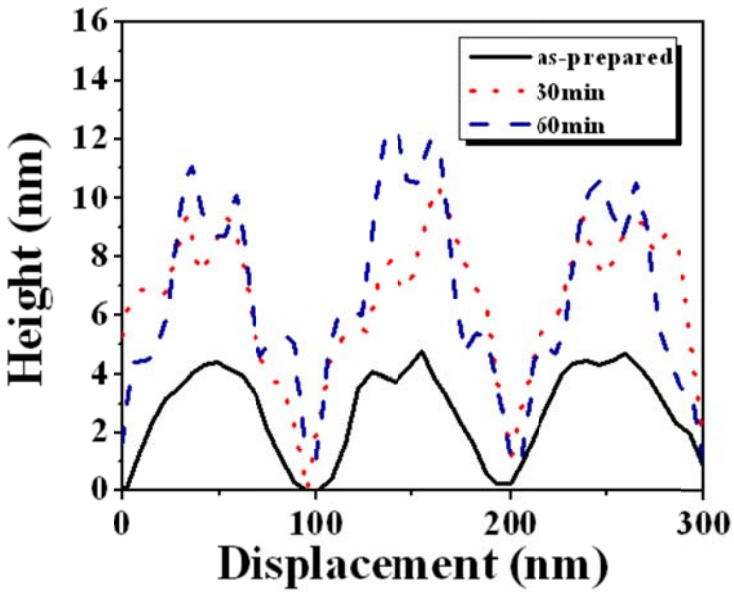

Figure S3. The height profiles for the AFM images shown in Figure 27, corresponding to different solvent vapor annealing times (i.e., as-prepared, 30min and 60min). The nanochannel depth increased with increased vapor annealing time, which is indicative of the successful removal of PLA arms.

References

1. Bigioni, T. P.; Lin, X.-M.; Nguyen, T. T.; Corwin, E. I.; Witten, T. A.; Jaeger, H. M., *Nat Mater* **2006,** *5*, 265-270.
2. Martin, C. P.; Blunt, M. O.; Pauliac-Vaujour, E.; Stannard, A.; Moriarty, P.; Vancea, I.; Thiele, U., *Phys. Rev. Lett.* **2007,** *99*, 116103.
3. Khanal, B.; Zubarev, E., *Angew. Chem. Int. Ed.* **2007,** *119*, 2245-2248.
4. Rabani, E.; Reichman, D. R.; Geissler, P. L.; Brus, L. E., *Nature* **2003,** *426*, 271-274.
5. Mitov, Z.; Kumacheva, E., *Phys. Rev. Lett.* **1998,** *81*, 3427.
6. Hu, H.; Larson, R. G., *Langmuir.* **2005,** *21*, 3963-3971.
7. Prevo, B. G.; Velev, O. D., *Langmuir.* **2004,** *20*, 2099-2107.
8. Hu, H.; Larson, R. G., *J. Phys. Chem. B* **2006,** *110*, 7090-7094.
9. Pauliac-Vaujour, E.; Stannard, A.; Martin, C. P.; Blunt, M. O.; Notingher, I.; Moriarty, P. J.; Vancea, I.; Thiele, U., *Phys. Rev. Lett.* **2008,** *100*, 176102.
10. Byun, M.; Bowden, N. B.; Lin, Z., *Nano Lett.* **2010,** *10*, 3111-3117.
11. Byun, M.; Han, W.; Qiu, F.; Bowden, N. B.; Lin, Z., *Small* **2010,** *6*, 2250-2255.
12. Hong, S. W.; Jeong, W.; Ko, H.; Kessler, M. R.; Tsukruk, V. V.; Lin, Z. Q., *Adv. Funct. Mater.* **2008,** *18*, 2114-2122.
13. Hong, S. W.; Giri, S.; Lin, V. S. Y.; Lin, Z. Q., *Chem. Mater.* **2006,** *18*, 5164-5166.
14. Hong, S. W.; Wang, J.; Lin, Z. Q., *Angew. Chem. Int. Ed.* **2009,** *48*, 8356-8360.
15. Hong, S. W.; Xia, J. F.; Byun, M.; Zou, Q. Z.; Lin, Z. Q., *Macromolecules* **2007,** *40*, 2831-2836.
16. Hong, S. W.; Xia, J. F.; Lin, Z. Q., *Adv. Mater.* **2007,** *19*, 1413.
17. Hong, S. W.; Xu, J.; Xia, J. F.; Lin, Z. Q.; Qiu, F.; Yang, Y. L., *Chem. Mater.* **2005,** *17*, 6223-6226.
18. Xu, J.; Xia, J. F.; Lin, Z. Q., *Angew. Chem. Int. Ed.* **2007,** *46*, 1860-1863.
19. Xu, J.; Xia, J. F.; Hong, S. W.; Lin, Z. Q.; Qiu, F.; Yang, Y. L., *Phys. Rev. Lett.* **2006,** *96*, 066104.
20. Byun, M.; Laskowski, R. L.; He, M.; Qiu, F.; Jeffries-El, M.; Lin, Z. Q., *Soft Matter* **2009,** *5*, 1583-1586.
21. Hong, S. W.; Xu, J.; Lin, Z. Q., *Nano Lett.* **2006,** *6*, 2949-2954.
22. Lin, Z. Q., *J. Polym. Sci., Part B: Polym. Phys.* **2010,** *48*, 2552-2557.
23. Lin, Z. Q.; Granick, S., *J. Am. Chem. Soc.* **2005,** *127*, 2816-2817.
24. Lin, Y.; Boker, A.; He, J.; Sill, K.; Xiang, H.; Abetz, C.; Li, X.; Wang, J.; Emrick, T.; Long, S.; Wang, Q.; Balazs, A.; Russell, T. P., *Nature* **2005,** *434*, 55-59.
25. Maldovan, M.; Thomas, E. L., *Naturet Mater* **2004,** *3*, 593-600.
26. Zalusky, A. S.; Olayo-Valles, R.; Taylor, C. J.; Hillmyer, M. A., *J. Am. Chem. Soc.* **2001,** *123*, 1519-1520.
27. Zalusky, A. S.; Olayo-Valles, R.; Wolf, J. H.; Hillmyer, M. A., *J. Am. Chem. Soc.* **2002,** *124*, 12761-12773.
28. Chen, X.; Rogach, A. L.; Talapin, D. V.; Fuchs, H.; Chi, L., *J. Am. Chem. Soc.* **2006,** *128*, 9592-9593.
29. Rzayev, J., *Macromolecules* **2009,** *42*, 2135-2141.
30. Zhao, L.; Byun, M.; Rzayev, J.; Lin, Z. Q., *Macromolecules* **2009,** *42*, 9027-9033.
31. Deegan, R. D.; Bakajin, O.; Dupont, T. F.; Huber, G.; Nagel, S. R.; Witten, T. A., *Nature* **1997,** *389*, 827-829.

32. Hong, S. W.; Byun, M.; Lin, Z. Q., *Angew. Chem. Int. Ed.* **2009,** *48*, 512-516.
33. Peng, J.; Kim, D. H.; Knoll, W.; Xuan, Y.; Li, B. Y.; Han, Y. C., *J. Chem. Phys.* **2006,** *125*.
34. Xuan, Y.; Peng, J.; Cui, L.; Wang, H.; Li, B.; Han, Y., *Macromolecules* **2004,** *37*, 7301-7307.
35. Olayo-Valles, R.; Guo, S. W.; Lund, M. S.; Leighton, C.; Hillmyer, M. A., *Macromolecules* **2005,** *38*, 10101-10108.
36. Olayo-Valles, R.; Lund, M. S.; Leighton, C.; Hillmyer, M. A., *J. Mater. Chem.* **2004,** *14*, 2729-2731.
37. Cavicchi, K. A.; Berthiaume, K. J.; Russell, T. P., *Polymer* **2005,** *46*, 11635-11639.
38. Yoon, J.-S.; Oh, S.-H.; Kim, M.-N.; Chin, I.-J.; Kim, Y.-H., *Polymer* **1999,** *40*, 2303-2312.
39. Vayer, M.; Hillmyer, M. A.; Dirany, M.; Thevenin, G.; Erre, R.; Sinturel, C., *Thin Solid Films* **2010,** *518*, 3710-3715.
40. Lo, K. H.; Chen, M. C.; Ho, R. M.; Sung, H. W., *Acs Nano* **2009,** *3*, 2660-2666.
41. Lammertink, R. G. H.; Hempenius, M. A.; van den Enk, J. E.; Chan, V. Z. H.; Thomas, E. L.; Vancso, G. J., *Adv. Mater.* **2000,** *12*, 98-103.
42. Ivanisevic, A.; Mirkin, C. A., *J. Am. Chem. Soc.* **2001,** *123*, 7887-7889.

CHAPTER 5. CONTROLLED EVAPORATIVE SELF-ASSEMBLY OF ALL-CONJUGATED POLYMER WITH ENHANCED ELECTRIC CONDUCTIVITY

Modified from a manuscript to be submitted

Wei Han, Ming He, and Zhiqun Lin*

Abstract

Well-organized periodical stripes of conjugated polymers, including poly(3-hexylthiophene) (P3HT), poly(3-butylthiophene) (P3BT), and poly(3-butylthiophene)-b-poly(3-hexylthiophene) (P3BHT)), were formed by repeated "stick-slip" motion of the contact line in a "cylinder-on-Si" geometry. The interfacial interaction between the solute and the substrate effectively mediate the pattern formation. Subsequently, electrical conductivity was found to be significantly improved by chloroform vapor annealing. This facile, one-step deposition technique based on controlled evaporative self-assembly opens up a new avenue for organizing semicrystalline conjugated polymers into two-dimensional ordered patterns in a simple and controllable manner.

Introduction

Conjugated polymers have been widely regarded as promise materials for usage in biosensors, transistors and solar cells.[1, 2] Of the various conjugated polymers, poly(3-alkylthiophene)s (P3ATs) (e.g., P3HT, P3BT) are among the most heavily studied organic conjugated polymers. They have a rather rigid backbone with a regular head-to-tail arrangement of pendant alky side chains that allow for efficient π–π stacking of the

conjugated backbones and solubilization, thus leading to excellent solution processability, chemical stability and high field-effect mobility.[3] The self-organized chains of P3ATs are dramatically influenced by side-chain length, regioregularity, molecular weight, solvent properties, and processing conditions (spin-coating, dip coating and drop casting), resulting in variations of the charge carrier mobility in thin-film transistors by several orders of magnitude.[3-7] Recent advances in synthesis techniques render the design of functional rod-coil or rod-rod block copolymers with specific length scales and geometries. Block copolymers composed of two or more chemically different blocks that are covalently linked are thermodynamically driven to self-assemble into various ordered structures including spheres, cylinders, and lamellae, depending on the volume fraction of the blocks.[8] The self-assembly of block-copolymer chains into nanoscopic ordered domains depends on the ratio of block lengths, strength of interaction, and side-chain groups.[9] Compared with P3AT homopolymers, P3AT rod-rod diblock copolymers (e.g., poly(3-butylthiophene)-b-poly(3-hexylthiophene):P3BHT) has achieved much better balance between the chain flexibility and self-assembly by adjusting the components of alky side chains, resulting in completely different solubilizing and stacking patterns of polymer chains from those of homopolymers. [10, 11] The attempt to rationally design and control the self-assemble of such rod-coil or rod-rod block copolymers in a hierarchical way, on multiple length-scales ranging from nanometers to macroscopic sizes, will open a new avenue to develop economically electronic devices.

In stark contrast to structures formed from a freely evaporating droplet on a substrate (i.e., unconstrained solution), which are often stochastic, lack of regularity, and far from equilibrium (i.e., convection patterns[12, 13], fingering instabilities[14, 15], and

polygonal network structures[16, 17]), the use of controlled evaporative self-assembly (CESA), which can precisely control the evaporation flux, the solution concentration, the interfacial interaction between the solute and substrate, and etc. enables the organization of materials of interest (i.e., polymers, nanoparticles and biomaterials, among others) into complex structures of high fidelity and regularity with engineered optical, electronic, optoelectronic, magnetic properties. [8, 18-33] When compared with conventional techniques (e.g., photolithography, e-beam lithography, soft-lithography, and nanoimprint lithography), CESA is simple, cost-effective, and offers a lithography and external-field-free means of organizing nonvolatile materials into ordered microscopic structures over large surface areas.

Herein, we present a facile and robust method of evaporating conjugated polymers (i.e., poly(3-hexylthiophene) (P3HT), poly(3-butylthiophene) (P3BT), and poly(3-butylthiophene)-b-poly(3-hexylthiophene) (P3BHT; mole ratio: P3HT:P3BT=2:1; Figure 28c) solutions in "cylinder-on-Si" geometries to create highly regular microstructures with large surface areas in a precisely controlled environment. Due to different interfacial interactions between the polymer and the substrate, straight and wave-like stripes were obtained on the silicon surface, respectively. Subsequently, the electrical conductivity of P3BHT was improved significantly after chloroform vapor annealing treatment. This CESA technique, which dispenses with the need for lithography and external fields, is fast, cheap and robust. As such, it represents a powerful strategy for creating highly structured, multifunctional materials and devices.

Experimental Section

Synthesis of conjugated P3HT, P3BT and P3BHT. Regioregular P3BT homopolymer (M_n = 22400 g/mol, PDI = 1.3) and P3HT homopolymer (M_n = 19000 g/mol, PDI = 1.2) were synthesized by a modified Grignard metathesis procedure. P3BHT diblock copolymers, P3BHT21 (P3BT/P3HT block ratio = 2:1 mol/mol, M_n = 8300 g/mol, PDI=1.3), was synthesized by a modified quasi-living chain growth polymerization. The detailed synthesizing procedures can be found in previous works. [39, 42, 43]

Evaporative Self-Assembly of the All-Conjugated Polythiophene Diblock Copolymer Toulene Solution in a "Cylinder-on-Si" Geometry. The above mentioned conjugated polymers were selected as the nonvolatile solute to prepare P3HT, P3BT and P3BHT toluene solution at the concentration 0.15mg mL^{-1} and purified with 200 nm polytetrafluoroethylene (PTFE) filters, respectively. The silicon substrates were cleaned with a mixture of sulfuric acid and Nochromix, then rinsed extensively with deionized (DI) water and blow-dried with N_2. The cylinder lens (L=9.5mm, H=4.0 mm, W=11.0mm, Figure 28b) and silicon substrate were used as the upper and lower surface, respectively, to construct a confined geometry. The "cylinder-on-Si" geometry was placed in a sealed chamber to minimize possible air convection and maintain constant temperature during the evaporation process. The complete evaporation took approximately 30min. After the evaporation was complete, the patterns formed on the Si substrate were examined in this work.

Vapor Annealing Treatment. The regular P3HT, P3BT and P3BHT patterns formed on the Si substrate were exposed to chloroform vapor for a certain period of time (i.e. 6 hours and 12hours) in a closed vessel to achieve morphological reconstruction of

polymers. The small piece of gauze soaked with chloroform solvent was placed into a 33 cm^3 vessel. The vessel was sealed by Teflon and placed in an argon grove box to avoid temperature and humidity variation.

Characterization. The particle patterns were characterized by optical microscopy (Olympus BX51 in the reflection mode) and atomic force microscopy (Dimension 3100 scanning force microscope in the tapping mode (Digital Instruments)). Vista probes (T190) with spring constants $48Nm^{-1}$ were used as scanning probes. WAXD profiles were obtained by using a Bruker D8 Discover Reflector with X-ray generation power of 40kV tube voltage and 40mA tube current. The diffraction was recorded at a θ-2θ symmetry scanning mode with scan angle from $2\theta=4^o$-10^o. Electric properties were measured using a Keithley2400 multisource meter.

Results and Discussion

The choice of P3HT, P3BT and P3BHT (BT: HT=2:1) as the nonvolatile solute was motivated by their promising applications in the solar cells and thin-film transistors with high field-effect mobility. In our experiment, new synthesized P3HT, P3BT and P3BHT diblock copolymers were used as nonvolatile solute to prepare P3HT, P3BT and P3BHT toluene solutions, respectively (See Experiment Section). The concentration of all the solutions was 0.15mg mL^{-1}. The polymer toluene was trapped in the gap between a cylinder lens and a Si substrate, thereby forming a capillary-held microfluid (Fig 1a and Fig 1b), from which toluene was allowed to evaporate only at the capillary edge. Evaporative loss of toluene at the capillary edge caused the pining of the contact line ("stick"), thereby forming the outermost polymer ring. During the deposition process, the

initial contact angle of the meniscus gradually decreased to a critical value, at which the depinning force became larger than the pinning force, causing the contact line jump to a new position ("slip") and arrest again to form a new polymer stripe.[34] Consecutive controlled "stick-slip" cycles of the receding contact line in the symmetric "cylinder-on-Si" geometry yielded rectangle-like deposits globally. The periodical patterns chronicled the moments of arrested contact line motion in the capillary bridge.

After the evaporation was complete, the patterns of P3HT, P3BTand P3BHT formed on the Si substrate were examined by optical microscopy, respectively. Figure 29 shows three typical optical microscopy images of highly ordered, microscopic stripes of P3HT, P3BT and P3BHT formed in the "cylinder-on-Si" geometry. It is noteworthy that the use of confined geometry created highly ordered stripes over large areas. Representative atomic force microscopy (AFM) images taken in three different regions (e.g., X_1-X_3) are shown in Figure 30, respectively. Close examination of the stripes revealed the gradient of the width (ω), the height of stripes (h), and the center-to-center distance ($\lambda_{C\text{-}C}$) between adjacent polymer stripes, which significantly decrease with increasing proximity to the contact center (Along the marked arrows, Table 1). X_n (n ranging from 1 to 3) indicates the position away from the cylinder/Si contact center (i.e. X_1=4500μm, X_2=4000μm, X_3=3500μm). The gradient dimension of the stripes can be attributed to the competition between the linear pinning force and the nonlinear capillary force and the decrease in the height of meniscus of the solution due to the curved surface topology of cylinder of the solvent evaporated.[34]

Quite interesting, it is noteworthy to observe the straight stripes of P3BT and the stripes together with the instability fingers in P3HT and P3BHT. Since the solution

concentration (0.15mg mL^{-1}), the loading volume (30μL) and the solvent (toluene) were kept the same for P3HT, P3BT and P3BHT solutions, the difference in resulting surface patterns of P3HT, P3BT and P3BHT can be attributed to different interfacial interaction between the polymer and the substrate. The observation resembled our pervious study in drying-mediated self-assembly of polystyrene (PS) and poly(methyl methacrylate) (PMMA).[31] Increasing the side-chain from butyl to hexyl increases the contact angle of water on conjugated polymer films (which means, more hydrophobic). As a result, when deposited these conjugated polymers on hydrophilic native silicon oxide surface, P3HT and the substrate has higher interfacial energy.[35] This unfavorable interfacial interaction between P3HT and the substrate is crucial in forming fingering instabilities. Moreover, the P3HT chains do not entangle one another due to their rigid rod-like nature, and the MW of the P3HT was quite low. Taken together, P3HT fingers can be easily formed.[21] In contrast, compared to P3HT, higher MW of P3BT and lower surface energy on the substrate make the stripe like rings without fingering instabilities finally formed. When incorporate part of P3HT into P3HT to form the P3BHT diblock copolymers, the fingering instabilities were retained due to the existence of the P3HT part (Fig 2c and Fig3 g-i). The result was also resembled our pervious PS-b-PMMA study. [31]

An important usage of the patterned P3AT stripes is to create large-area stripe like deposits with well-defined molecular architecture, resulting in higher crystallinity, ordered morphology and thus enhanced electricity conductivity. Solvent-annealing method has been regarded as one of the most successful post-treatment to achieve morphological rearrangement of nanodomains within microscopic straight stripes.[8] Proper solvent-annealing process can highly improve the ordered packing of P3AT

chains, thus resulting in improved electrical performance.[36] In this work, P3AT stripes deposited on the silicon substrate were sealed in chloroform vapor for 6h and 12h, respectively. The selection of chloroform vapor annealing is due to the good solubility of P3AT chains in chloroform, which tend to form a more thermodynamically favorable crystal structure consisting of edge-on side chains and parallel π~π stacking planes with respect to the substrate.[37]

After chloroform solvent vapor annealing for 6h and 12h, no obvious topological changes on the surface patterns were observed as shown in Figure S4. Close examination of the stripes by phase AFM revealed the phase separation of P3AT nanodomains within the stripes changed with varying duration of chloroform vapor annealing (Figure 31). P3AT is a commonly studied semicrystal polymer, and AFM images are commonly used to describe the domain size and the crystallinity. It is necessary to note that, AFM does not measure crystallinity directly, but instead measures the morphology of the surface. Since P3AT crystals tend to have well-defined shapes due to its rigid thienyl rings, bright domain structures observed in AFM images are often assumed to represent crystals.[38] As shown on Figure 31, P3HT presented typical nodule-like morphology after complete evaporation of toluene leading to the formation of stripes, and no obvious changes in the crystal morphology and domain size after subsequent chloroform-vapor annealing for 6h and 12h, which seems to imply that the crystallinity did not significantly change during the vapor annealing. Similar crystal morphology was observed in P3BT stripes, but the crystal domains size decreased accompanying the increased chloroform vapor-annealing duration as the interspace between P3BT crystal domains extended much larger after vapor annealing for 12h, indicating that the crysallinity of P3BT within the stripes

decreased during the vapor annealing. In comparison with those of P3HT and P3BT, P3BHT showed clearly nanowire morphology with apparent structure after evaporation of toluene, which was also reported in low-MW P3HT films.[38](Fig 4, Bottom left) Quite intriguingly, the nanowire morphology grew into nodule-like morphology when treating P3BHT stripes under chloroform vapor for 6h, and the nodule-like packed much closer when extending the vapor annealing to 12h. It is believed that nodule-like crystals are the aggregation of more polymer chains than nanowire crystals in P3HT, which can be viewed as evidence that chloroform vapor annealing effectively improve the crystallinity of P3BHT chains and promote the rearrangement of P3BHT nanodomains within the stripes at the nanometer scale. [38]

To further verify the molecular packing and crystallinity of P3HT, P3BT and P3BHT before and after chloroform vapor annealing, all the stripe films were characterized by XRD after AFM scanning as shown in Figure 32. All the XRD patterns obtained from P3HT, P3BT and P3BHT indicated that the P3AT homopolymers and diblock copolymer followed the typical edge-on orientation in which the thienyl backbones were aligned parallel to the substrates, consistent with those reported in our previous work.[39] The XRD patterns of P3HT, P3BT and P3BHT were all measured on the same films before and after vapor annealing, respectively, so that the intensities of the [100] peaks of them were nearly proportional to the number of polymer crystallites per unit volume in the films, which can be used to compare the changes in crystallinity. The intensity of P3BT peaks decreased with the duration of chloroform vapor annealing, which corresponded well with the reduction of crystal domain in the AFM phase images, suggesting that chloroform tended to dissolve P3BT chains instead of promoting them to

crystalize. In contrast, an increment in the [100] peaks of P3BHT were observed , which also agreed with the observed increasing crystal domains in the AFM results, pointing out that the crystal morphology change from nanowires to nodule-like aggregations was accompanied with increase in crystallinity. Therefore, it is demonstrated that chloroform vapor annealing may further promote the rearrangement of P3BHT nanodomains within the stripes at the nanometer scale. In contrast, we cannot observe clearly changing trends of P3HT peaks, which is corresponding to the unobvious change of crystal domain size in the AFM images we discussed above.

It would be of interest to verify whether the increased crystallinity of P3BHT could really contribute to significantly increase of the electric conductivity within the stripes. The current measurements (with constant applied voltage) of the stripes before and after vapor annealing were measured in situ on the silicon template as shown in Figure 33a, which contains two golden electrodes with 10μm blank gap. CSEA experiment was directly performed on the template, instead of silicon substrate we used before. As illustrated in Figure 33b, the contacts between the stripes and golden electrodes are Ohmic contacts. All stripe films exhibited good electrical conductivity, especially for the P3BT films due to its short alkyl-side chains and therefore enhanced crystallinity.[40, 41] It was interesting to observed that, the current (*i.e.,* 10 V voltage was applied) of P3BHT stripes measured substantially increases with increased treatment time of the vapor annealing, and even much higher than that of P3BT without annealing. For the almost unchanged cross-section of the stripes before and after the vapor annealing (see Supporting Information, Fig S4), we can ignore the shape effect between the measurements. This observation unambiguously confirms that the increased P3BHT

crystallinity via the method introduced in this work would significantly improve electric conductivity of the stripes, which demonstrates a rational reconstruct over the P3BHT nanostructures in the stripes resulting in optimized morphologies and electronic properties. In contrast, the currents measurements of P3HT and P3BT are almost unchanged and decreased, respectively, which are also corresponding to the decreased crystallinity of P3BT and unchanged crystallinity of P3HT conclude from the AFM phase image and XRD data. Now a rapid and cheap two-step process towards forming well-ordered structures over large areas for possible technological applications were realized, including the formation of large-area functional P3BHT block copolymer stripes and the post-treatment of the stripes using vapor annealing to promote reorganization of P3BHT nanodomains within the microscopic stripes, resulting in highly enhanced electrical conductivity.

Conclusions

In summary, we have demonstrated that well-ordered polymer stripes can be produced by subjecting the P3AT toluene solution to evaporation in an axially symmetric "cylinder-on-Si" geometry. These complex self-assembled structures were the direct consequence of interplay between controlled "stick-slip" motion of the contact line and the phase separation of polymers. Furthermore, morphological rearrangement of nanodomains within microscopic straight stripes was achieved with subsequent chloroform vapor annealing. Different crystallinity and morphology of P3AT could significantly affect the electric conductivity within the stripes. The approach of controlled evaporative self-assembly (CESA) represents a powerful strategy for creating highly

structured, multifunctional materials and devices for potential applications in optoelectronics, photonics, and biosensors.

Figures

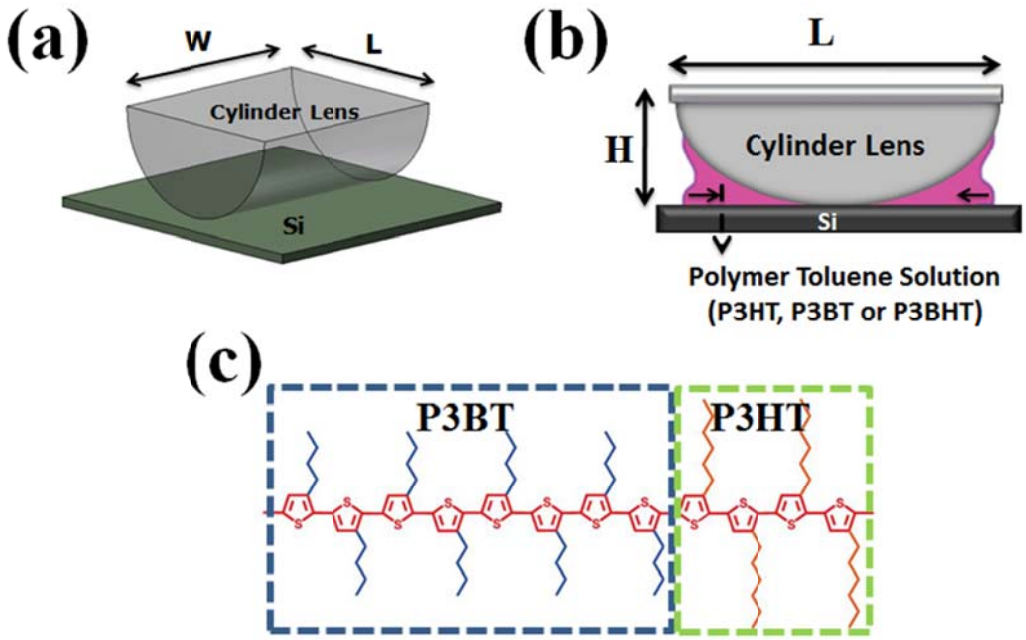

Figure 28. Schematic representation of the formation of P3AT stripes. A drop of P3AT toluene solution was trapped in a confined geometry consisting of a cylinder-shaped lens on a flat Si substrate, forming a capillary-held solution. (a) 3D view and (b) Side view of "cylinder-on-flat" system. H, L, and W are the height, length, and width of cylinder lens, respectively. The black arrows mark the movement of the solution front toward the cylinder/Si contact center. (c) Chemical structure of P3BHT (mole ratio: P3HT:P3BT=2:1) diblock copolymer.

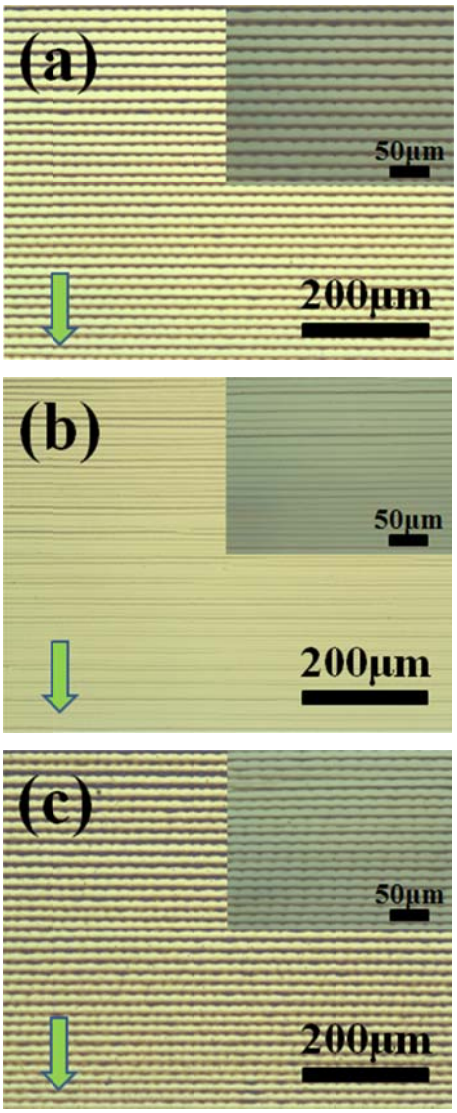

Figure 29. Optical micrograph images of P3AT stripes formed by evaporative self-assembly in a cylinder-on-Si geometry. The concentration of all the solutions was 0.15mg mL^{-1}. (a) P3HT; (b) P3BT; (c) P3BHT; Arrays mark the moving direction of the solution front during the course of evaporation.

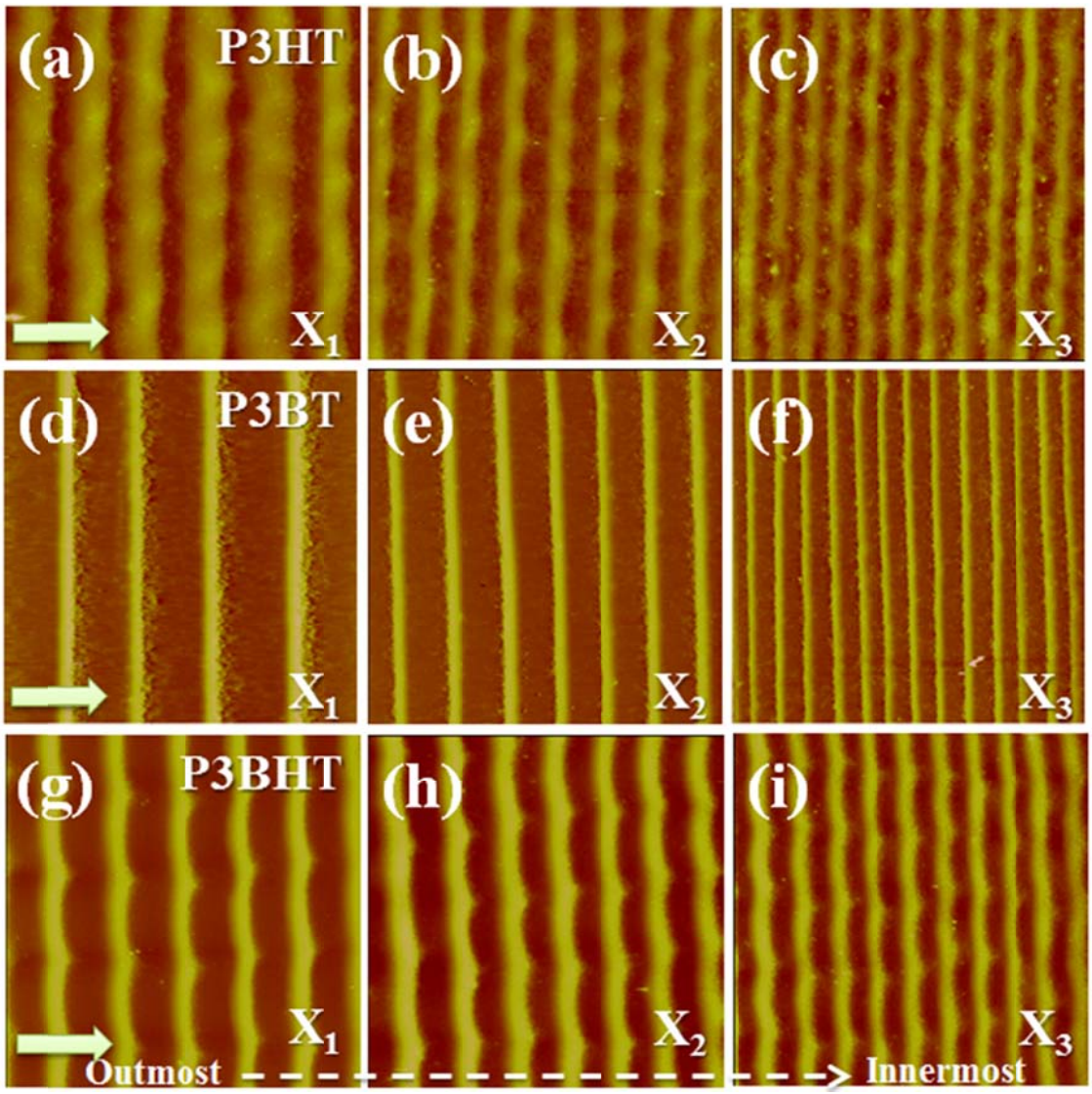

Figure 30. Representative AFM height images taken in three different regions (e.g., X_1-X_3) of P3AT stripes. (a)-(c) P3HT; (d)-(f) P3BT; (g)-(I) P3BHT.X_1, X_2, X_3 are outmost region, intermediate region, innermost region, respectively. Image size: 80x80μm. Z range: (a),(d),(g) are 400nm; (b),(e),(h) are 300nm, (c),(f),(i) are 200nm.

Table 1: The width (ω), the height of stripes (h), and the center-to-center distance ($\lambda_{C\text{-}C}$) between adjacent polymer stripes significantly decreased with increasing proximity to the contact center (from X_1 to X_3). Dates are obtained from AFM images in Figure2.

P3AT	Outmost (X_1)			Intermediate(X_2)			Innermost(X_3)		
	Width (μm)	Height (nm)	$\lambda_{C\text{-}C}$ (μm)	Width (μm)	Height (nm)	$\lambda_{C\text{-}C}$ (μm)	Width (μm)	Height (nm)	$\lambda_{C\text{-}C}$ (μm)
P3HT	11.8	80.4	12.2	5.2	62.2	9.8	3.6	43.6	6.0
P3BT	4.2	165.4	18.8	2.8	98.8	10.8	3.8	52.8	6.1
P3BHT	5.1	142.2	15.6	4.7	102.6	12.0	3.2	61.2	7.8

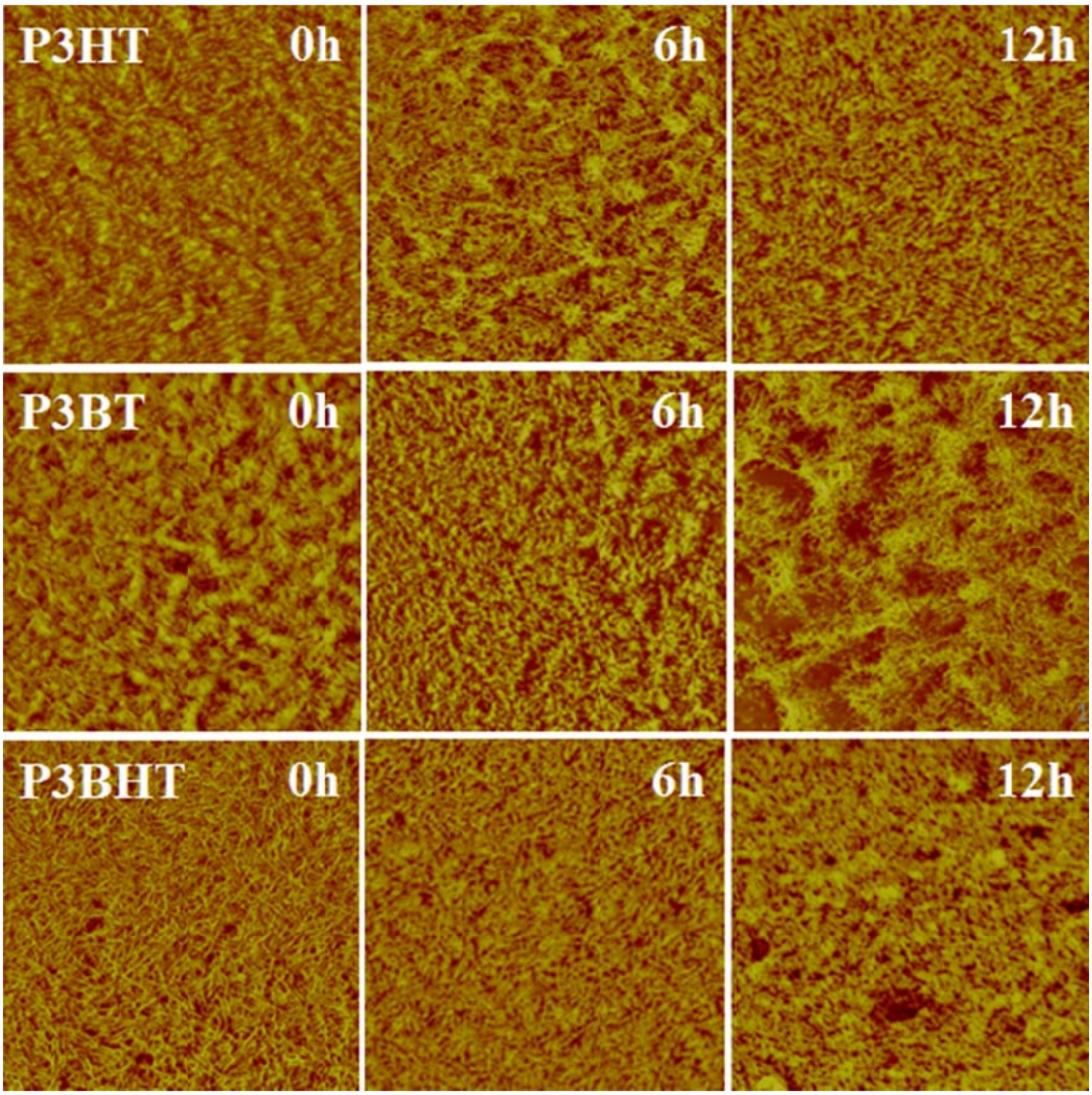

Figure 31. Representative AFM phase images within P3AT (P3HT, P3BT and P3BHT) stripes changed with varying duration of chloroform vapor annealing. Top line: P3HT from 0h-12h. Middle line: P3HT from 0h-12h. Bottom line: P3BHT from 0h-12h. Image Size: 1.5x1.5μm.

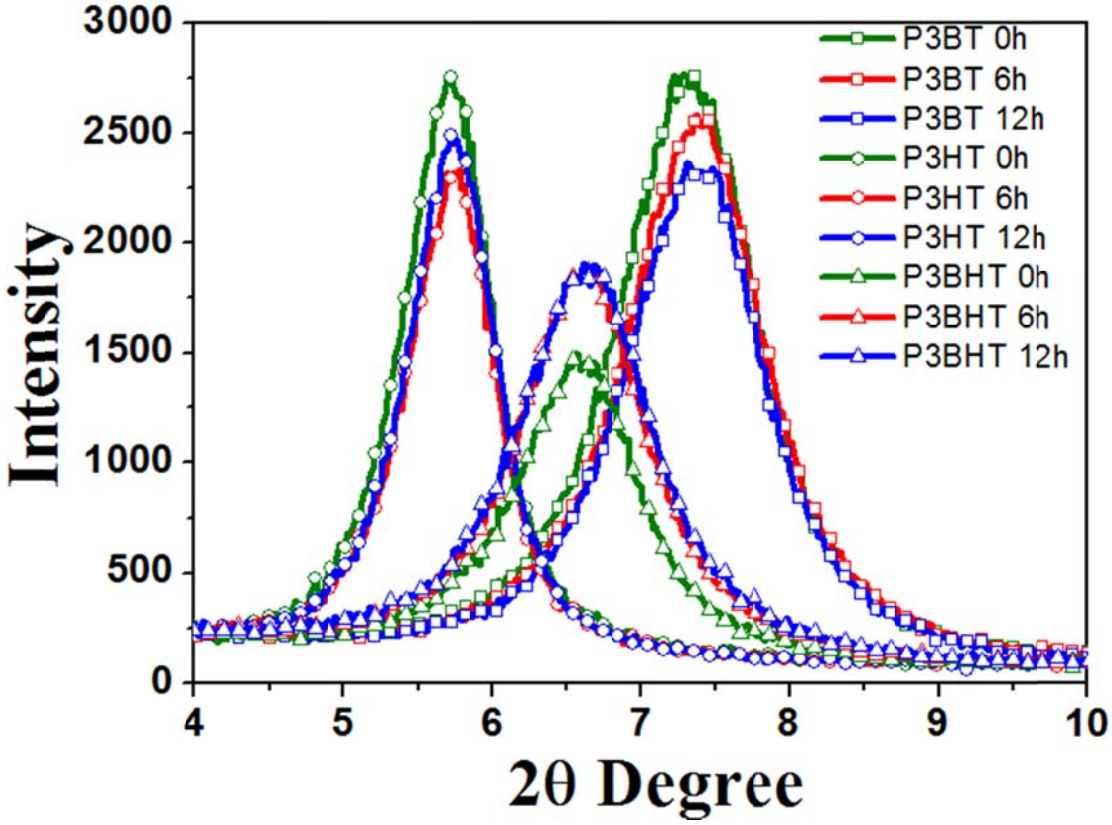

Figure 32. XRD patterns of P3AT stripes with varying duration of chloroform vapor annealing (0h, 6h and 12h). All the XRD patterns indicated that the P3AT homopolymers and diblock copolymer followed the typical edge-on orientation in which the thienyl backbones were aligned parallel to the substrates

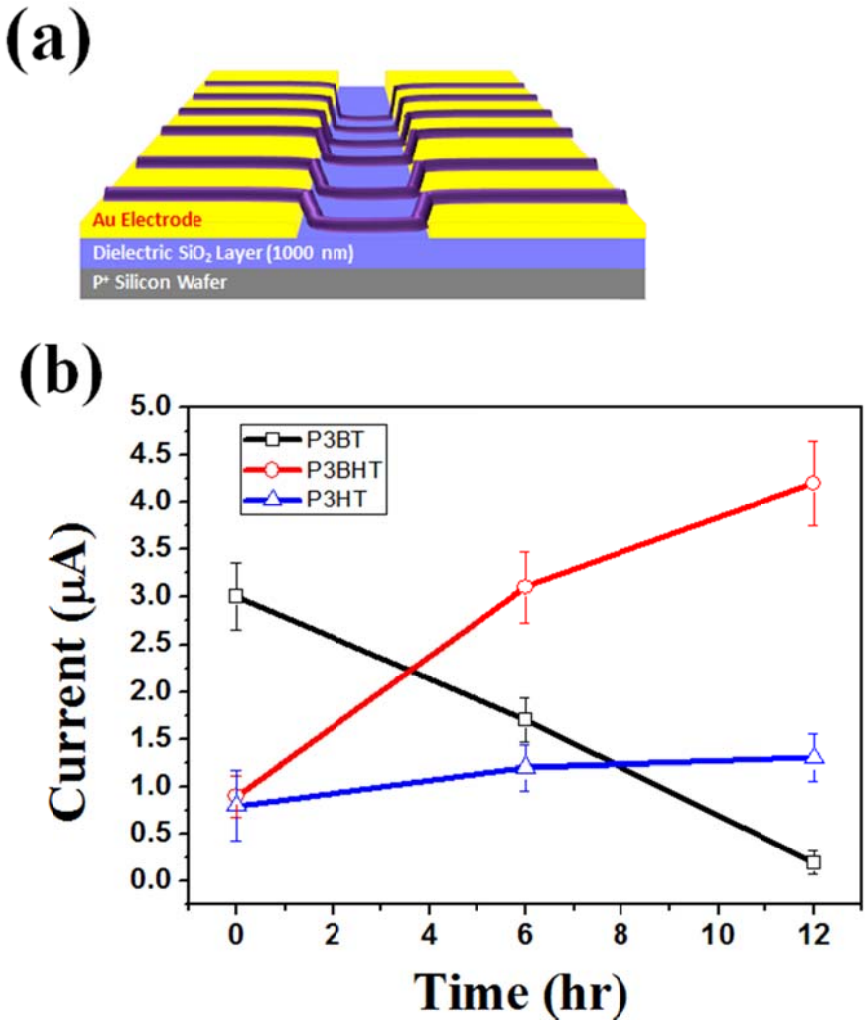

Figure 33. The electric conductivity of P3HT, P3BT and P3BHT with different vapor annealing time. (a) Schematic representation of the electric conductivity measurement. The CSEA experiment was repeated on the template, instead silicon substrate used before. (b) The measurement of the currents from the equipment when applied 10V voltage with diffrenent samples, with varying duration of chloroform vapor annealing (0h, 6h and 12h).

Supporting Information:

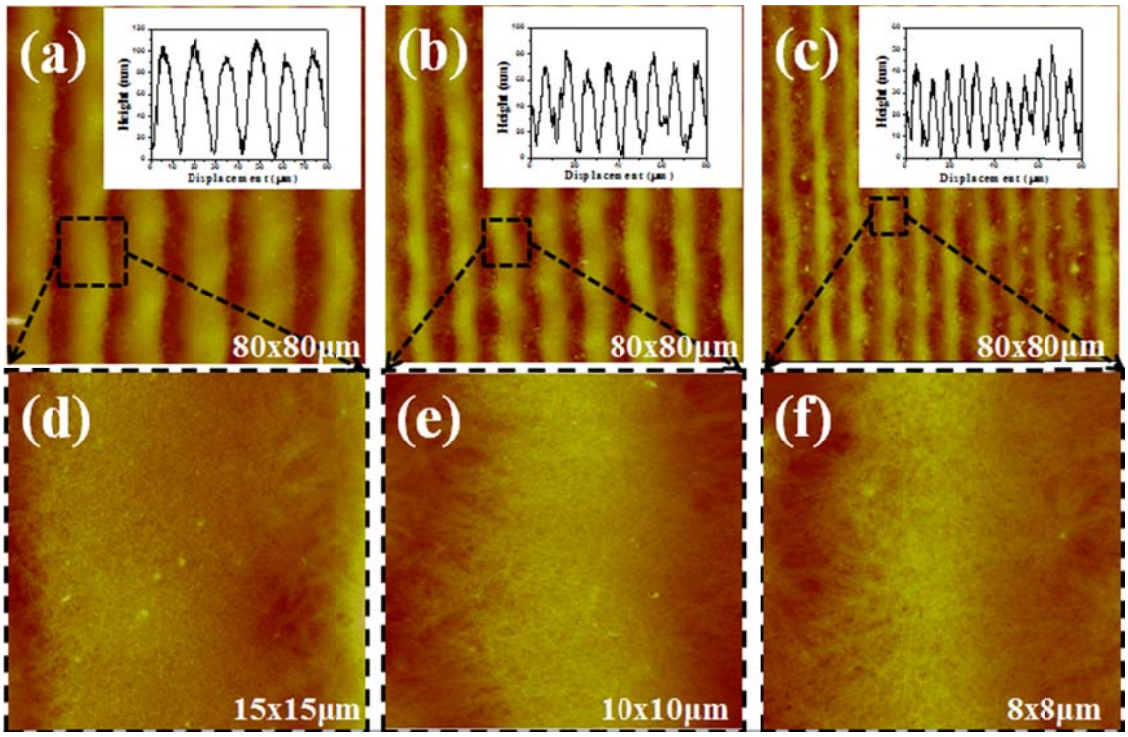

Figure S1. Representative AFM height (a, b, c) and corresponding zoom in images (d, e, f) of P3HT. (a) Outmost region (X_1). (b) Intermediate region (X_2). (c) Innermost region (X_3). The distance between adjacent stripes, the height of stripes, and the width of stripes gradually decreased at the three regions. Inset images are the height profiles of the stripes.

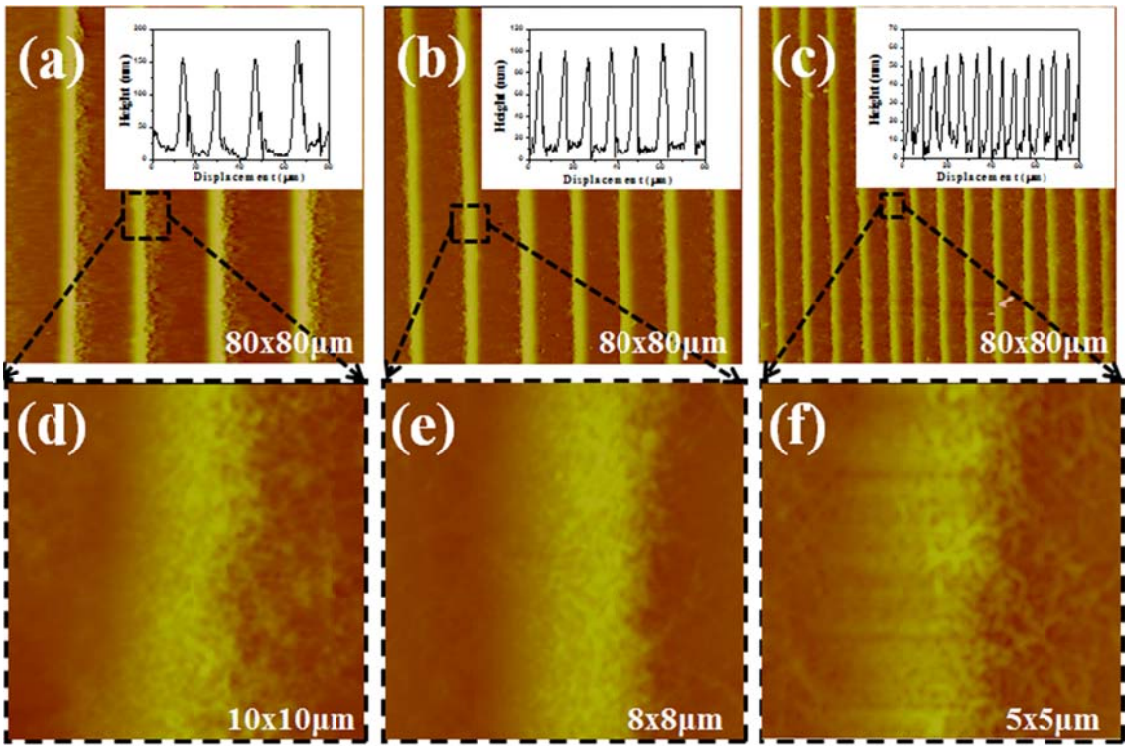

Figure S2. Representative AFM height (a, b, c) and corresponding zoom in images (d, e, f) of P3BT. (a) Outmost region (X_1). (b) Intermediate region (X_2). (c) Innermost region (X_3). The distance between adjacent stripes, the height of stripes, and the width of stripes gradually decreased at the three regions. Inset images are the height profiles of the stripes.

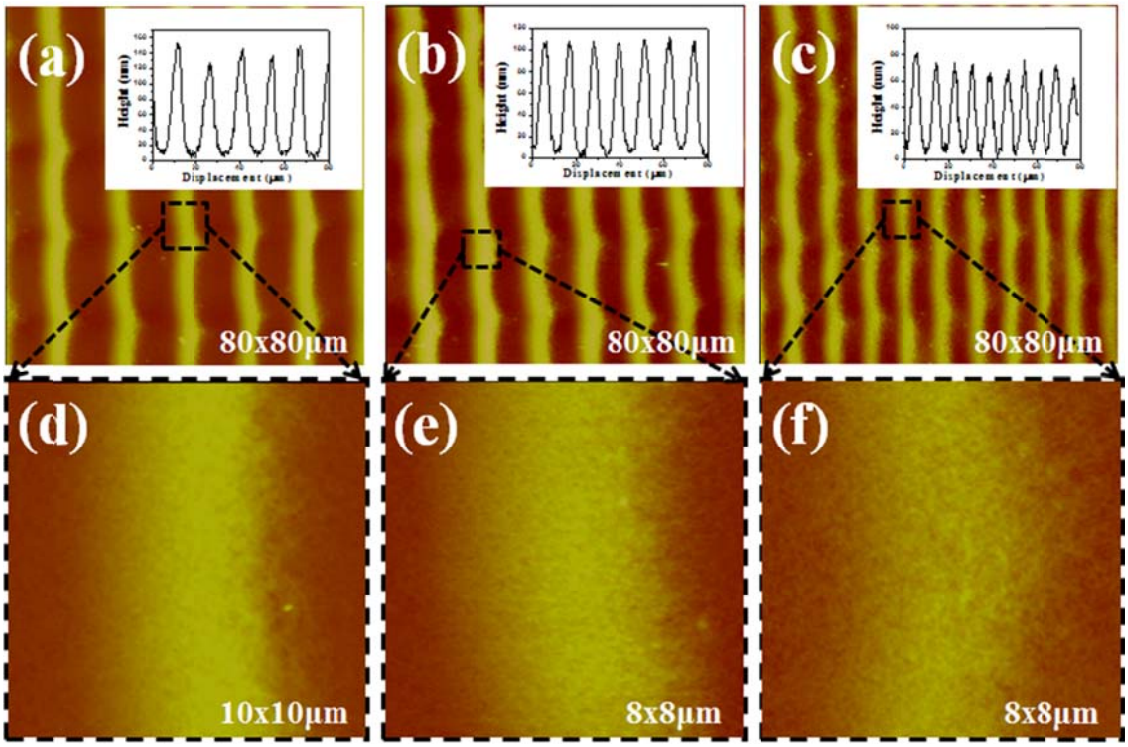

Figure S3. Representative AFM height (a, b, c) and corresponding zoom in images (d, e, f) of P3BHT. (a) Outmost region (X_1). (b) Intermediate region (X_2). (c) Innermost region (X_3). The distance between adjacent stripes, the height of stripes, and the width of stripes gradually decreased at the three regions. Inset images are the height profiles of the stripes.

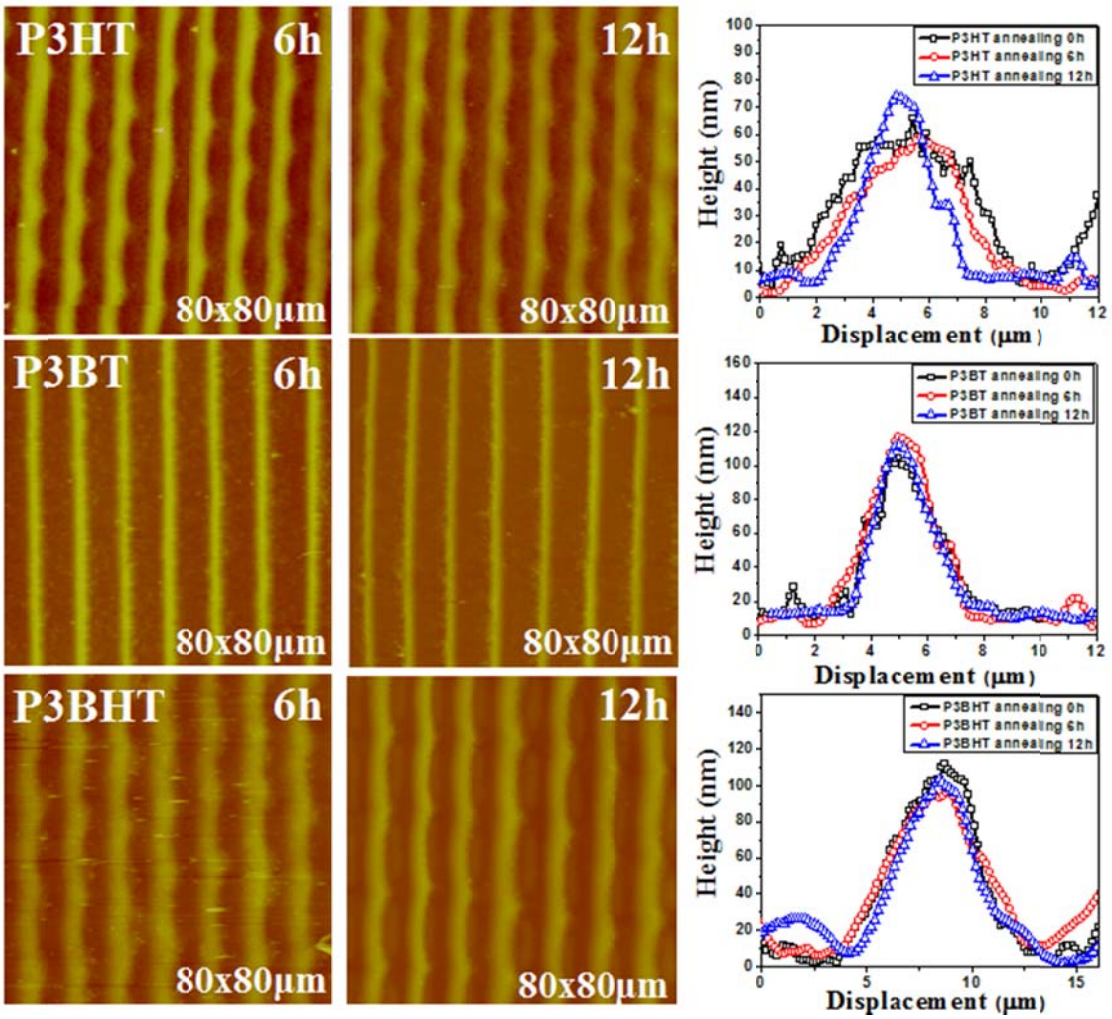

Figure S4. Representative AFM height images and corresponding height profiles of one stripe with different annealing time. Top line: P3HT from 0h-12h. Middle line: P3HT from 0h-12h. Bottom line: P3BHT from 0h-12h. No obvious topological changes on the surface patterns were observed before and after the vapor annealing.

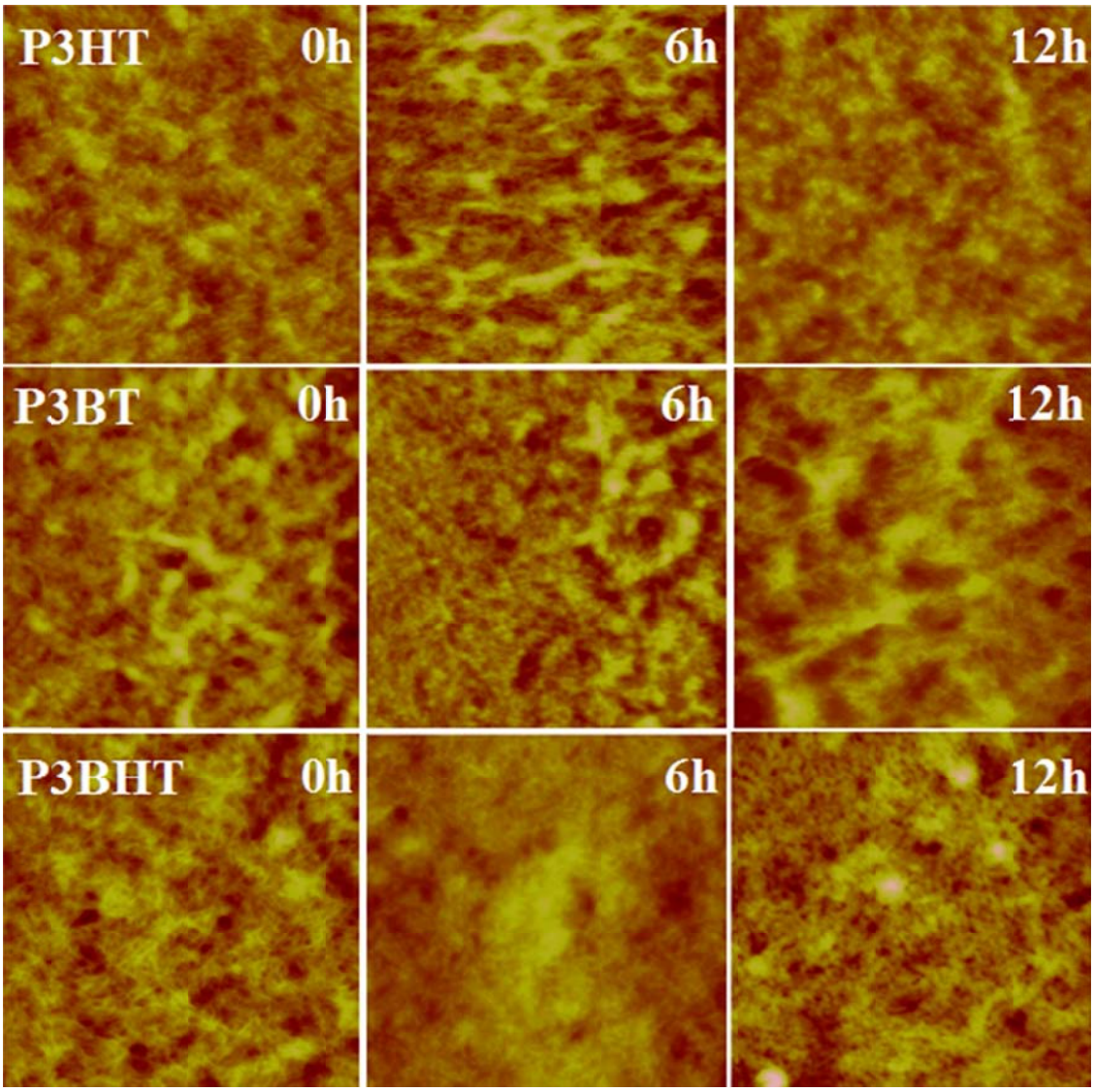

Figure S5. Representative AFM height images within P3AT stripes with varying duration of chloroform vapor annealing, which is corresponding to the phase images in Figure 31. Top line: P3HT from 0h-12h. Middle line: P3HT from 0h-12h. Bottom line: P3BHT from 0h-12h. Image Size: 1.5x1.5μm.

Reference:

1. Xu, J.; Wang, J.; Mitchell, M.; Mukherjee, P.; Jeffries-El, M.; Petrich, J. W.; Lin, Z. Q., *J. Am. Chem. Soc.* **2007,** *129* (42), 12828-12833.
2. Lin, Z. Q., *Chem-eur. J.* **2008,** *14* (21), 6294-6301.
3. Bao, Z.; Dodabalapur, A.; Lovinger, A. J., *Appl. Phys. Lett.* **1996,** *69* (26), 4108-4110.
4. Joseph Kline, R.; McGehee, M. D.; Toney, M. F., *Nat Mater* **2006,** *5* (3), 222-228.
5. Kline, R. J.; McGehee, M. D.; Kadnikova, E. N.; Liu, J.; Fréchet, J. M. J., *Adv. Mater.* **2003,** *15* (18), 1519-1522.
6. Zhang, R.; Li, B.; Iovu, M. C.; Jeffries-El, M.; Sauvé, G.; Cooper, J.; Jia, S.; Tristram-Nagle, S.; Smilgies, D. M.; Lambeth, D. N.; McCullough, R. D.; Kowalewski, T., *J. Am. Chem. Soc.* **2006,** *128* (11), 3480-3481.
7. Sirringhaus, H.; Brown, P. J.; Friend, R. H.; Nielsen, M. M.; Bechgaard, K.; Langeveld-Voss, B. M. W.; Spiering, A. J. H.; Janssen, R. A. J.; Meijer, E. W.; Herwig, P.; de Leeuw, D. M., *Nature* **1999,** *401* (6754), 685-688.
8. Byun, M.; Bowden, N. B.; Lin, Z., *Nano Lett.* **2010,** *10* (8), 3111-3117.
9. Botiz, I.; Darling, S. B., *Materials Today* **2010,** *13* (5), 42-51.
10. He, M.; Han, W.; Ge, J.; Yang, Y.; Qiu, F.; Lin, Z., *Energy & Environmental Science* **2011,** *4* (8), 2894-2902.
11. Loewe, R. S.; Khersonsky, S. M.; McCullough, R. D., *Adv. Mater.* **1999,** *11* (3), 250-253.
12. de Gennes, P. G., *Eur. Phys. J. E* **2001,** *6* (5), 421-424.
13. Bormashenko, E.; Pogreb, R.; Stanevsky, O.; Bormashenko, Y.; Stein, T.; Gaisin, V.-Z.; Cohen, R.; Gendelman, O. V., *Macromol. Mater. Eng.* **2005,** *290* (2), 114-121.
14. Karthaus, O.; Grasjo, L.; Maruyama, N.; Shimomura, M., *Chaos* **1999,** *9* (2), 308-314.
15. Cazabat, A. M.; Heslot, F.; Troian, S. M.; Carles, P., *Nature* **1990,** *346* (6287), 824-826.
16. Nguyen, V. X.; Stebe, K. J., *Phys. Rev. Lett.* **2002,** *88* (16), 164501.
17. Maillard, M.; Motte, L.; Pileni, M. P., *Adv. Mater.* **2001,** *13* (3), 200-204.
18. Byun, M.; Han, W.; Qiu, F.; Bowden, N. B.; Lin, Z. Q., *Small* **2010,** *6*, 2250.
19. Byun, M.; Hong, S. W.; Qiu, F.; Zou, Q.; Lin, Z., *Macromolecules* **2008,** *41*, 9312.
20. Byun, M.; Hong, S. W.; Zhu, L.; Lin, Z. Q., *Langmuir.* **2008,** *24*, 3525.
21. Byun, M.; Laskowski, R. L.; He, M.; Qiu, F.; Jeffries-EL, M.; Lin, Z. Q., *Soft Matter* **2009,** *5*, 1583.
22. Byun, M.; Wang, J.; Lin, Z., *J. Phys.: Cond. Matt.* **2009,** *21*, 264014.
23. Byun, M.; Wang, J.; Lin, Z., *Acta Phys. -Chim. Sin.* **2009,** *25*, 1249.
24. Han, W.; Byun, M.; Lin, Z., *J. Mater. Chem.* **2011,** *21* (42), 16968-16972.
25. Han, W.; Byun, M.; Zhao, L.; Rzayev, J.; Lin, Z., *J. Mater. Chem.* **2011,** *21* (37), 14248-14253.
26. Hong, S. W.; Byun, M.; Lin, Z. Q., *Angew. Chem., Int. Ed.* **2009,** *48*, 512.
27. Hong, S. W.; Giri, S.; Lin, V. S. Y.; Lin, Z. Q., *Chem. Mater.* **2006,** *18* (22), 5164-5166.
28. Hong, S. W.; Jeong, W.; Ko, H.; Kessler, M. R.; Tsukruk, V.; Lin, Z. Q., *Adv. Funct. Mater.* **2008,** *18*, 2114

29. Hong, S. W.; Wang, J.; Lin, Z. Q., *Angew. Chem., Int. Ed.* **2009,** *48*, 8356.
30. Hong, S. W.; Xia, J.; Byun, M.; Zou, Q.; Lin, Z. Q., *Macromolecules* **2007,** *40*, 2831.
31. Hong, S. W.; Xia, J. F.; Lin, Z. Q., *Adv. Mater.* **2007,** *19* (10), 1413-+.
32. Hong, S. W.; Xu, J.; Lin, Z. Q., *Nano Lett.* **2006,** *6* (12), 2949-2954.
33. Hong, S. W.; Xu, J.; Xia, J.; Lin, Z. Q.; Qiu, F.; Yang, Y. L., *Chem. Mater.* **2005,** *17*, 6223.
34. Xu, J.; Xia, J. F.; Hong, S. W.; Lin, Z. Q.; Qiu, F.; Yang, Y. L., *Phys. Rev. Lett.* **2006,** *96* (6).
35. Robinson, L.; Isaksson, J.; Robinson, N. D.; Berggren, M., *Surf. Sci.* **2006,** *600* (11), L148-L152.
36. Tang, H.; Lu, G.; Li, L.; Li, J.; Wang, Y.; Yang, X., *J. Mater. Chem.* **2010,** *20* (4), 683-688.
37. Yang, H. H.; LeFevre, S. W.; Ryu, C. Y.; Bao, Z. N., *Appl. Phys. Lett.* **2007,** *90* (17).
38. Salleo, A.; Kline, R. J.; DeLongchamp, D. M.; Chabinyc, M. L., *Adv. Mater.* **2010,** *22* (34), 3812-3838.
39. Ge, J.; He, M.; Qiu, F.; Yang, Y., *Macromolecules* **2010,** *43* (15), 6422-6428.
40. Lu, G. H.; Tang, H. W.; Huan, Y. A.; Li, S. J.; Li, L. G.; Wang, Y. Z.; Yang, X. N., *Adv. Funct. Mater.* **2010,** *20* (11), 1714-1720.
41. Lu, G. H.; Li, L. G.; Yang, X. N., *Adv. Mater.* **2007,** *19* (21), 3594-+.
42. He, M.; Zhao, L.; Wang, J.; Han, W.; Yang, Y. L.; Qiu, F.; Lin, Z. Q., *Acs Nano* **2010,** *4* (6), 3241-3247.
43. He, M.; Ge, J.; Fang, M.; Qiu, F.; Yang, Y. L., *Polymer* **2010,** *51* (10), 2236-2243.

CHAPTER 6. SIMPLE ROUTE TO METAL OXIDE STRIPES VIA CONTROLLED EVAPORATIVE SELF-ASSEMBLY

Modified from a manuscript to be submitted

Wei Han, Chuanbing Tang, and Zhiqun Lin*

Abstract

Highly-ordered gradient stripes of a new synthesized side-chain ferrocene-containing polymer, poly 2-(metharcryloyloxy) ethyl ferrocenecarboxylate (PAMEFC), with remarkable regularity over large areas were obtained by controlled evaporation process of confined microfluid in a cylinder-on-Si geometry, which produced periodic "stick-slip" motions at the three-phase contact line. Subsequent pyrolysis treatment led to the creation of ordered iron oxide stripes from the prepared polymer template. This facile, simple and robust deposition technique based on controlled evaporative self-assembly, combined with following pyrolysis, opens up a new avenue for preparing two-dimensional and well-ordered metal oxide patterns in a controllable and cost-effective manner.

Introduction

In last two decades, metallocene-containing polymers have attracted significant attention in material science since they have great potential applications in catalytic, optical, magnetic, and biological areas.[1-6] For example, they are ideal precursors for producing magnetoceramics whose magnetic properties can be tuned by pyrolysis temperature.[7-9] Compared to widely studied main chain metallocene-containing polymers explored by Manners and coworkers [3, 4, 6, 10, 11], side-chain metallocene-containing polymers with the metallocene unit as a pendant group have recently started to draw attention due to the facile

electrophilic substitution of metallocene, especially well-defined polymers and block copolymers synthesized with predetermined molecular weight, low polydispersity, high functionality and diverse architectures, via controlled/living radical polymerization techniques (CRP).[12-15] One of the advantages to use these metallocene-containing polymers is to prepare patterned, micron-scale metal bars, circles and lines via microcontact printing,[10] template-based synthesis combined with chemical etching,[9] and E-beam lithography[1] after pyrolysis treatment. However, these techniques mentioned above are not cost-effective and require multi steps. Thus, an extremely simple, one-step and non-lithography route to creation of intriguing, well-ordered metal or metal oxide micro structures from metallocene-containing polymers template over a large area is highly desired.

Recently, controlled self-assembly in confined geometries have demonstrated the feasibility of delicately manipulating the drying process to drive the assembly of nonvolatile materials (i.e., nanoparticles, polymers, and biological entities) into well-structured patterns with remarkably high fidelity and regularity, thus representing an extremely versatile way for one-step creation of complex large-scale and ordered structures that have numerous technological applications in microelectronics, data storage devices, and biotechnology.[16-35] By subjecting drying droplets to such a restricted geometry (e.g. a "cylinder-on-flat" geometry), the evaporation rate of solution is controlled and the temperature gradient is minimized or eliminated. Thus, the possible nature convection and Marangoni flow are suppressed, the instabilities (e.g., fingering instability) can be readily harnessed. Due to the imposed geometrical constraint, the evaporation is restricted to occur only at the capillary edge. As a result, controlled, repetitive pinning and depinning of the three-phase contact line yields a lateral surface morphology naturally and spontaneously which consists of hundreds

of highly ordered periodical polymer deposits. [35, 36] Notably, this procedure was remarkably controllable, high-yielding, and easy to implement, thus opening up a new route for fabricating highly ordered organic and inorganic structures with potential in optoelectronics, photonics, and biosensor applications.

Herein, we present a simple and straightforward method to achieve ordered iron oxide patterns over large areas by combining controlled evaporative self-assembly and subsequent pyrolysis process. Well-ordered ferrocene-containing polymer stripes with remarkable regularity were spontaneously formed on Si substrate via evaporation induced self-assembly in a confined geometry consisting of a cylindrical lens on flat Si substrate (See Figure 35a). Subsequent pyrolysis of patterned polymer stripes led to the creation of ordered iron oxide stripes. Field-emission scanning electron microscope (FE-SEM), X-ray diffraction (XRD), X-ray photoelectron spectroscopy (XPS) and Energy-dispersive X-ray spectroscopy (EDX) were used to prove the formation of iron oxide particles after pyrolysis process. Here we introduce for the first time the micro scale patterning of the iron oxide stripes with unprecedented regularity via controlled evaporative self-assembly combined with following pyrolysis treatment of ferrocene-containing polymers.

Experimental Section.

Synthesis and Characterization of PAMEFC: This new side-chain ferrocene-containing polymer (poly 2-(metharcryloyloxy) ethyl ferrocenecarboxylate (PAMEFC)) was prepared via atom transfer radical polymerization. The detailed synthesizing procedures can be found in our previous work.[15] The Mn and PDI of homopolymer PMAEFC is 21700

(obtained from ^{1}H NMR) and 1.25, respectively. Chemical structure of PAMEFC is shown in Figure 35c.

Evaporative Self-Assembly of the PAMEFC toluene Solution in a Cylinder-on-Si Geometry. PAMEFc was dissolved in toluene at a concentration of 0.4mgmL^{-1} and purified with 200 nm polytetrafluoroethylene (PTFE) filters. The cylinder lens (L=9.5mm, H=3.2 mm, W=11.0mm, Figure 35a) and silicon substrate were used as the upper and lower surface, respectively, to construct a confined geometry. The silicon substrates were cleaned with a mixture of sulfuric acid and Nochromix, then rinsed extensively with deionized (DI) water and blow-dried with N_2. The cylinder-on-Si geometry was placed in a sealed chamber to minimize possible air convection and maintain constant temperature during the evaporation process.

Characterization. The surface structures produced on Si substrate were characterized by optical microscopy (Olympus BX51 in the reflection mode) and atomic force microscopy (Dimension 3100 scanning force microscope in the tapping mode (Digital Instruments)). Vista probes (T190) with spring constants 48Nm^{-1} were used as scanning probes. X-ray photoelectron spectroscopy (XPS; PHI 5500) measurements were performed with Al standard x-ray source (1486.6 eV). The samples were attached to the holder using double stick tape to isolate the charging effects. WAXD profiles were obtained by using a Bruker D8 Discover Reflector with X-ray generation power of 40kV tube voltage and 40mA tube current. The diffraction was recorded at a θ-2θ symmetry scanning mode with scan angle from $2\theta=30^{o}$-66^{o}. Patterns of nanoparticles were observed by a field-emission scanning electron microscope (FE-SEM; FEI Quanta 250) operating at 20kv in High Vacuum.

Results and Discussion

A new synthesized side-chain ferrocene-containing polymer, poly 2-(metharcryloyloxy) ethyl ferrocenecarboxylate (PAMEFC, see Experimental Section) was employed as the nonvolatile solute. The PAMEFC toluene solution (volume: V=30 mL) with the concentration of 0.4 mg/mL was then loaded and trapped in a restricted geometry composed of a cylindrical lens sitting on a Si substrate (i.e. cylinder-on-flat geometry; Figure. 1a) (see Experimental Section), thus yielding a capillary-held solution, in which the evaporation of toluene was restricted at the constrained capillary edge. The evaporative loss of toluene at the capillary edge triggered the pinning of the three-phase contact line (i.e., ‘‘stick’’) by transporting nonvolatile PAMEFC to the capillary edge, thus forming an outmost PAMEFC stripe.[21] During the deposition of PAMEFC, the initial contact angle of the meniscus gradually decreased to a critical value due to continuing evaporative loss of toluene, at which the depinning force (i.e., capillary force) became larger than the pinning force (i.e., friction force), causing the contact line to jerk toward the cylinder/Si contact center (i.e., “slip”) and get arrested at a new position, thereby leaving behind a stripe locally. Consecutive pinning and depinning of the contact line of the evaporating PAMEFC toluene drop assembled them into hundreds of periodical stripes in an elliptical arrangement globally (Figure 35b), guided by the shape of upper cylindrical lens (see Experimental Section).[21] It is noteworthy that the confined cylinder-on-flat geometry provides a unique environment (i.e., a bound solution) for controlling the flow within an evaporating droplet, which in turn regulates the intriguing structure formation. As opposed to the irregular concentric rings formed due to stochastic ‘‘stick-slip’’ cycles of the contact line when a droplet evaporates from a single surface (i.e., an unbound solution),[37-40] the formation of PAMEFC patterns with unprecedented regularity

suggests that the use of the cylinder-on-Si geometry rendered control over the evaporation rate, and is effective in improving the stability against the convection. It is also of interest to note that the well-ordered PAMEFC stripes observed here were highly reproducible.

These periodical patterns were characterized by optical microscopy (OM) first. Figure 35d shows typical optical micrographs of PAMEFC stripes formed after the evaporation was complete. It is clearly observed that highly ordered, microscopic PAMEFC stripes locally formed in the cylinder-on-Si geometry, where X_n (n ranging from 1 to 3) indicates the position away from the cylinder/Si contact center (see Figure 35d). It is noteworthy that only a small zone of the entire pattern is shown in Figure 35d. The entire pattern was formed over 1x1cm^2 surface areas. Compared to the concentric rings formed by the evaporative self-assembly in a sphere-on-flat geometry,[17, 19, 22] the use of upper cylinder lens yielded straight stripe-like patterns over large areas, as shown in the insert OM image in Figure 35d, which may potentially be used into complex microelectronic, optical and sensing devices.

AFM measurement of the PAMEFC patterns deposited on the Si substrate revealed their dimensions and spacings, respectively, as shown in Figure 36. Locally, they appeared as parallel lines. The distance between adjacent stripes, $\lambda_{c\text{-}c}$, the height of stripe, h, and the width of stripe, w, progressively decreased as the contact line of evaporating solution approached the cylinder/Si contact center, from $\lambda_{c\text{-}c}$=4.82μm, w = 2.78μm, and h = 32.6nm at X_1 = 3000μm (Figure 3a), to $\lambda_{c\text{-}c}$=4.12μm, w =2.48μm and h =25.8nm at X_2 = 2700μm (Figure 3c), to $\lambda_{c\text{-}c}$=3.62μm, w =2.32μm and h =23.8nm, at X_2 = 2400μm (Figure 3d). The formation of gradient stripes was a direct consequence of the competition between the nonlinear capillary force, due to the curvature effect of the cylinder, and the linear pinning force.[21] It is noteworthy that, compared to other polymer patterns formed before,[19, 26, 30, 31, 33] small

dimensions and spacings between adjacent stripes were achieved, due to the small molecular weight of PAMEFC. Close examination of PAMFEC stripes revealed that several “holes” formed at one side of stripes during the deposition process, due to the “figuring instability” formed by evaporative self-assembly (Figure 36, insert images).

In order to get iron oxide patterns via the prepared polymer template, the PAMEFC samples were further pyrolyzed at 1000^{o}C in a pyrolysis furnace for two hours (air environment). During pyrolysis process, the Fe atoms “released” from the ferrocene moieties and migrate together to form iron oxide crystals, in the air environment. [10] Shown in Figure 3a is the optical images of PAMEFC patterns after pyrolysis. It is noteworthy that the location and the order of the pattern will be preserved as the original pattern of the starter polymer stripes. From the SEM image, it is clearly observed that the stripes were composited of discreted nanoparticles with the diameter of about 30nm (See Figure 3b). As far as we know, this is the first time to fabricate the well-ordered metal iron patterns via the controlled evaporative self-assembly, using metallocene-containing polymers as the template. Since the pyrolysis leading the iron oxide stripes would not change the dimension and spacing of the whole patterns, this simple and facile process has promises applications in magnetic data storage and microelectrics.

Energy-dispersive X-ray spectroscopy (EDX) was used to estimate the chemical composition of the pyrolyzed samples (See Supporting Information). The Fe, Si and O elements are understandably from the polymer template, the substrate and air environment during the pyrolysis, respectively. The Ir element detected by the EDX was due to the Ir sputtering before SEM observation. The amounts of the Fe and O elements detected on the stripes are much higher than those detected between the stripes, thus implying the Fe and O

element are mainly located on the stripes (See Supporting Information). To future demonstrate the successful preparation of iron oxide stripes, information regarding the surface composition of the pyrolyzed stripes was obtained via X-ray photoelectron spectroscopy (XPS) and compared to data obtained from an untreated sample of PAMEFC, as shown in Figure 38a. The peak characteristic of ferrocene moieties (E_B=708eV) was observed in the untreated sample. The absence of this peak after the pyrolysis indicated that the Fe atoms are released from polymeric ferrocene moieties and migrate to form Fe_2O_3 nanoparticles (E_B=711eV and 725eV).[10] The small amount of Fe on the untreated sample may be from the synthesis and Fe_2O_3 may be introduced by the moisture absorbed by the polymer samples prior to pyrolysis.[5] The absence of the α-Fe peaks on the pyrolyzed sample is due to the air environment during the pyrolysis process. Since α- and γ-Fe_2O_3 species possess the same binding energy, [5] it is difficult to distinguish whether the iron oxide in the samples is in the α- or γ-Fe_2O_3 phase on the basis of the XPS data alone. As a result, the pyrolyzed sample was future examined by X-ray diffraction (XRD) to determine the iron oxide phase (Figure 38b). The XRD showed three sharp peaks at $2\theta=33^o$, 62^o and 67^o, respectively, indicating the presence of crystalline hematite (α- Fe_2O_3) in the samples.[10]

Conclusions

In summary, we have demonstrated a simple, robust means to create highly regular iron oxide stripes by combine controlled evaporative self-assembly of capillary-held PAMEFC toluene solution in the cylinder-on-Si geometry and following pyrolysis treatment, in an easily controllable and cost-effective manner. By allowing a drop of PAMEFC to evaporate between a confined geometry, which provides unique environment for controlling the flow

within the droplet, intriguing and highly ordered structures on a large scale can be produced. The prepared polymer template can easily converted to inorganic patterns after the pyrolysis with unchanged spacing the dimension as original polymer patterns. These self-organized patterns over large areas offer a tremendous potential for applications in magnetic data storage, optics and microelectrics. We envision that by varying the pyrolysis environment (nitrogen, argon and etc.) and the pyrolysis temperature, different state of metal or metal oxide patterns can be achieved.

Figures

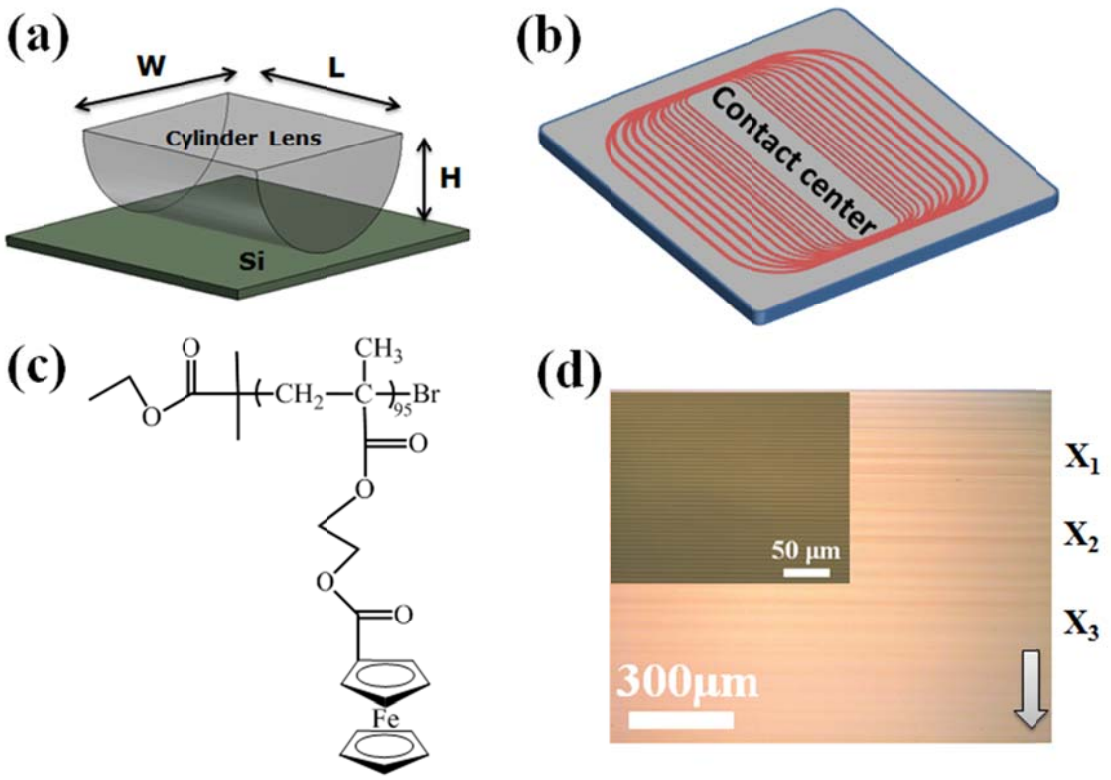

Figure 35. (a) 3D view of "cylinder-on-flat" geometry. H, L and W are the height, length and width of cylinder lens, respectively. (b) Schematic representation of the formation of gradient PAMEFC stripes via confined evaporative self-assembly. (c) The chemical structure of a new synthesized side-chain ferrocene-containing polymer PAMEFC. (d) Optical micrograph images of PAMEFC stripes formed by evaporative self-assembly in a cylinder-on-flat geometry. The white arrows mark the movement of the solution front toward the cylinder/Si contact center. X_n (n=1, 2, 3) indicates the position toward the contact center.

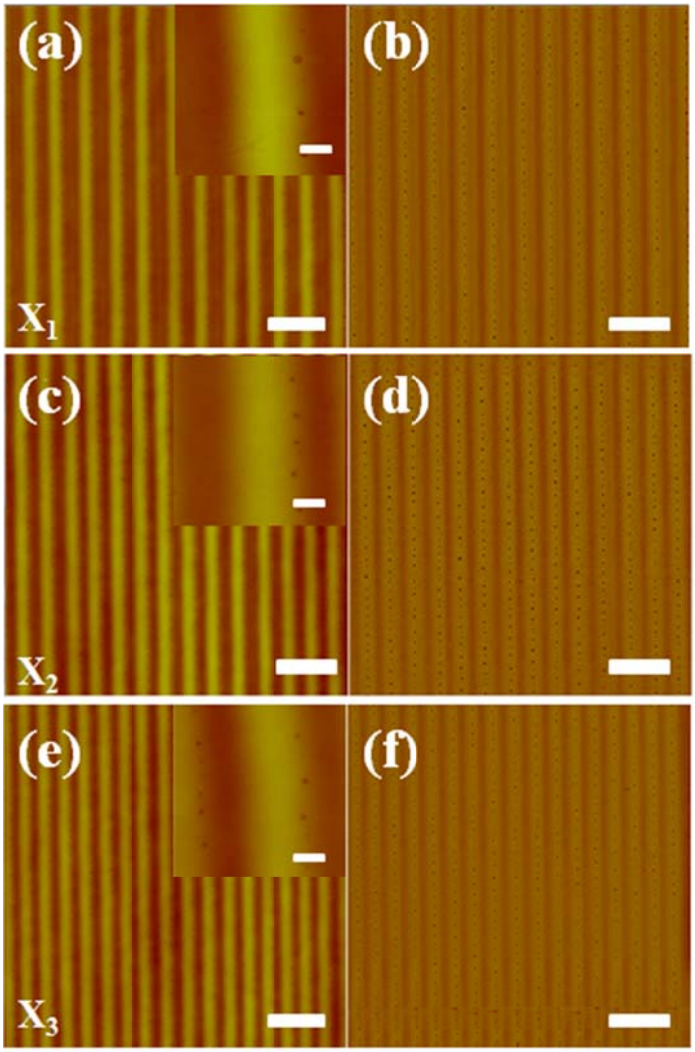

Figure 36. Representative AFM height (a, c d) and corresponding phase (b, d, f) images at different locations. (a, b) at the outermost region X_1, (c, d) at the intermediate region X_2, (e, f) at the innermost region X_3. The distance between adjacent stripes, the height of stripes, and the width of stripes gradually decreased at these three regions. The scale bar and Z range is 10um and 200nm for (a), (c), (e) AFM images, and 1um and 150nm for insert images, respectively.

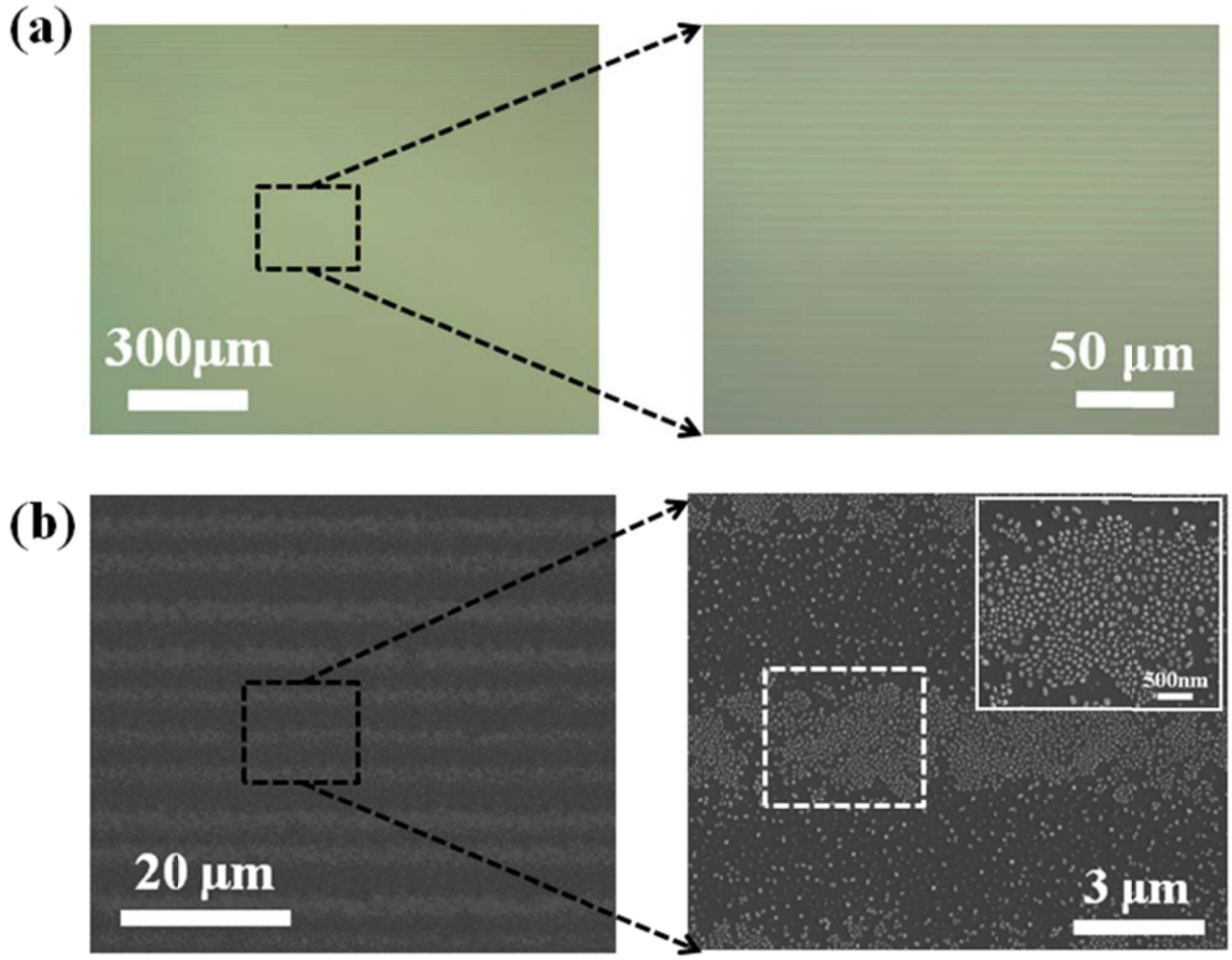

Figure 37. (a) Optical micrograph images of PAMEFC stripes patterns after pyrolysis. It is noteworthy that the location and the order of the pattern will be preserved as the original pattern of the starter polymer stripes. (b) SEM images of pyrolyzed PAMEFC stripes. From the insert image it is clearly observed that the stripes were composited of discreted nanoparticles

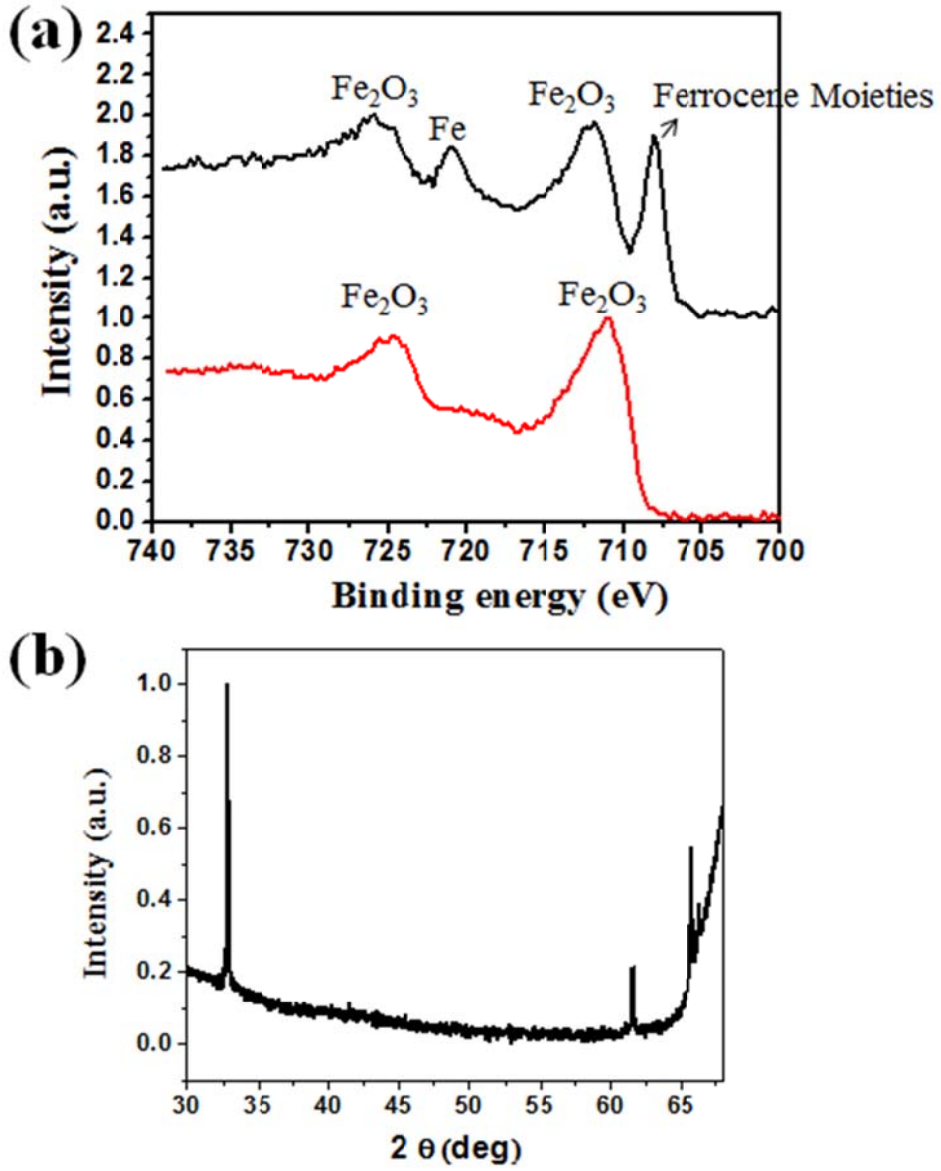

Figure 38. (a) XPS spectra for PAMEFC stripes on top of Si substrate before (top black line) and after (bottom red line) pyrolysis. (b) XRD pattern of PAMEFC stripes after pyrolysis. These peaks indicate the formation of crystalline hematite (α- Fe_2O_3) in the samples.

Supporting Information

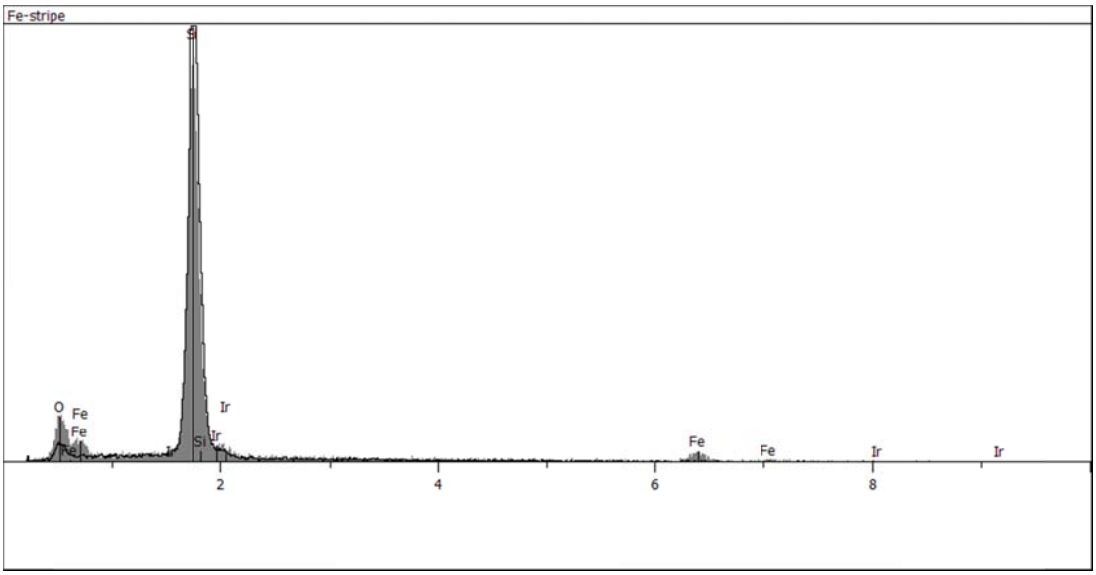

Table1: On PAMEFC stripe

Elem	Line	At.%	Wt.%
O	Ka	24.839	14.175
Si	Ka	70.346	70.469
Fe	La	3.631	7.232
Ir	Ma	1.185	8.125
Total		100.000	100.000

Table2: Silica between stripes

Elem	Line	At.%	Wt.%
O	Ka	10.499	5.859
Si	Ka	87.961	86.166
Fe	La	0.495	0.964
Ir	Ma	1.046	7.011
Total		100.000	100.000

Figure S1. Energy dispersive X-ray spectroscopy (EDS) analysis of pyrolyzed samples.

Table 1 and Table 2 give the Atomic composition of pyrolyzed samples estimated by EDX

analyses. The amounts of the Fe and O elements detected on the stripes are much higher than those detected between the stripes, thus implying the Fe and O element are mainly located on the stripes.

References

1. Clendenning, S. B.; Aouba, S.; Rayat, M. S.; Grozea, D.; Sorge, J. B.; Brodersen, P. M.; Sodhi, R. N. S.; Lu, Z. H.; Yip, C. M.; Freeman, M. R.; Ruda, H. E.; Manners, I., *Adv. Mater.* **2004,** *16* (3), 215-219.
2. Korczagin, I.; Lammertink, R.; Hempenius, M.; Golze, S.; Vancso, G., Surface Nano- and Microstructuring with Organometallic Polymers Ordered Polymeric Nanostructures at Surfaces. Vancso, G., Ed. Springer Berlin / Heidelberg: 2006; Vol. 200, pp 91-117.
3. MacLachlan, M. J.; Ginzburg, M.; Coombs, N.; Coyle, T. W.; Raju, N. P.; Greedan, J. E.; Ozin, G. A.; Manners, I., *Science* **2000,** *287* (5457), 1460-1463.
4. Raez, J.; Manners, I.; Winnik, M. A., *J. Am. Chem. Soc.* **2002,** *124* (35), 10381-10395.
5. Sun, Q.; Lam, J. W. Y.; Xu, K.; Xu, H.; Cha, J. A. K.; Wong, P. C. L.; Wen, G.; Zhang, X.; Jing, X.; Wang, F.; Tang, B. Z., *Chem. Mater.* **2000,** *12* (9), 2617-2624.
6. Whittell, G. R.; Manners, I., *Adv. Mater.* **2007,** *19* (21), 3439-3468.
7. Kulbaba, K.; Manners, I., *Macromol. Rapid. Comm.* **2001,** *22* (10), 711-724.
8. Kulbaba, K.; Resendes, R.; Cheng, A.; Bartole, A.; Safa-Sefat, A.; Coombs, N.; Stöver, H. D. H.; Greedan, J. E.; Ozin, G. A.; Manners, I., *Adv. Mater.* **2001,** *13* (10), 732-736.
9. Ginzburg-Margau, M.; Fournier-Bidoz, S.; Coombs, N.; Ozin, G. A.; Manners, I., *Chem. Commun.* **2002,** (24).
10. Ginzburg, M.; MacLachlan, M. J.; Yang, S. M.; Coombs, N.; Coyle, T. W.; Raju, N. P.; Greedan, J. E.; Herber, R. H.; Ozin, G. A.; Manners, I., *J. Am. Chem. Soc.* **2002,** *124* (11), 2625-2639.
11. Nguyen, P.; Gómez-Elipe, P.; Manners, I., *Chem. Rev.* **1999,** *99* (6), 1515-1548.
12. Watson, K. J.; Zhu, J.; Nguyen, S. T.; Mirkin, C. A., *J. Am. Chem. Soc.* **1998,** *121* (2), 462-463.
13. Albagli, D.; Bazan, G.; Wrighton, M. S.; Schrock, R. R., *J. Am. Chem. Soc.* **1992,** *114* (11), 4150-4158.
14. Ren, L.; Hardy, C. G.; Tang, C., *J. Am. Chem. Soc.* **2010,** *132* (26), 8874-8875.
15. Hardy, C. G.; Ren, L.; Tamboue, T. C.; Tang, C., *Journal of Polymer Science Part A: Polymer Chemistry* **2011,** *49* (6), 1409-1420.
16. Byun, M.; Wang, J.; Lin, Z., *Acta Phys. -Chim. Sin.* **2009,** *25*, 1249.
17. Hong, S. W.; Jeong, W.; Ko, H.; Kessler, M. R.; Tsukruk, V.; Lin, Z. Q., *Adv. Funct. Mater.* **2008,** *18*, 2114
18. Hong, S. W.; Xia, J.; Lin, Z. Q., *Adv. Mater.* **2007,** *19*, 1413.
19. Hong, S. W.; Byun, M.; Lin, Z. Q., *Angew. Chem., Int. Ed.* **2009,** *48*, 512.
20. Hong, S. W.; Wang, J.; Lin, Z. Q., *Angew. Chem., Int. Ed.* **2009,** *48*, 8356.
21. Xu, J.; Xia, J.; Lin, Z. Q., *Angew. Chem., Int. Ed.* **2007,** *46*, 1860.
22. Hong, S. W.; Xu, J.; Lin, Z. Q., *Nano Lett.* **2006,** *6* (12), 2949-2954.
23. Hong, S. W.; Xu, J.; Xia, J.; Lin, Z. Q.; Qiu, F.; Yang, Y. L., *Chem. Mater.* **2005,** *17*, 6223.
24. Byun, M.; Wang, J.; Lin, Z., *J. Phys.: Cond. Matt.* **2009,** *21*, 264014.
25. Han, W.; Byun, M.; Lin, Z., *J. Mater. Chem.* **2011,** *21* (42), 16968-16972.
26. Han, W.; Byun, M.; Zhao, L.; Rzayev, J.; Lin, Z., *J. Mater. Chem.* **2011,** *21* (37), 14248-14253.

27. Byun, M.; Hong, S. W.; Zhu, L.; Lin, Z. Q., *Langmuir.* **2008,** *24*, 3525.
28. Stafford, C. M.; Vogt, B. D.; Harrison, C.; Julthongpiput, D.; Huang, R., *Macromolecules* **2006,** *39* (15), 5095-5099.
29. Byun, M.; Hong, S. W.; Qiu, F.; Zou, Q.; Lin, Z., *Macromolecules* **2008,** *41*, 9312.
30. Hong, S. W.; Xia, J.; Byun, M.; Zou, Q.; Lin, Z. Q., *Macromolecules* **2007,** *40*, 2831.
31. Byun, M.; Bowden, N. B.; Lin, Z. Q., *Nano Lett.* **2010,** *10*, 3111.
32. Hong, S. W.; Xu, J.; Lin, Z. Q., *Nano Lett.* **2006,** *6*, 2949.
33. Byun, M.; Han, W.; Qiu, F.; Bowden, N. B.; Lin, Z. Q., *Small* **2010,** *6*, 2250.
34. Byun, M.; Laskowski, R. L.; He, M.; Qiu, F.; Jeffries-EL, M.; Lin, Z. Q., *Soft Matter* **2009,** *5*, 1583.
35. Han, W.; Lin, Z., *Angew. Chem. Int. Ed.* **2012,** *51* (7), 1534-1546.
36. Lin, Z., *Journal of Polymer Science Part B: Polymer Physics* **2010,** *48* (24), 2552-2557.
37. Adachi, E.; Dimitrov, A. S.; Nagayama, K., *Langmuir.* **1995,** *11* (4), 1057-1060.
38. Deegan, R. D.; Bakajin, O.; Dupont, T. F.; Huber, G.; Nagel, S. R.; Witten, T. A., *Nature* **1997,** *389* (6653), 827-829.
39. Deegan, R. D., *Phys. Rev. E* **2000,** *61* (1), 475-485.
40. Deegan, R. D.; Bakajin, O.; Dupont, T. F.; Huber, G.; Nagel, S. R.; Witten, T. A., *Phys. Rev. E* **2000,** *62* (1), 756-765.

CHAPTER 7. MAGNETIC FIELD ASSISTED SELF-ASSEMBLY OF MAGNETIC NANOPARTICLES

Modified from a manuscript to be submitted

Wei Han and Zhiqun Lin*

Abstract

By combining magnetic-filed induced self-assembly with controlled evaporative self-assembly (CESA), we present a simple and cost-effective route to organize nonvolatile materials into ordered asymmetry microscopic structures over large surface areas. When a gradient magnetic field is applied next to the "cylinder-on-flat" geometry, the asymmetry pattern with an increase in $\lambda_{C\text{-}C}$, width and height on one side and a decrease of them on the other side can be observed, thus potentially achieving improved ordering and orientation of micro- and nanostructures. This technique is remarkably controllable and easy to implement, opening up a new route for fabricating highly structured functional materials and devices in a fast, robust, and cost-effective manner.

Introduction

Assemblies and controlled positioning of metallic, semiconducting, and magnetic nanoscale materials into well-ordered functional structures offer new opportunities for miniaturized electronic, optoelectronic, and magnetic devices. Their collective properties depend on particle size, shape, and spatial arrangement of the nanomaterials. The latter can be produced by employing a variety of self-assembly techniques, including self-directed self-assembly, magnetic field induced assembly, and electrostatic interaction-induced assembly.

Recently, spontaneous self-assembly of nanoscale materials to form intriguing, complex yet well-ordered structures via the evaporation of a sessile droplet containing nonvolatile solutes provides a simple means to fabricate functional materials.[1-7] However, flow instabilities within the evaporating droplet often result in irregular dissipative structures (e.g., fingering instabilities, convection patters, etc.).[4, 8, 9] To date, a few elegant methods have emerged to precisely control the evaporation process to produce highly ordered structures that are technologically relevant. Among them, controlled evaporative self-assembly (*CESA*) of a droplet constrained in restricted geometries (e.g., cylinder-on-flat) renders the creation of intriguing structures with high fidelity and regularity.[10-27]

Magnetic nanoparticles are promising building blocks for high-performances nanodevices for applications such as data storage,[28] ferrofluid technology,[29] and energy storage. Achieving this enormous promise, however, requires controlled fabrication of specific structures using nanoparticles as elementary. The application of an additional external field (e.g., magnetic, electric, and mechanical shear) in conjunction with the solvent evaporative field may be an effective strategy to promote the CESA of polymers and colloids. The external electric or magnetic field could make the deposition process more rapid, and thus reducing the number of defects in the formed structures.

Here, by combining magnetic-filed induced self-assembly with controlled evaporative self-assembly (CESA), we present a simple and cost-effective route to organize nonvolatile materials into ordered asymmetry microscopic structures over large surface areas. When a gradient magnetic field is applied next to the “cylinder-on-flat” geometry, the asymmetry pattern with an increase in $\lambda_{C\text{-}C}$, width and height on one side and a decrease of them on the

other side can be observed, thus potentially achieving improved ordering and orientation of micro- and nanostructures.

Experimental Section.

Synthesis of monodispersed Fe_3O_4 magnetic nanoparticles. Monodispersed Fe_3O_4 magnetic nanoparticles with diameter of 10nm were synthesized based on our 21 arms β-CD template, according to our previous report. These prepared Fe_3O_4 magnetic nanoparticles were dissolved in toluene for the future use.

Magnetic-filed Assisted Evaporative Self-Assembly of the PMMA toluene Solution in a Cylinder-on-Si Geometry. The cylinder lens (L=9.5mm, H=4.0mm, W=11.0mm, Figure 39b) and silicon substrate were used as the upper and lower surface, respectively, to construct a confined geometry. The silicon substrates were cleaned with a mixture of sulfuric acid and Nochromix, then rinsed extensively with deionized (DI) water and blow-dried with N_2. The magnet purchased from *K&J Magnetics* was sitting at one side of the CSEA setup (Figure 39). The distance between the magnet and gradient intensity of magnetic field was carefully measured and recorded. The cylinder-on-Si geometry was placed in a sealed chamber to minimize possible air convection and maintain constant temperature during the evaporation process.

Characterization. The surface structures produced on Si substrate were characterized by optical microscopy (Olympus BX51 in the reflection mode) and atomic force microscopy (ICON, Bruker). Vista probes (T190) with spring constants $48Nm^{-1}$ were used as scanning probes.

Results and Discussion

Monodispersed Fe_3O_4 magnetic nanoparticles with diameter of 10nm were synthesized based on our 21 arms β-CD template, according to our previous report. First to study the evaporative self-assembly of Fe_3O_4 nanoparticles in the cylinder-on-Si geometry, without the external magnetic field, the Fe_3O_4 nanoparticle toluene solution was loaded, and bridged the cylinder and Si substrate, yielding a capillary-held solution (Figure 39). During the evaporation, the evaporation of toluene only occurred at the constrained capillary edge. As toluene evaporated, Fe_3O_4 nanoparticles were transported from the solution to the capillary edge, conglomerated, and pinned the contact line, forming parallel deposits. During the deposition of nanoparticles, the initial contact angle gradually decreased to a critical contact angle, at which the capillary force becomes larger than the pinning force, causing the contact line to jump to a new position, where it was arrested again and a new ring was thus produced. The use of axially symmetric cylinder-on-Si geometry was responsible for consecutive pinning (i.e., 'stick') and depinning (i.e., 'slip') cycles of the contact line in a controllable manner, leaving behind hundreds of concentric 'coffee rings' of Fe_3O_4 nanoparticles (Supporting Information). The stripe arrays exhibited gradient features, representing the decrease in center-to-center distance between neighboring rings, λ and the ring width, w, as the liquid capillary edge approached the cylinder/Si contact center. This is because of the imbalance between the nonlinear capillary force, due to the curvature effect of the cylinder, and the linear pinning force.

Subsequently, when combining magnetic-filed induced self-assembly with controlled evaporative self-assembly (CESA) by putting a magnet at one side of substrate, thus providing gradient magnetic field, from the left to the right, intriguing asymmetry pattern

was yielded, as shown in Figure 39 and Figure 40. From the representative optical microscope images at left and right side, both from outermost to innermost, respectively, asymmetry pattern with different $\lambda_{C\text{-}C}$, width and height of stripes were clear observed.

AFM measurements were performed to examine the detailed surface morphologies of the Fe_3O_4 arrays. Two-dimensional AFM height images obtained from *Left side (close to the magnet)* and *Right side (far away from the magnet)* are shown in figures 3, respectively, with the parallel locally stripe looking. For the *Left side*, as the solution front moved toward the cylinder/Si contact center, λ, *w and h* progressively decreased from λ = 22.3μm, *w* = 5.8μm and h= 208.2nm at *X*1 = 4600μm to λ = 20.2μm, *w* = 5.6μm and h= 207.8nm at *X*2 = 4200μm to λ = 18.8μm, *w* = 5.6μm and h= 207.3nm at *X*3 = 3800μm to λ = 17.1μm, *w* = 5.2μm and h= 206.9nm at *X*4 = 3400μm. With increased proximity to the cylinder/Si contact center, stripes with smaller *w* formed, indicating a shorter pinning time of Fe_3O_4 nanoparticles at the three-phase contact line. A smaller *w* also implies a lesser volume loss of solvent during pinning. As a result, this led to a shorter pull away of the contact line to a new position, thereby yielding a smaller λ. However, for the *Right side* pattern, as the solution front moved toward the cylinder/Si contact center, λ, *w and h* progressively decreased from λ = 14.4μm, *w* = 3.2μm and h= 132.6nm at *X*1 = 4600μm to λ = 13.7μm, *w* = 2.8μm and h= 132.2nm at *X*2 = 4200μm to λ = 13.1μm, *w* = 2.7μm and h= 130.4nm at *X*3 = 3800μm to λ = 10.2μm, *w* = 2.5μm and h= 128.2nm at *X*4 = 3400μm, which showed quite small dimension compare to the left side.

Compare all the dimensional values obtained from AFM, with and without magnetic field assisted, as shown in Figure 4, we found at the area close to the magnet, the width, height and λ are the largest at each location, and the smallest valves were observed at the area

far away from the magnet. It has been demonstrated the formation of these parallel stripes were due to the competition between the capillary force (depinning force) and the frication force (pinning force), thus inducing repeated “stick-slip” motion of three-phase contact line during the evaporation process. As shown in Figure 4a, at the left side, the employing of the magnet induce the magnetic force which is helping pin the contact line, thus making the deposition time longer, which means, the loss of toluene during the deposition is larger than without external field. As a result, the longer deposition time yields larger amount of particles depositing at the contact line, with larger height and width. The larger solvent loss makes the contact line jump longer to the new position and arrests again to form the new stripe, thus achieving larger distance between the stripes, compared to the pattern formed without magnetic field. However, on the other side, the magnetic force helps depinning the contact line, thus making the shorter pinning time and less loss of toluene during the deposition, finally achieving the small height, width and λ of the pattern at the same X location.

Conclusions

By combining magnetic-filed induced self-assembly with controlled evaporative self-assembly (CESA), we present a simple and cost-effective route to organize nonvolatile materials into ordered asymmetry microscopic structures over large surface areas. When a gradient magnetic field is applied next to the “cylinder-on-flat” geometry, the asymmetry pattern with an increase in $\lambda_{C\text{-}C}$, width and height on one side and a decrease of them on the other side can be observed, thus potentially achieving improved ordering and orientation of micro- and nanostructures. This technique is remarkably controllable and easy to implement,

opening up a new route for fabricating highly structured functional materials and devices in a fast, robust, and cost-effective manner.

Figures

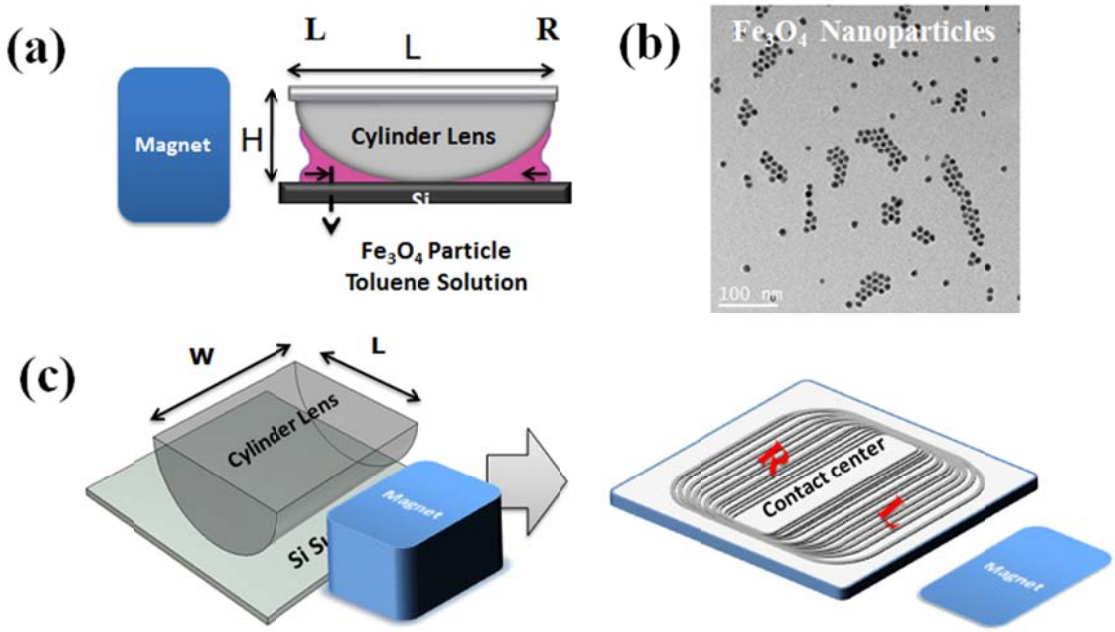

Figure 39. (a) Schematic side view of a capillary-held toluene solution containing Fe_3O_4 nanoparticles placed in a cylinder lens, assisted by the external filed. (b) TEM images of Fe_3O_4 nanoparticles. The diameter of Fe_3O_4 nanoparticles is about 10nm. (c) Schematic three-dimensional illustration of the setup.

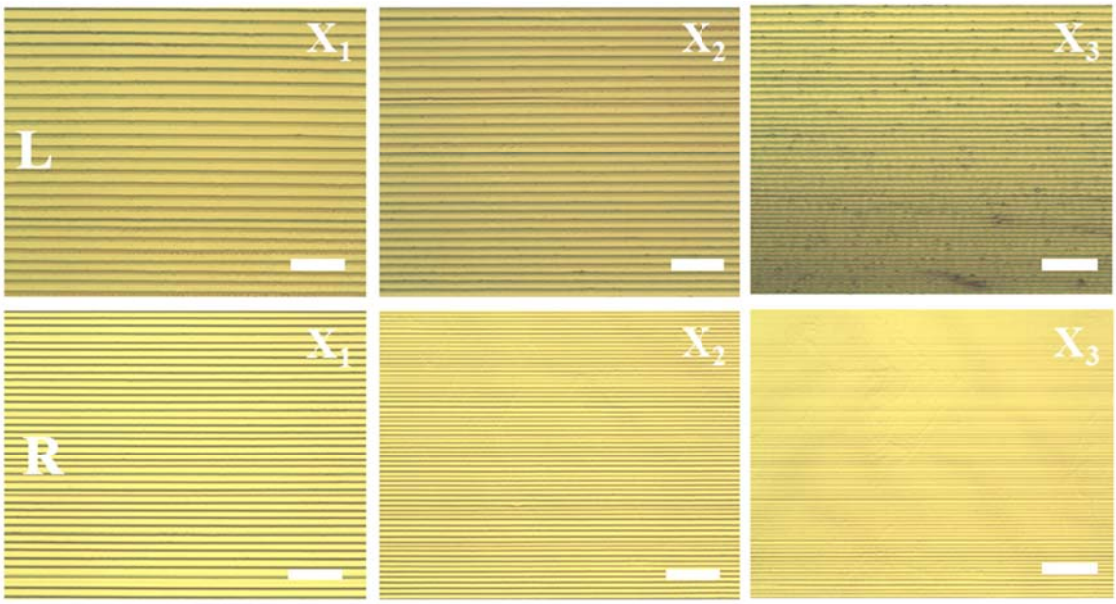

Figure 40. Representative optical microscope images of well-ordered Fe_3O_4 nanoparticle stripes in different regions, at the left side and right side, respectively.

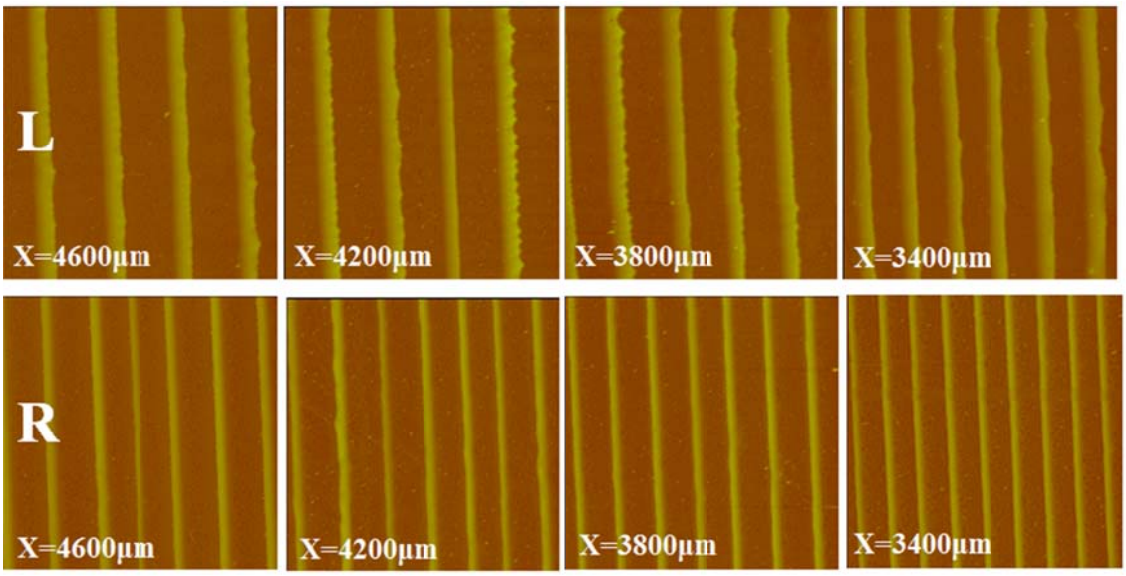

Figure 41. Representative AFM height images of well-ordered Fe_3O_4 nanoparticle stripes in different regions, at the left side and right side, respectively.

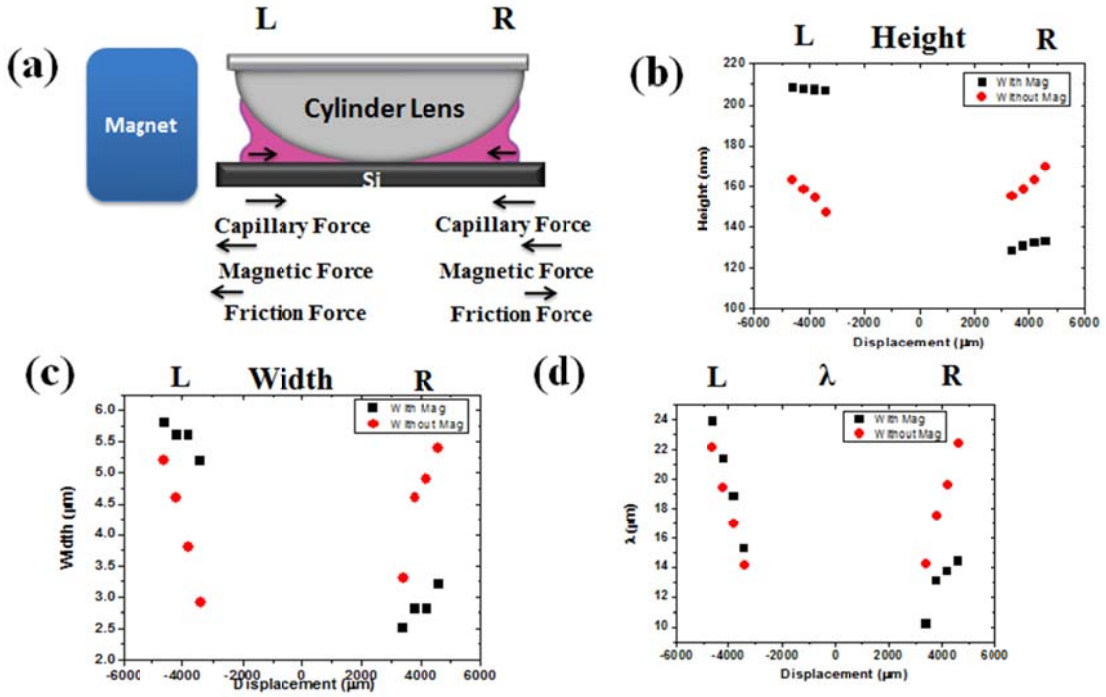

Figure 42. (a) Schematic presentation of the dominative force during the magnetic assisted controlled evaporative self-assembly. (b)-(d) Diagram of the comparisons of the height, width and distances between the stripes with different location and with and without magnetic field, respectively.

Supporting Information

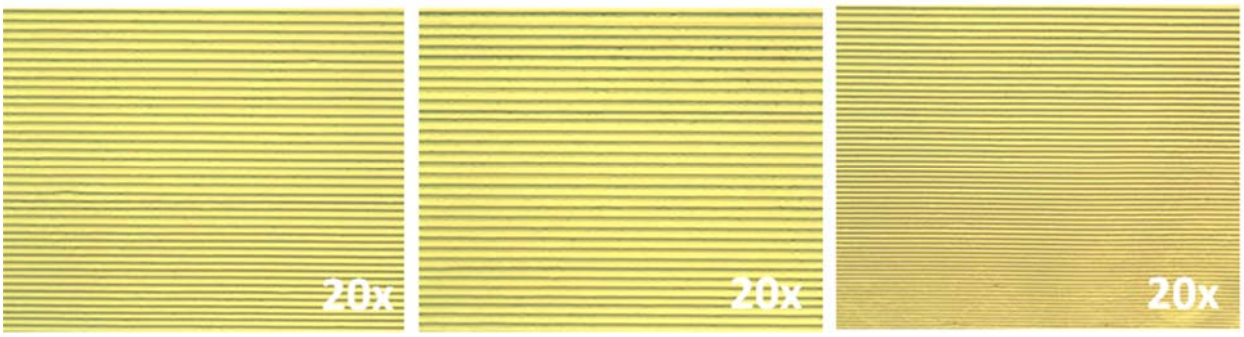

Figure S1. Representative optical microscope images of well-ordered Fe_3O_4 nanoparticle stripes in different regions without external magnetic field.

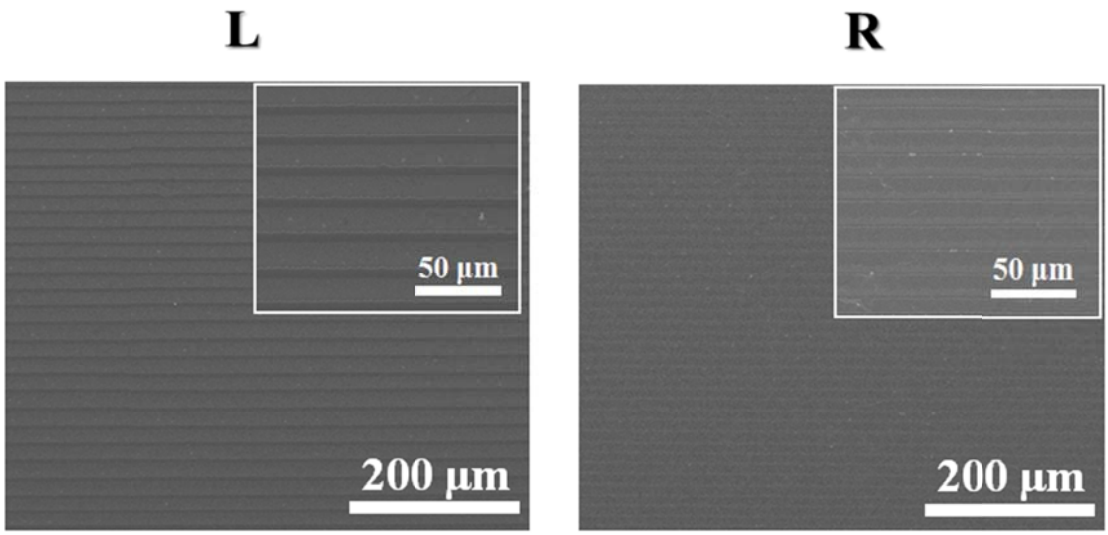

Figure S2. Representative SEM images of well-ordered Fe_3O_4 nanoparticle stripes at the left side and right side, respectively.

References

1. Bigioni, T. P.; Lin, X.-M.; Nguyen, T. T.; Corwin, E. I.; Witten, T. A.; Jaeger, H. M., *Nat Mater* **2006,** *5* (4), 265-270.
2. Martin, C. P.; Blunt, M. O.; Pauliac-Vaujour, E.; Stannard, A.; Moriarty, P.; Vancea, I.; Thiele, U., *Phys. Rev. Lett.* **2007,** *99* (11), 116103.
3. Khanal, B.; Zubarev, E., *Angewandte Chemie* **2007,** *119* (13), 2245-2248.
4. Rabani, E.; Reichman, D. R.; Geissler, P. L.; Brus, L. E., *Nature* **2003,** *426* (6964), 271-274.
5. Mitov, Z.; Kumacheva, E., *Phys. Rev. Lett.* **1998,** *81* (16), 3427.
6. Hu, H.; Larson, R. G., *Langmuir.* **2005,** *21* (9), 3963-3971.
7. Prevo, B. G.; Velev, O. D., *Langmuir.* **2004,** *20* (6), 2099-2107.
8. Stafford, C. M.; Vogt, B. D.; Harrison, C.; Julthongpiput, D.; Huang, R., *Macromolecules* **2006,** *39* (15), 5095-5099.
9. Pauliac-Vaujour, E.; Stannard, A.; Martin, C. P.; Blunt, M. O.; Notingher, I.; Moriarty, P. J.; Vancea, I.; Thiele, U., *Phys. Rev. Lett.* **2008,** *100* (17), 176102.
10. Xu, J.; Xia, J.; Hong, S. W.; Lin, Z. Q.; Qiu, F.; Yang, Y. L., *Phys. Rev. Lett.* **2006,** *96*, 066104.
11. Xu, J.; Xia, J.; Lin, Z. Q., *Angew. Chem., Int. Ed.* **2007,** *46*, 1860.
12. Hong, S. W.; Byun, M.; Lin, Z. Q., *Angew. Chem., Int. Ed.* **2009,** *48*, 512.
13. Hong, S. W.; Giri, S.; Lin, V. S. Y.; Lin, Z. Q., *Chem. Mater.* **2006,** *18*, 5164.
14. Hong, S. W.; Jeong, W.; Ko, H.; Kessler, M. R.; Tsukruk, V.; Lin, Z. Q., *Adv. Funct. Mater.* **2008,** *18*, 2114
15. Hong, S. W.; Wang, J.; Lin, Z. Q., *Angew. Chem., Int. Ed.* **2009,** *48*, 8356.
16. Hong, S. W.; Xia, J.; Byun, M.; Zou, Q.; Lin, Z. Q., *Macromolecules* **2007,** *40*, 2831.
17. Hong, S. W.; Xia, J.; Lin, Z. Q., *Adv. Mater.* **2007,** *19*, 1413.
18. Hong, S. W.; Xu, J.; Lin, Z. Q., *Nano Lett.* **2006,** *6*, 2949.
19. Hong, S. W.; Xu, J.; Xia, J.; Lin, Z. Q.; Qiu, F.; Yang, Y. L., *Chem. Mater.* **2005,** *17*, 6223.
20. Byun, M.; Bowden, N. B.; Lin, Z. Q., *Nano Lett.* **2010,** *10*, 3111.
21. Byun, M.; Han, W.; Qiu, F.; Bowden, N. B.; Lin, Z. Q., *Small* **2010,** *6*, 2250.
22. Byun, M.; Hong, S. W.; Qiu, F.; Zou, Q.; Lin, Z., *Macromolecules* **2008,** *41*, 9312.
23. Byun, M.; Hong, S. W.; Zhu, L.; Lin, Z. Q., *Langmuir.* **2008,** *24*, 3525.
24. Byun, M.; Laskowski, R. L.; He, M.; Qiu, F.; Jeffries-EL, M.; Lin, Z. Q., *Soft Matter* **2009,** *5*, 1583.
25. Byun, M.; Wang, J.; Lin, Z., *J. Phys.: Cond. Matt.* **2009,** *21*, 264014.
26. Byun, M.; Wang, J.; Lin, Z., *Acta Phys. -Chim. Sin.* **2009,** *25*, 1249.
27. Wang, J.; Xia, J.; Hong, S. W.; Qiu, F.; Yang, Y.; Lin, Z. Q., *Langmuir.* **2007,** *23*, 7411.
28. *MRS Bull.* **1990,** *15*, 12–72.
29. Rosensweig, R. E., *Ferrohydrodynamics*. Cambridge University Press: Cambridge, UK 1985.

CHAPTER 8. SWELLING-INDUCED HIERARCHICAL STRUCTURES

Modified from a manuscript to be submitted

Wei Han, Bo Li, and Zhiqun Lin*

Abstract

By combining the solvent-induced preferential swelling of Polyvinylpyrrolidone (PVP) substrate and wrinkling effect due to modulus mismatch in the upper polymethyl methacrylate (PMMA) stripes and PVP thin film, we present the formation of hierarchically well-ordered wrinkled patterns over large areas. The key difference from the prior reports on swelling-induced surface pattern formation is that we create gradient stripes via controlled evaporative self-assembly (CESA), with decreasing width and height from the outermost area to the innermost area. These observed different wrinkle wavelengths and amplitudes within the stripes indicated shape-dependent mechanical properties of patterned polymer stripes. The precise prediction and evaluation of mechanical moduli of patterned polymer thin films will provide useful guidance to rationally design and control over the wrinkling profiles for a wealth of applications in low-cost, flexible electronics, optoelectronics.

Introduction

Surface instabilities in organic and inorganic thin films have received considerable attention due to the ease of using self-organization in such systems to create well-defined and complex topological features.[1-3] Spontaneous formation of highly-ordered, intriguing surface wrinkles of thin, stiff polymer films attached to a relatively compliant substrate represents one class of instability-driven self-organization. These highly structured wrinkles with

characteristic wavelength and amplitude can be employed in a variety of practical applications, including diffraction gratings,[4, 5] optical sensors,[5-9] smart adhesives,[10-22] mechanical strain sensors,[23-33] microfluidic sorters,[17, 34-38] cell culture surfaces,[39-45] stretchable electronics, thin film metrology,[46-50] among other areas. In this regard, surface wrinkling has been utilized as a tool for characterizing materials and creating surfaces with functional patterned topologies.[51] However, the wrinkles are often formed in planar continuous films or topographically flat, strictly periodic patterns. In the latter, these microscopic patterns are often prepared by lithography techniques. In stark contrast to the surface wrinkling that has been widely studied in planar and periodically patterned films, the instabilities in gradient patterned polymer thin films and thus mechanical properties have not yet been explored.

Wrinkling of thin stiff film on a soft substrate in the presence of internal or external deformation is a common phenomenon throughout nature and technology. Three main wrinkles are widely studied, which includes: Thermal expansion-induced wrinkling: Complex, ordered wrinkles of thin stiff films can form due to a mismatch of thermal expansion coefficients between upper layer and lower layer when the thermally expanded lower compliant substrate is cooled down to ambient temperature.[46, 52-56]Solvent diffusion-induced wrinkling***:*** When polymer thin film is exposed to a saturated solvent vapor, the internal osmotic pressure is induced by the preferential swelling of the lower stationary soft substrate (i.e., solvent vapor diffusion), resulting in a net compressive stress in the system after the removal of vapor, which in turn leading to the formation of stimuli-responsive surface wrinkling.[57-60] And mechanically-driven wrinkling***:*** The wrinkling also appears as a result of the competition between the bending energy of the stiff upper film and deforming

(i.e., stretching) energy of the soft lower support. By mechanically compressing or stretching (or releasing) the upper film that situates on a compliant substrate (or pre-stretched substrate), wrinkling patterns can display rich surface morphologies and multiple-scale ordering over large areas.[61, 62]

In the letter, by combining the solvent-induced preferential swelling of Polyvinylpyrrolidone (PVP) substrate and wrinkling effect due to modulus mismatch in the upper poly methyl methacrylate (PMMA) stripes and PVP thin film, we present the formation of hierarchically well-ordered wrinkled patterns over large areas. The key difference from the prior reports on swelling-induced surface pattern formation is that we create gradient stripes via controlled evaporative self-assembly (CESA), with decreasing width and height from the outermost area to the innermost area. These observed different wrinkle wavelengths and amplitudes within the stripes indicated shape-dependent mechanical properties of patterned polymer stripes. Moreover, when using PS-b-P4VP instead of PMMA deposited on the PVP thin film, intriguing three-level hierarchical micelle structures can be yielded.

Experimental Section.

Evaporative Self-Assembly of the PMMA and PS-b-P4VP toluene Solution in a Cylinder-on-Si Geometry. Polyvinylpyrrolidone (PVP) dissolved in ethanol (Concentration: 4mgmL^{-1}) was spin-coated on the silicon substrate (spin speed=2000rpm for 60s) as the soft substrate for the future CESA experiment. Poly (methyl methacrylate) (PMMA, *Mn* = 534 kgmol^{-1}, PDI = 1.57) and Polystyrene-block-poly (4-vinylpyridine) (PS-b-P4VP; number average molecular weight: PS=41.0 kgmol^{-1}, P4VP=24.0 kgmol^{-1}; Polydispersity=1.09;

Polymer Source, Inc.) was dissolved in toluene at a concentration of 0.2 $mgmL^{-1}$ and 0.1 $mgmL^{-1}$, and purified with 200 nm polytetrafluoroethylene (PTFE) filters, respectively. The cylinder lens (L=9.5mm, H=4.0mm, W=11.0mm, Figure 43b) and silicon substrate were used as the upper and lower surface, respectively, to construct a confined geometry. The silicon substrates were cleaned with a mixture of sulfuric acid and Nochromix, then rinsed extensively with deionized (DI) water and blow-dried with N_2. The cylinder-on-Si geometry was placed in a sealed chamber to minimize possible air convection and maintain constant temperature during the evaporation process.

Swelling-induced Wrinkles. The regular PMMA and PS-b-P4VP patterns formed on the PVP thin film were exposed to ethanol vapor in a closed vessel (Figure 43). The small piece of gauze soaked with ethanol solvent was placed into a 33 cm^3 vessel. The vessel was sealed by Teflon and placed in an argon grove box to avoid temperature and humidity variation.

Characterization. The surface structures produced on Si substrate were characterized by optical microscopy (Olympus BX51 in the reflection mode) and atomic force microscopy (ICON, Bruker). Vista probes (T190) with spring constants $48Nm^{-1}$ were used as scanning probes.

Results and Discussion

PMMA was used as nonvolatile solutes to prepare PMMA toluene solutions with the concentration 0.2 $mgmL^{-1}$. The evaporation, in general, took less than 30 min to complete. After the evaporation was complete, two surfaces (spherical lens and Si) were separated and examined by using OM. Only the patterns on Si were evaluated. Highly ordered gradient concentric rings of PMMA, persisting toward the sphere/Si contact center, were obtained

over the entire surfaces of the sphere and Si except the region where the sphere was in contact with Si (Figure 43). The formation of periodic, gradient rings was a direct consequence of controlled, repetitive 'stick-slip' motion of the contact line, resulting from the competition of linear pinning force and nonlinear depinning force (i.e., capillary force) in the sphere-on-Si geometry. This is in sharp contrast with irregular concentric rings formed in an unbound liquid by stochastic 'stick-slip' motion of the contact line, suggesting that the use of the sphere-on-Si geometry rendered control over the evaporation rate, and is effective in improving the stability against the convection.

Subsequently, the regular PMMA patterns formed on the PVP thin film were exposed to ethanol vapor in a closed vessel. Here, wrinkling can be induced by the ethanol vapor, as shown in the optical microscopy images in Figure 43. Due to the gradient of the stripes, the wrinkles patterns are obviously different (e.g., the wavelength of wrinkles) from outermost area to the innermost area. Representative AFM height images of wrinkles within the stripes with different radial distances, X (Fig. 1), away from the center of the sphere/Si contact are shown in Figure 44. The recession of the center-to-center distance between adjacent rings, λ_{C-C}, and the height of the ring, h, the width of the stripe, w, the wavelength and the amplitude were clearly evident. As the solution front moved toward the center of the cylinder/Si contact due to evaporative loss of toluene, all the numbers mentioned above are decreased. Since the mechanical properties (e.g. Young's modules) are highly dependent on the measured wavelength of the stripes, these gradient polymers stripes had clearly shape-dependent mechanical properties.

The mechanism leading to the growth of these new hierarchical structures of wrinkles in a confinement stripe should involve viscous flow in the polymer layer and solvent

diffusion. To get a first insight into this complex mechanism, the in-situ OM observation was conducted to reveal the formation process of wrinkles, as shown in Figure 45. At first, parallel wrinkles are observed when the solvent diffuses from the edge yielding a linear front. Subsequently, the wrinkles domains grow and meet together at the center of the stripes. These immersed wrinkles from two edges of one stripe make these wrinkles parallel to each other locally within the stripe.

When choosing PS-b-P4VP as the building block, instead of PMMA, intriguing three-level hierarchical micelle structures can be induced. Since toluene is a strong selective solvent for PS, PS-b-P4VP copolymers spontaneously assemble into spherical micelles with a soluble PS corona and an insoluble P4VP core in toluene (Figure 43a).[63-65] The PS blocks formed coronae around insoluble P4VP cores to reduce energetically unfavorable interactions with the solvent.[65, 66] As shown in Figure 4, micelles were wrinkled within one stripe. It is noteworthy to find at the top of the wrinkles, the micelles are separated a litter, however, at the bottom of the wrinkles, the micelles are squeezed. In other words, the distances between the micelles are modified by the wrinkles.

Conclusions

In summary, by combining the solvent-induced preferential swelling of PVP substrate and wrinkling effect due to modulus mismatch in the upper PMMA stripes and PVP thin film, we present the formation of hierarchically well-ordered wrinkled patterns over large areas. The key difference from the prior reports on swelling-induced surface pattern formation is that we create gradient stripes via controlled evaporative self-assembly (CESA), with decreasing width and height from the outermost area to the innermost area. These observed

different wrinkle wavelengths and amplitudes within the stripes indicated shape-dependent mechanical properties of patterned polymer stripes. Moreover, when using PS-b-P4VP instead of PMMA deposited on the PVP thin film, intriguing three-level hierarchical micelle structures can be yielded. The precise prediction and evaluation of mechanical moduli of patterned polymer thin films will provide useful guidance to rationally design and control over the wrinkling profiles for a wealth of applications in low-cost, flexible electronics, optoelectronics.

Figures

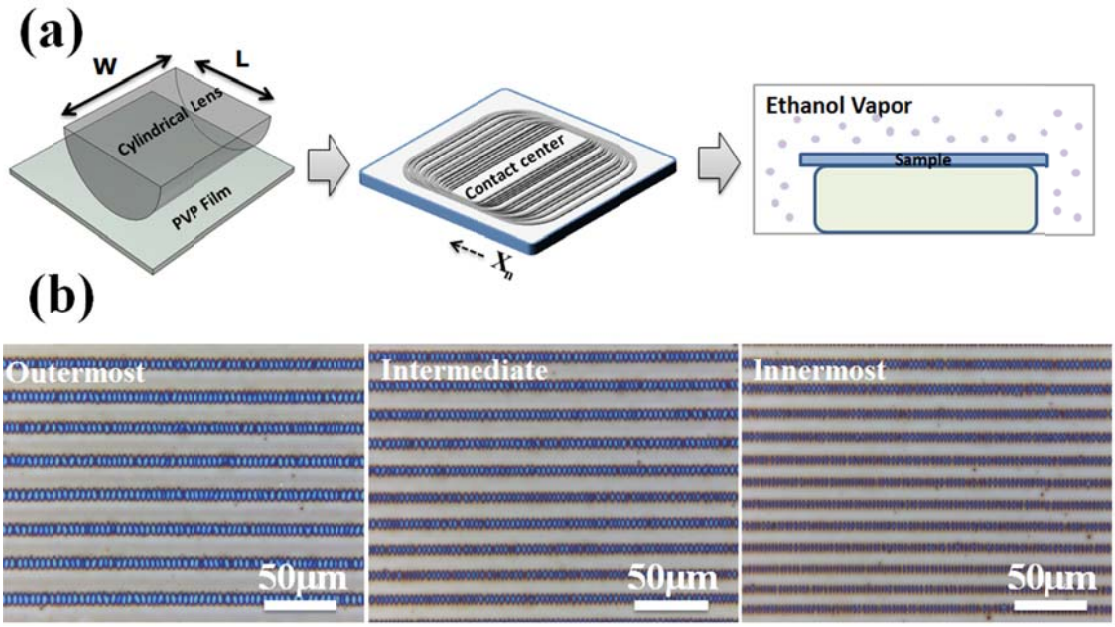

Figure 43. (a) Schematic drawing illustrating sequential formation of gradient concentric stripes with wrinkles by combining the solvent-induced preferential swelling and the solvent evaporation in the geometry. (b) Optical micrograph images of PMMA wrinkles at the left: outermost region (X1=4500μm); middle: intermediate region (X2=4000 μm) and right innermost region (X3=3500 μm), respectively.

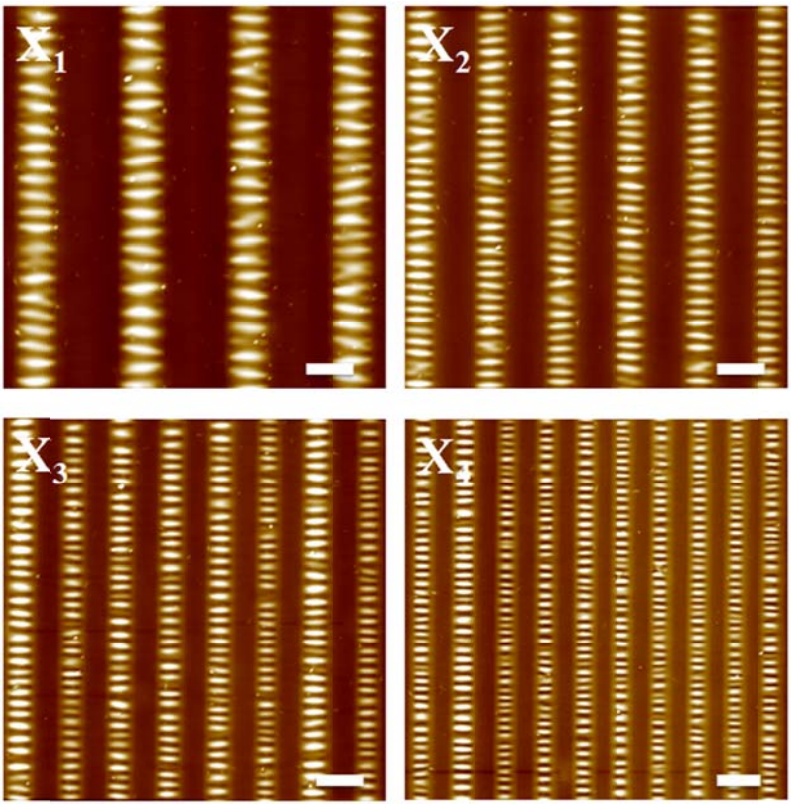

Figure 44. Representative AFM height images in different location. The distance between adjacent stripes, the height of stripes, and the width of stripes gradually decreased at the four regions.

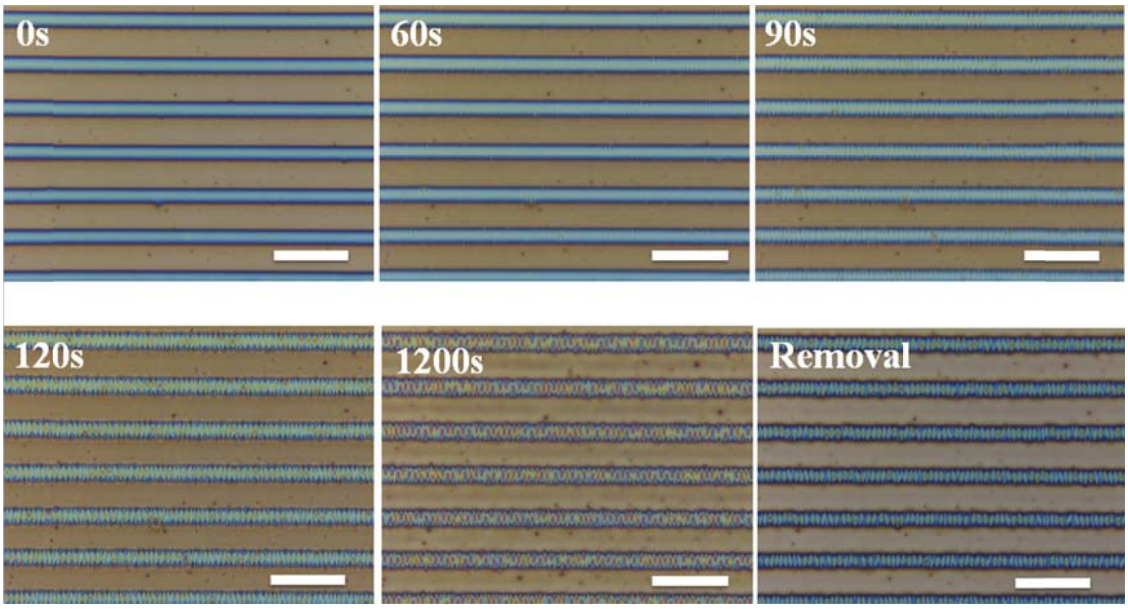

Figure 45. In situ OM observation of the formation of swelling-induced wrinkles.

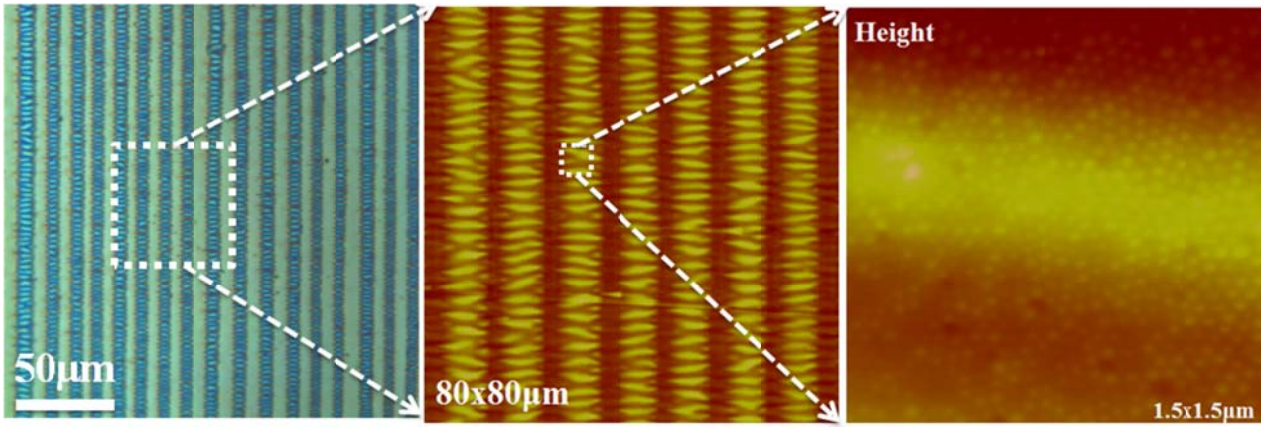

Figure 46. OM and AFM images of wrinkles formed within the PS-P4VP micelle stripes.

References

1. Barth, J. V.; Costantini, G.; Kern, K., *Nature* **2005,** *437* (7059), 671-679.
2. Lazzari, M.; Lopez-Quintela, M. A., *Adv. Mater.* **2003,** *15* (19), 1583-1594.
3. Wu, L. Q.; Payne, G. F., *Trends Biotechnol.* **2004,** *22* (11), 593-599.
4. Harrison, C.; Stafford, C. M.; Zhang, W. H.; Karim, A., *Appl. Phys. Lett.* **2004,** *85* (18), 4016-4018.
5. Yu, C. J.; O'Brien, K.; Zhang, Y. H.; Yu, H. B.; Jiang, H. Q., *Appl. Phys. Lett.* **2010,** *96* (4).
6. Kolaric, B.; Vandeparre, H.; Desprez, S.; Vallee, R. A. L.; Damman, P., *Appl. Phys. Lett.* **2010,** *96* (4).
7. Mei, Y. F.; Kiravittaya, S.; Benyoucef, M.; Thurmer, D. J.; Zander, T.; Deneke, C.; Cavallo, F.; Rastelli, A.; Schmidt, O. G., *Nano Lett.* **2007,** *7* (6), 1676-1679.
8. Jiang, C. Y.; McConney, M. E.; Singamaneni, S.; Merrick, E.; Chen, Y. C.; Zhao, J.; Zhang, L.; Tsukruk, V. V., *Chem. Mater.* **2006,** *18* (11), 2632-2634.
9. Burton, K.; Taylor, D. L., *Nature* **1997,** *385* (6615), 450-454.
10. Ke, C. H.; Zheng, M.; Bae, I. T.; Zhou, G. W., *J. Appl. Phys.* **2010,** *107* (10).
11. Autumn, K.; Liang, Y. A.; Hsieh, S. T.; Zesch, W.; Chan, W. P.; Kenny, T. W.; Fearing, R.; Full, R. J., *Nature* **2000,** *405* (6787), 681-685.
12. Chen, B.; Shi, X. H.; Gao, H. J., *Proceedings of the Royal Society a-Mathematical Physical and Engineering Sciences* **2008,** *464* (2091), 657-671.
13. Chung, J. Y.; Kim, K. H.; Chaudhury, M. K.; Sarkar, J.; Sharma, A., *Eur. Phys. J. E* **2006,** *20* (1), 47-53.
14. Chan, E. P.; Greiner, C.; Arzt, E.; Crosby, A. J., *Mater. Res. Bull.* **2007,** *32* (6), 496-503.
15. Nolte, A. J.; Chung, J. Y.; Walker, M. L.; Stafford, C. M., *Acs Applied Materials & Interfaces* **2009,** *1* (2), 373-380.
16. Lin, P. C.; Vajpayee, S.; Jagota, A.; Hui, C. Y.; Yang, S., *Soft Matter* **2008,** *4* (9), 1830-1835.
17. Majumder, A.; Ghatak, A.; Sharma, A., *Science* **2007,** *318* (5848), 258-261.
18. Chung, J. Y.; Chaudhury, M. K., *Journal of the Royal Society Interface* **2005,** *2* (2), 55-61.
19. Vandeparre, H.; Leopoldes, J.; Poulard, C.; Desprez, S.; Derue, G.; Gay, C.; Damman, P., *Phys. Rev. Lett.* **2007,** *99* (18).
20. Jeong, H. E.; Kwak, M. K.; Suh, K. Y., *Langmuir.* **2010,** *26* (4), 2223-2226.
21. Chan, E. P.; Smith, E. J.; Hayward, R. C.; Crosby, A. J., *Adv. Mater.* **2008,** *20* (4), 711-+.
22. Hamm, E.; Reis, P.; LeBlanc, M.; Roman, B.; Cerda, E., *Nature Mater.* **2008,** *7* (5), 386-390.
23. Zhang, P. F.; Yang, D. Y.; Li, Z.; Ma, H. W., *Soft Matter* **2010,** *6* (18), 4580-4584.
24. Huang, W. M.; Hu, Y. Y.; An, L., *Appl. Phys. Lett.* **2005,** *87* (20).
25. Maune, H.; Bockrath, M., *Appl. Phys. Lett.* **2006,** *89* (17).
26. Xie, T.; Xiao, X. C.; Li, J. J.; Wang, R. M., *Adv. Mater.* **2010,** *22* (39), 4390-+.
27. Chun, I. S.; Challa, A.; Derickson, B.; Hsia, K. J.; Li, X. L., *Nano Lett.* **2010,** *10* (10), 3927-3932.
28. Ohzono, T.; Shimomura, M., *Langmuir.* **2005,** *21* (16), 7230-7237.
29. Han, X. D.; Zhang, Y. F.; Zheng, K.; Zhang, X. N.; Zhang, Z.; Hao, Y. J.; Guo, X. Y.; Yuan, J.; Wang, Z. L., *Nano Lett.* **2007,** *7* (2), 452-457.
30. Maranganti, R.; Sharma, P., *J. Mech. Phys. Solids.* **2007,** *55* (9), 1823-1852.
31. Gemici, Z.; Smadbeck, P.; Rubner, M. F.; Cohen, R. E., *Abstracts of Papers of the American Chemical Society* **2008,** *235*, 117-PMSE.
32. Kim, D. H.; Kim, Y. S.; Wu, J.; Liu, Z. J.; Song, J. Z.; Kim, H. S.; Huang, Y. G. Y.; Hwang, K. C.; Rogers, J. A., *Adv. Mater.* **2009,** *21* (36), 3703-+.
33. Hobbie, E. K.; Simien, D. O.; Fagan, J. A.; Huh, J. Y.; Chung, J. Y.; Hudson, S. D.; Obrzut, J.; Douglas, J. F.; Stafford, C. M., *Phys. Rev. Lett.* **2010,** *104* (12).

34. Monteux, C.; Kirkwood, J.; Xu, H.; Jung, E.; Fuller, G. G., *Phys. Chem. Chem. Phys.* **2007,** *9* (48), 6344-6350.
35. Arscott, S.; Peytavit, E.; Vu, D.; Rowe, A. C. H.; Paget, D., *J. Micromech. Microeng* **2010,** *20* (2).
36. Fasolka, M. J.; Stafford, C. M.; Beers, K. L., Gradient and Microfluidic Library Approaches to Polymer Interfaces. In *Polymer Libraries*, 2010; Vol. 225, pp 63-105.
37. So, J. H.; Thelen, J.; Qusba, A.; Hayes, G. J.; Lazzi, G.; Dickey, M. D., *Adv. Funct. Mater.* **2009,** *19* (22), 3632-3637.
38. Khare, K.; Zhou, J. H.; Yang, S., *Langmuir.* **2009,** *25* (21), 12794-12799.
39. Jiang, X. Y.; Takayama, S.; Qian, X. P.; Ostuni, E.; Wu, H. K.; Bowden, N.; LeDuc, P.; Ingber, D. E.; Whitesides, G. M., *Langmuir.* **2002,** *18* (8), 3273-3280.
40. Teixeira, A. I.; Abrams, G. A.; Bertics, P. J.; Murphy, C. J.; Nealey, P. F., *J. Cell Sci.* **2003,** *116* (10), 1881-1892.
41. Burton, K.; Park, J. H.; Taylor, D. L., *Mol. Biol. Cell* **1999,** *10* (11), 3745-3769.
42. Quero, F.; Nogi, M.; Yano, H.; Abdulsalami, K.; Holmes, S. M.; Sakakini, B. H.; Eichhorn, S. J., *Acs Applied Materials & Interfaces* **2010,** *2* (1), 321-330.
43. Miquelard-Garnier, G.; Zimberlin, J. A.; Sikora, C. B.; Wadsworth, P.; Crosby, A., *Soft Matter* **2010,** *6* (2), 398-403.
44. Lam, M. T.; Clem, W. C.; Takayama, S., *Biomaterials.* **2008,** *29* (11), 1705-1712.
45. Harris, A. K.; Wild, P.; Stopak, D., *Science* **1980,** *208* (4440), 177-179.
46. Stafford, C. M.; Harrison, C.; Beers, K. L.; Karim, A.; Amis, E. J.; Vanlandingham, M. R.; Kim, H. C.; Volksen, W.; Miller, R. D.; Simonyi, E. E., *Nature Mater.* **2004,** *3* (8), 545-550.
47. Cao, Y. P.; Zheng, X. P.; Li, B.; Feng, X. Q., *Scripta Mater.* **2009,** *61* (11), 1044-1047.
48. Wilder, E. A.; Guo, S.; Lin-Gibson, S.; Fasolka, M. J.; Stafford, C. M., *Macromolecules* **2006,** *39* (12), 4138-4143.
49. Khang, D. Y.; Rogers, J. A.; Lee, H. H., *Adv. Funct. Mater.* **2009,** *19* (10), 1526-1536.
50. Aoyanagi, Y.; Hure, J.; Bico, J.; Roman, B., *Soft Matter* **2010,** *6* (22), 5720-5728.
51. Chung, J. Y.; Nolte, A. J.; Stafford, C. M., *Adv. Mater.* **2011,** *23* (3), 349-368.
52. Peinado, C.; Corrales, T.; Catalina, F.; Pedron, S.; Quiteria, V. R. S.; Parellada, M. D.; Barrio, J. A.; Olmos, D.; Gonzalez-Benito, J., *Polym. Degrad. Stabil.* **2010,** *95* (6), 975-986.
53. Zhou, J.; Berry, B.; Douglas, J. F.; Karim, A.; Snyder, C. R.; Soles, C., *Nanotechnology* **2008,** *19* (49).
54. Kim, T. H.; Choi, W. M.; Kim, D. H.; Meitl, M. A.; Menard, E.; Jiang, H. Q.; Carlisle, J. A.; Rogers, J. A., *Adv. Mater.* **2008,** *20* (11), 2171-+.
55. Li, S. P.; Chu, D. P.; Koltsov, D. K.; Fu, Y. T.; Welland, M. E., *Nanotechnology* **2008,** *19* (23).
56. Chan, E. P.; Page, K. A.; Im, S. H.; Patton, D. L.; Huang, R.; Stafford, C. M., *Soft Matter* **2009,** *5* (23), 4638-4641.
57. Kohler, R.; Donch, I.; Ott, P.; Laschewsky, A.; Fery, A.; Krastev, R., *Langmuir.* **2009,** *25* (19), 11576-11585.
58. Singamaneni, S.; McConney, M. E.; Tsukruk, V. V., *Acs Nano* **2010,** *4* (4), 2327-2337.
59. Guvendiren, M.; Yang, S.; Burdick, J. A., *Adv. Funct. Mater.* **2009,** *19* (19), 3038-3045.
60. Jing, B. X.; Zhao, J.; Wang, Y.; Yi, X.; Duan, H. L., *Langmuir.* **2010,** *26* (11), 7651-7655.
61. Yang, S.; Khare, K.; Lin, P. C., *Adv. Funct. Mater.* **2010,** *20* (16), 2550-2564.
62. Efimenko, K.; Rackaitis, M.; Manias, E.; Vaziri, A.; Mahadevan, L.; Genzer, J., *Nature Mater.* **2005,** *4* (4), 293-297.
63. Forster, S.; Antonietti, M., *Adv. Mater.* **1998,** *10* (3), 195-195.
64. Sohn, B. H.; Choi, J. M.; Yoo, S. I.; Yun, S. H.; Zin, W. C.; Jung, J. C.; Kanehara, M.; Hirata, T.; Teranishi, T., *J. Am. Chem. Soc.* **2003,** *125* (21), 6368-6369.

65. Forster, S.; Zisenis, M.; Wenz, E.; Antonietti, M., *J. Chem. Phys.* **1996,** *104* (24), 9956-9970.
66. Li, Z.; Zhao, W.; Liu, Y.; Rafailovich, M. H.; Sokolov, J.; Khougaz, K.; Eisenberg, A.; Lennox, R. B.; Krausch, G., *J. Am. Chem. Soc.* **1996,** *118* (44), 10892-10893.

CHAPTER 9. SPONTANEOUS FORMATION OF WELL-ORDERED MICROCHANNELS VIA EVAPORATIVE SELF-ASSEMBLY

Modified from a manuscript to be submitted

Wei Han, Bo Li, and Zhiqun Lin*

Abstract

When a latex particle dispersion freely evaporated on a rigid substrate, the enormous stresses developing during the evaporation process can fracture the thin film and prolongate the cracks towards the center, thus forming intriguing well-aligned microchannels in the patterns. By simply tailoring the upper confinement, the imposed geometry (i.e., needle and slides) directs the formation of a variety of complex, highly regular patterns in a precisely controllable manner. Subsequently, these microchannel patterns can be served as templates to direct the formation of Au stripes. This simple and cost-effective approach opens a new avenue for producing macroscopic patterns that have potential as scaffolds or substrates in the field of microelectronics or microfluidic-based biochips.

Introduction

Surface patterning of well-ordered two-dimensional (2D) structures have attracted many interests recently due to their potential applications in optics,[1, 2] optoelectronics,[3, 4] electronics,[5] magnetic materials[6] and biotechnology.[7] Compared to conventional top-down techniques (e.g., photolithography, e-beam lithography, soft-lithography and nanoimprint lithography), self-assembly is the self-made process of directing materials into surface patterns or structures in the absence of additional external forces, thus providing a bottom-up,

lithography-free and cons-effective approach to construct highly ordered, often intriguing structures, which can be applicable for potential applications, e.g., optical and electronic devices.[8, 9] Especially, among variety of self-assembly processes, dynamic (i.e., energy-dissipative) self-assembly of the components by solvent depletion in a single droplet evaporation process has been recognized as recognized as an extremely simple way to produce a diverse range of intriguing surface patterns in simple, rapid, inexpensive and scalable manner, thus yielding dissipative, complex and ordered structures, e.g., concentric coffee rings, fingering patterns, and thin structured films of colloids, over large areas. [10-26]

Latex particles dispersions with a liquid phase solvent, which are widely used as a classic research system, self-assemble into a wide range of intriguing and ordered structures after complete drying. Recently, a variety of methods have been adopted for structuring particles on a flat substrate, including controlled evaporative self-assembly, [2, 27, 28] surface modification,[29, 30] and template-directed assembly [31-33]. In contrast to controlled assembling and positioning colloidal particles into well-ordered arrays or stripes, crack during drying of latex particle dispersion has also received considerable attention from both academic and industrial researchers.[34-38] It has been investigated for a variety of systems, including wet clays, ceramic films, colloidal dispersions and etc.[39-44] These cracks can exhibit intriguing morphologies, including two-dimensional networks and logarithmic spirals. [45, 46] Crack formation has been widely studied in experiments, and many models have been developed to describe the qualitative features of crack morphology and the drying process responsible for cracking. [36, 47] In contrast to the well-studied drying mechanisms, there is little report focused on the control of directional cracks to form intriguing patterns with large areas, and its application of the crack template to form replica inorganic stripes. In this letter, we report the

highly ordered directional channel patterns over large areas formed via evaporation-induced self-assembly. During the evaporation process, the enormous stresses induced during evaporation fractured the thin film and prolongated the cracks inward to the center. By employing different upper confinement (e.g., needle or glass slide), complex but ordered microchannel patterns can be precisely controlled and yielded. Subsequently, the microchannels served as template to direct the formation of Au stripes with unprecedented regularity. This simple and cost-effective approach opens a new avenue for producing macroscopic patterns that have potential as scaffolds or substrates in the field of microelectronics or microfluidic-based biochips.

Experimental Section.

Evaporative Self-Assembly of PS Latex Aqueous Solution. The aqueous solutions containing PS latex particles with diameter of 50 nm was purchased from Thermo Scientific (c = 1.0 wt% particle solids) without further purification. The Si substrate was cleaned with a mixture of sulfuric acid and Nochromix, then rinsed extensively with deionized (DI) water and blow-dried with N_2. Hexamethyldisilazane (HMDS，99.9%) substrate was prepared by spin-coating (3000rpm and 60s) on the Si substrate, thus changing its surface property from hydrophilic to hydrophobic. The whole setup (the substrate and heater) was placed in a sealed chamber to minimize possible air convection and maintain constant temperature during the evaporation process. After the evaporation was complete, the patterns formed on the substrates (Si or HMDS) were investigated.

Characterization. The surface structures produced on Si substrate were characterized by optical microscopy (Olympus BX51 in the reflection mode) and atomic force microscopy

(ICON scanning force microscope in the tapping mode). Vista probes (T190) with spring constants 48Nm^{-1} were used as scanning probes. Patterns of PS latex microchannels were observed by a field-emission scanning electron microscope (FE-SEM; FEI Quanta 250) operating at 20kv in High Vacuum.

Results and Discussion

The aqueous solutions containing PS latex particles (D=50 nm) were chosen as building blocks to prepare the microchannle patterns by simply dropping small amount of solution (V=15μL) on the rigid silicon substrate. To promote the evaporation of water, the aqueous solution was heated at a fixed temperature (T = 60^0C), by placing a heat plate beneath the Si substrate. Previous we reported the formation of parallel PS latex stripes via confined evaporative self-assembly (CESA), due to the controlled and repetitive "stick-slip" motion of the three-phase contact line.[28] However, instead, here an intriguing well-ordered "spoke" like pattern with large areas was observed on the silicon substrate after complete evaporation, as shown in Figure 47. The heated substrate enhances the evaporation process, thus making the whole process complete less than 5 min. The entire pattern was formed over 6x6mm^2 surface areas and the optical microscope (OM) images only showed a small part of it. It is noteworthy that these "spokes" prolongate from the edge to the center of the pattern without intersecting each other, and locally, the patterns appear as well-ordered parallel stripes, as shown in the lower left panel in Figure 47. It is also of interest to note that the well-ordered "spoke" like pattern observed here were highly reproducible.

Scanning electron microscope (FE-SEM, see Experimental Section) was used to closely examine the detailed surface morphology and the packing of the PS latex particles, as shown in Figure 48. From SEM images, it is clearly observed that these "spokes" are the

arrays of PS latex microchannels (cracks), with the width of about 1μm. The distance between the adjacent channels varies from 10-20μm, which is highly related to the local film thickness.[34, 35] As the zoom-in image (Figure 47c) shown, the crack is quite sharp and the film around the cracks was consisting of more than 10 layers of particles. Between the cracks, it is noteworthy to observe that highly close-packed latex particles with small surface roughness formed between adjunct cracks, as shown in Figure 47d. During the evaporation, the particles at the surface of the film will be pulled together due to the capillary forces, and the rapidly descending meniscus push the particles down, taken together, thus forming these intriguing close-packed PS latex particles on the surface of the film.[48] The cross-section of AFM height image reveals that these channels have a relatively depth of about 400nm. However, since the AFM tip may not reach the bottom of the cracks (See Supporting Information), this number is suspicious. When prepared the sample on the glass substrate with some concentration and heating temperature, the cracks were also clearly observed on the back side of the sample (See Supporting Information). It indicates that the cracks penetrate the whole film, which means, the depth of the crack is equal to the local thickness of the thin film.

In situ OM observation reveals the dynamic drying process, as shown in Figure 49. The evaporation of the solvent concentrates the particles into a close packing and form a thin film first (Figure 49b), and no cracks observed at this stage. Further evaporation pulls the three phase interface inward, at the same time, generating a negative capillary pressure $P \sim \frac{\gamma}{R}$, which is in proportion to the surface tension of liquid γ and the curvature of the meniscus R. Atmospheric pressure puts the entire film into compression, thus inducing stresses since the rigid substrate prevents the deformation laterally. If these stresses exceed the yield stress of

the packed particle film, the strain energy stored in the film can be released by creating new interfaces, thus a crack is formed, as shown in Figure 49c. The newly formed crack can be served as the nucleation and propagates in a direction perpendicular to the drying front, as the drying front moving inward due to the continued evaporation. [34, 35] Finally all the cracks end and concentrate at the center point of the thin film, thus forming the "spoke" like patterns, as shown in Figure 49a and Figure 49d. It is of interest to observe that there is a small region I (marked in Figure 49c and 3d) between the cracks and the moving drying front, which is the region the particles are also close packed.[48] The width of the region I was observed to remain approximately constant during the evaporation process, which indicates the moving velocity of the cracks are only dependent on the moving speed of the drying front. These observations are consistent with other literature reports of drying colloidal films. [12, 34-37] It is noteworthy that, in contrast to the random shrinkage-crack patterns, drying-induced cracks can invade a surface, penetrate the whole film, and propagate inward to the center of the thin film, as the movement of the drying front, thus forming directional well-ordered channels, which have potential as scaffolds or substrates in the field of microelectronics or microfluidic-based biochips.

It is well known that the surface wetting ability of substrate will predictably govern the structure formation. Here we repeated the experiment on the hydrophobic HMDS (hexamethyldisilazane) coated substrate. It is no surprising that no well-ordered channels were observed after the evaporation. Instead, highly concentrated ring pattern was observed on the HMDS surface (See Figure S3 in Supporting Information). Due to the large contact angle between the solution and the substrate, the three phase contact line pinned during almost entire evaporation process, thus leading to the familiar "coffee-ring" pattern.

Additionally, we note that the heating temperature (T = 60^{o}C) was critical in the present study. At room temperature, the evaporation rate was quite low at the water/air/substrate three phase contact line, thus making insufficient time for the stress release of the drying front during the evaporation process.[34] As a result, the spatial arrangement of the cracks was no longer unidimensional, instead, secondary branching between cracks were observed and less ordered patterns were formed (Figure S3 in Supporting Information).

It has demonstrated that the confined geometry can be tailor-made to craft a rich family of surface patterns with evaporation induced self-assembly. The variation in size, shape, symmetry, and curvature of confined geometries will inevitably influence the evaporation process and the associated flow field, thus leading to interesting patterns with different morphologies.[49] By manually choosing the upper confinement to different shapes (i.e., two needles, three needles and glass slides) and vertical immersing them into the droplet during the evaporation, different forms of microchannels can be specifically "synthesized". As shown in Figure 4, parallel cracks formed at the side of the gap between two touch points of the needles (Region I in Figure 4a), and at other regions, spoke-like patterns are still retained (Region II in Figure 4a). When using three needles to guide the flow field inside the droplet, similar patterns were formed after evaporation, which is, parallel channels (region I in Figure 4b) and "spokes" (region II in Figure 4b) were created respectively. The forming channel patterns are strongly dependent on the position of these imposed needles and the distance between the needles. It is of interest to observe the parallel stripes with large areas when imposing the glass slide as upper confinement at the center of the droplet. These parallel and directional channels pointed from the edge of the droplet to the contact center between the glass slide and the substrate, as shown in Figure 4c. These specialized

geometries can be further chemically and/or physically modified to afford an even broader range of complex assembled structures.

The unprecedented regularity of these channels makes them intriguing templates for producing ordered metal stripes. After preparing the particle channels, 50nm thick Au was sputtered on the prepared sample. To achieve Au stripes, the sample was then placed in furnace at 400^{o}C for 2h to thermally decompose buried PS Latex particles, followed by extensive ultrasonication in toluene for 30 min, as shown in Figure 51a. In order to remove residual polymers on the surface, these processes (thermally decomposition and ultrasonication) may conduct more than once. OM images showed the "Spoke-like" and parallel Au stripe replica was obtained eventually after unltrasonication in toluene, from the sample created via freely evaporation and confinement under glass slide, respectively (Figure 51b). The order of Au stripes was reminiscent of the arrangement of PS latex channels and was not affected by the thermal treatment and subsequent ultrasonication. A typical AFM height image with a cross-section profile is shown in Figure 51c. The width and height of the Au stripe are about 600nm and 40nm, respectively. Compare to the original width of particle channel (about 1μm), the size decreasing may due to the long diffusion path of gold atoms during sputtering in the channels and little delamination when removing the polymer template. It is noteworthy that little amount of polymer still attached on the surface, as a result, higher thermal temperature or longer sonication are required. However, higher thermal temperature or prolonged sonication was found to cause Au stripes to delaminate from the substrate.[24]

Conclusions

In conclusion, highly ordered PS latex microchannels were formed on the surface via evaporation-induced self-assembly in a simple and cost effective manner. The formation of directional cracks was due the enormous stresses developing during the evaporation process, which can fracture the thin film and prolongate the cracks towards the center. By manually choosing the upper confinement (i.e., needles or glass slides), a range of complex assembled structures was achieved. Subsequently, these PS latex microchannels serve as templates to direct the formation of well-ordered gold stripes. There resulting metal arrays may offer possibilities for many applications, including microelectrics and data storage devices. We envision that the biomaterial, such as DNA, other than inorganic material, can be easily obtained with a rich family of surface patterns from corresponding template produced with different shape of confinement, during the simple evaporation process.

Figures

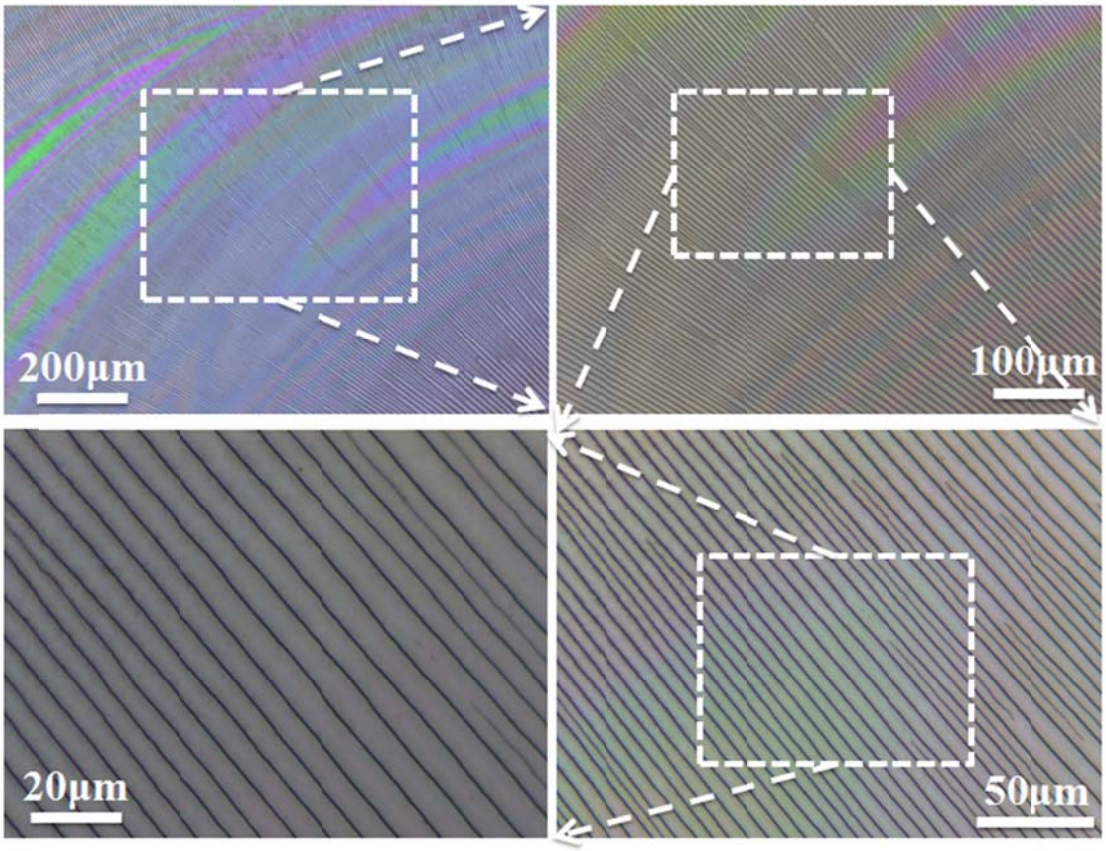

Figure 47. Optical micrograph images of intriguing well-ordered “spoke” like channel pattern on the silicon substrate, with different magnification.

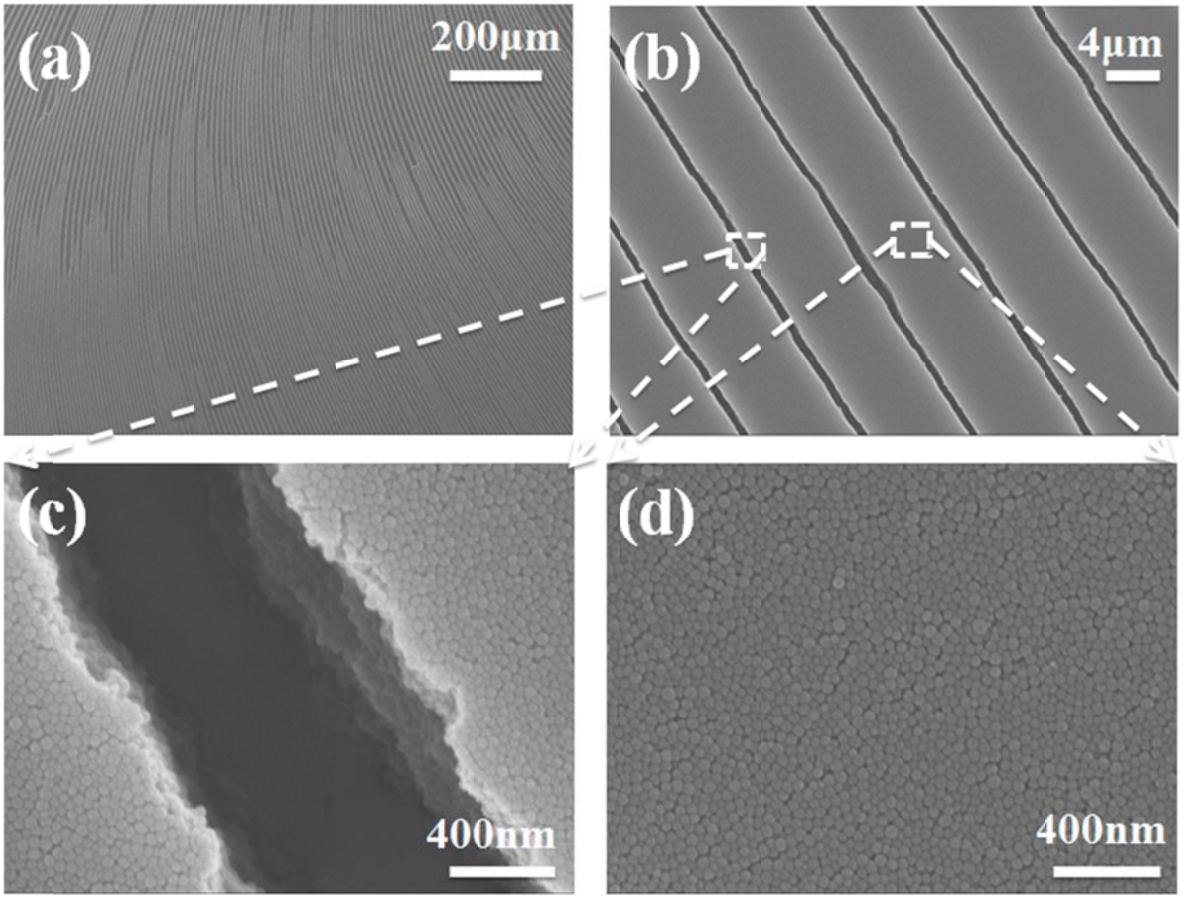

Figure 48. Typical SEM images of PS Latex channels on the silicon substrate, with different magnification. The crack is quite sharp and the film around the cracks was consisting of more than 10 layers of particles. Between adjunct cracks, highly close-packed latex particles were formed.

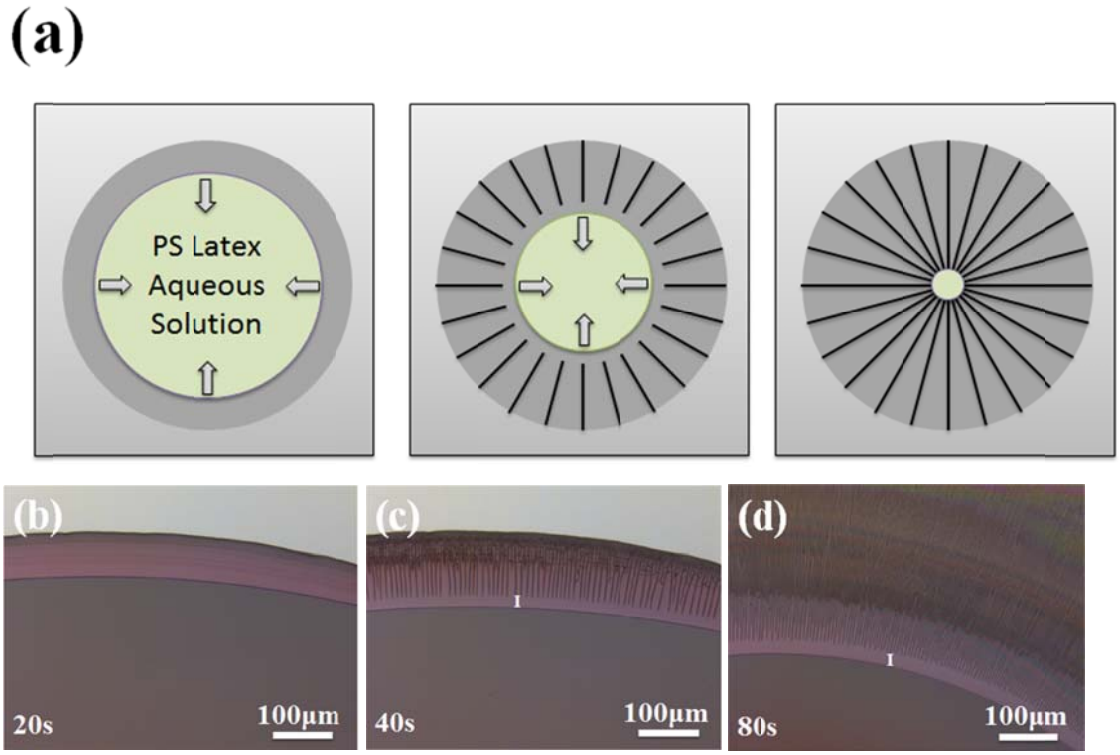

Figure 49. (a) Schematic stepwise representation of formation of PS latex channel pattern. (b)-(d) In situ optical micrograph images observation of formation of PS latex channels, at 20s, 40s and 80s, respectively.

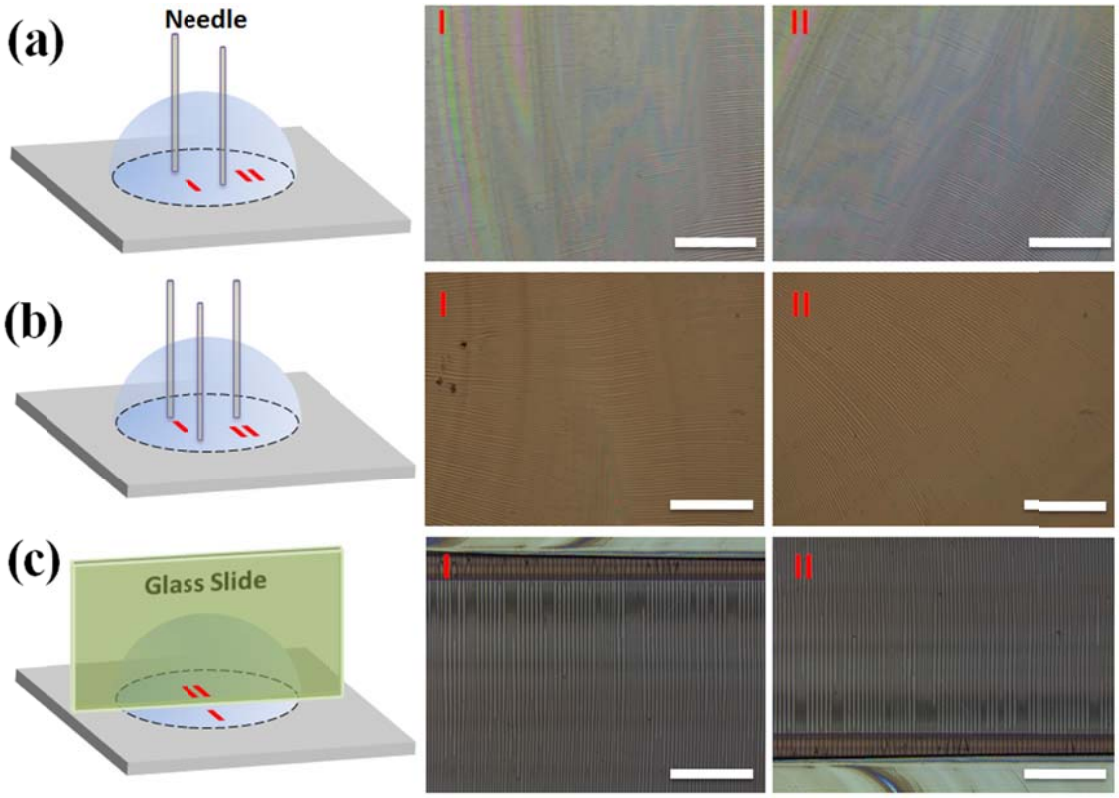

Figure 50. The confined geometry can be tailor-made to craft a rich family of surface patterns. (a) Two needles, (b) three needles (c) glass slide were chosen respectively to influence the evaporation process and the associated flow field, thus leading to interesting patterns with different morphologies.

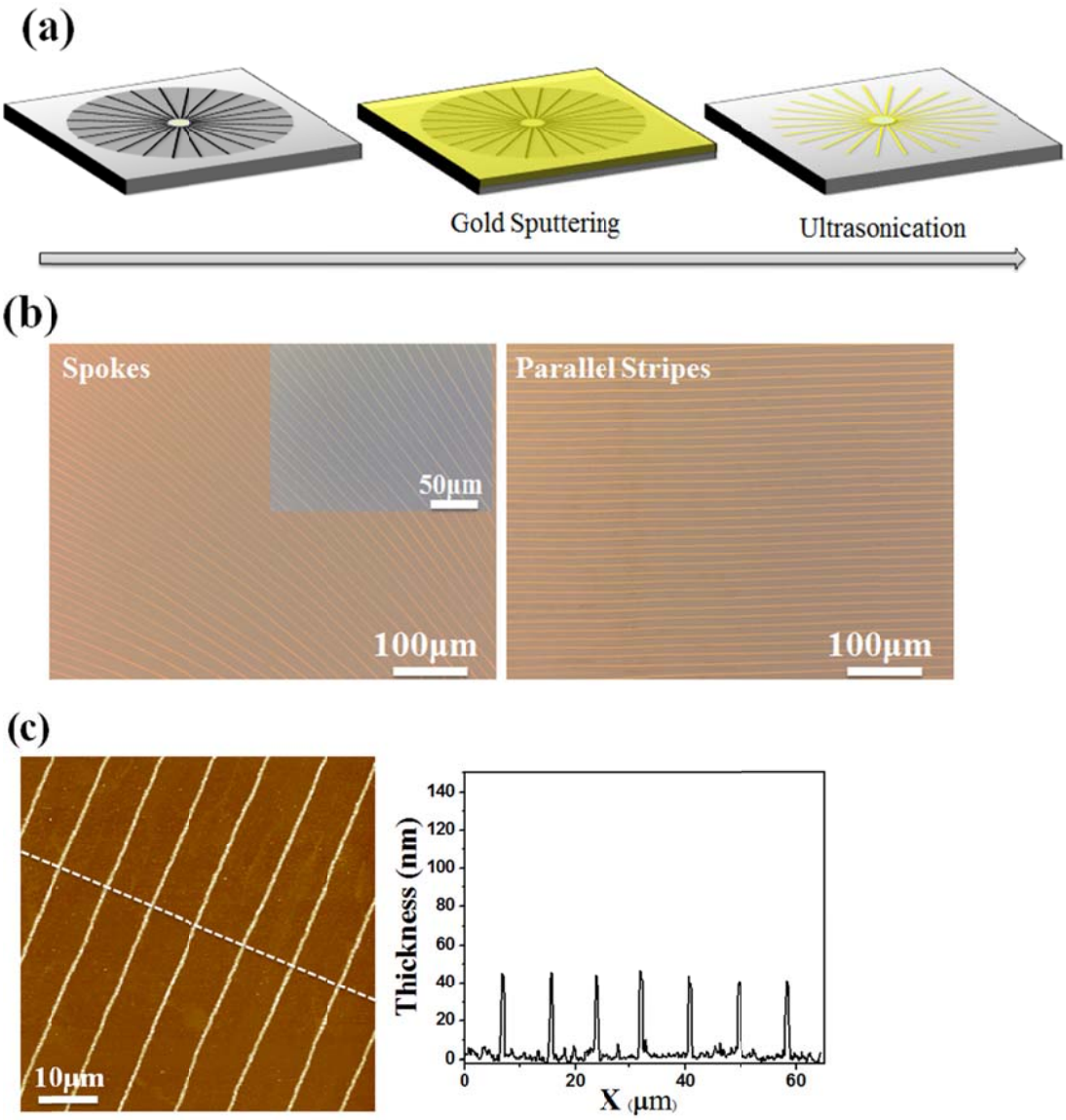

Figure 51. (a) Schematic stepwise representation of preparing Au stripes via PS latex channel pattern template. (b) Optical micrograph images of prepared "Spoke-like" and parallel Au stripes, respectively. (C) Typical AFM images of Au stripes. From the cross-section profile, the width and height of the Au stripe are about 600nm and 40nm, respectively.

Supporting Information

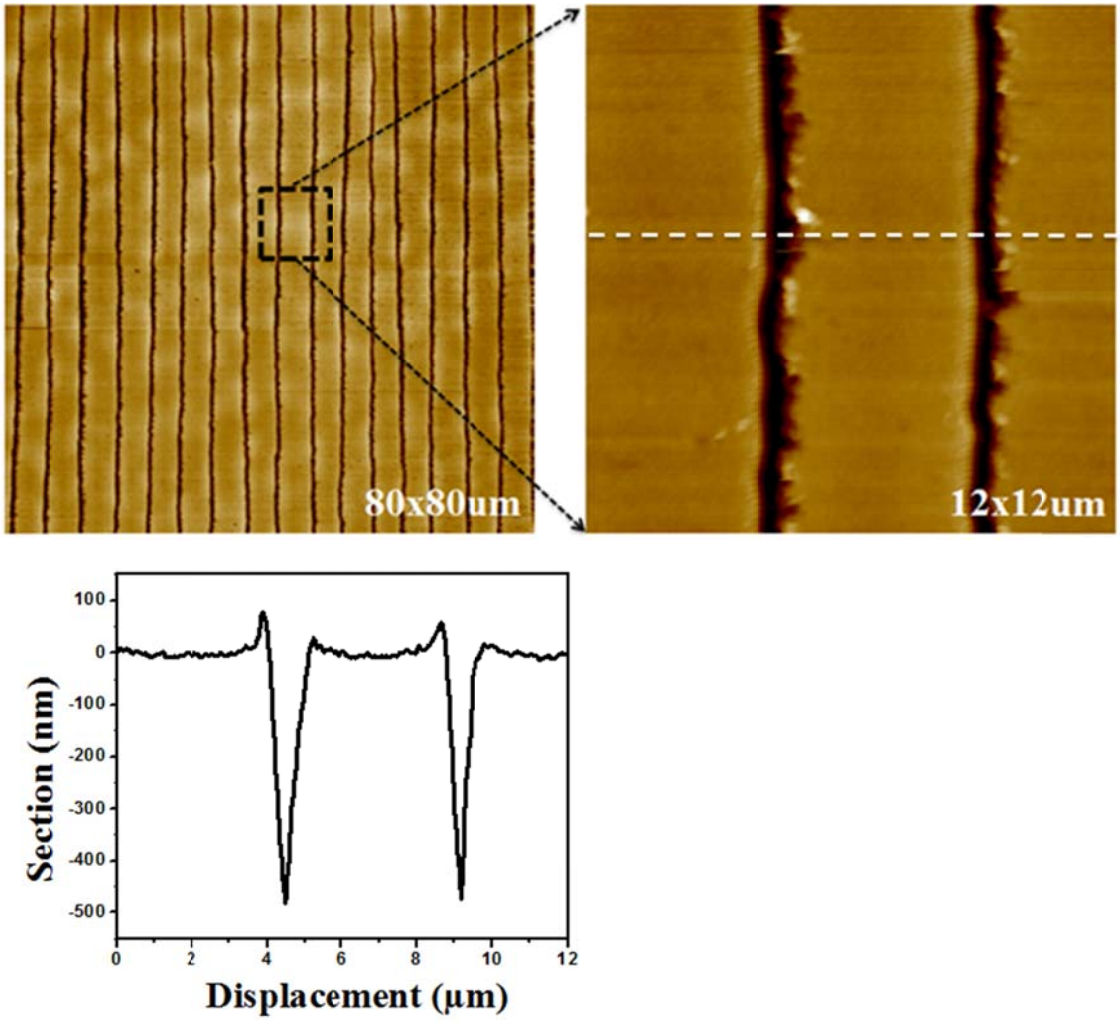

Figure S1. AFM images of PS latex channels. The cross-section of AFM height image reveals that these channels have a relatively depth of about 400nm. However, since the AFM tip may not reach the bottom of the cracks, this number is suspicious.

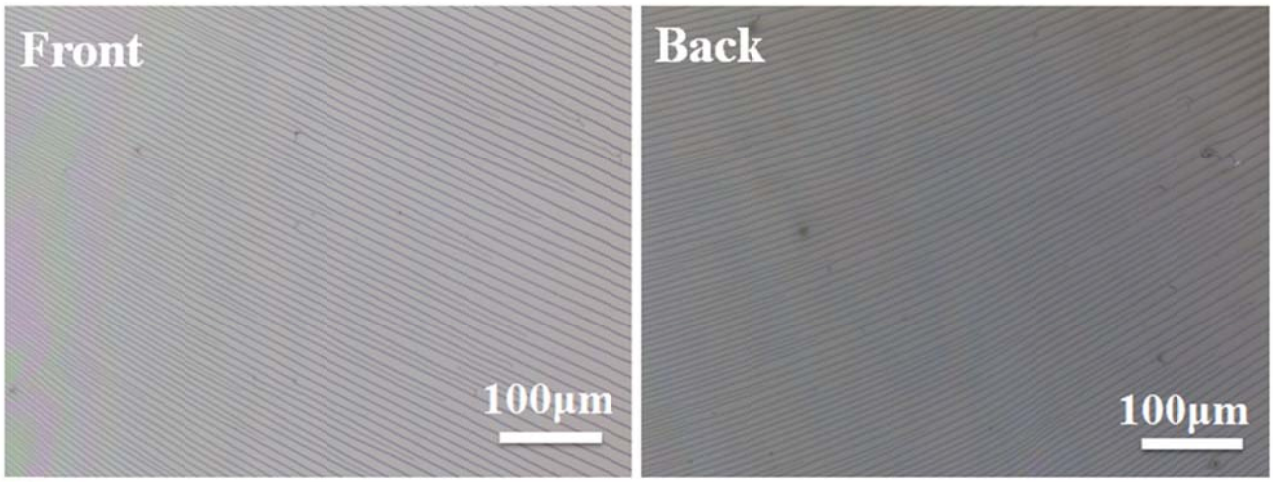

Figure S2. Optical micrograph images of front side and back side of PS latex particle channel pattern on the glass substrate, respectively. It indicates that the cracks penetrate the whole film, which means, the depth of the crack is equal to the local thickness of the thin film.

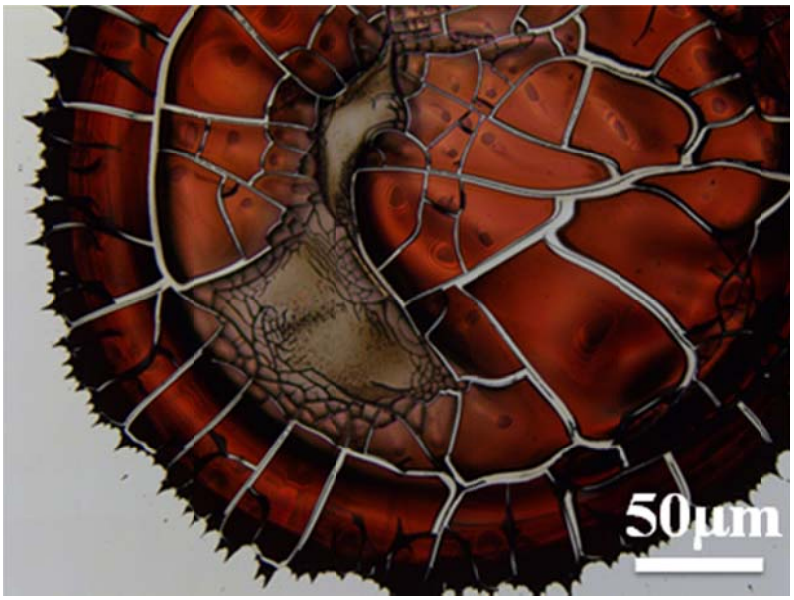

Figure S3. Optical micrograph images of PS latex particles deposited on the hydrophobic HMDS substrate. Highly concentrated ring pattern was observed due to the "coffee-ring" effect.

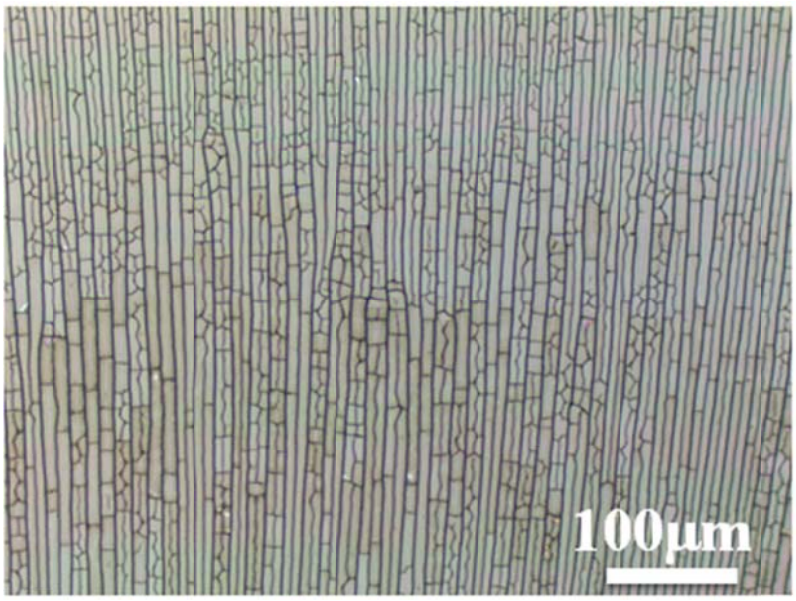

Figure S4. Optical micrograph images of PS latex particles conducted at room temperature. The channels are not well-ordered and secondary branching between cracks was observed.

References

1. Yabu, H.; Shimomura, M., *Langmuir* **2005,** *21* (5), 1709-1711.
2. Yabu, H.; Shimomura, M., *Adv. Funct. Mater.* **2005,** *15* (4), 575-581.
3. Erdogan, B.; Song, L.; Wilson, J. N.; Park, J. O.; Srinivasarao, M.; Bunz, U. H. F., *J. Am. Chem. Soc.* **2004,** *126* (12), 3678-3679.
4. Song, L.; Bly, R. K.; Wilson, J. N.; Bakbak, S.; Park, J. O.; Srinivasarao, M.; Bunz, U. H. F., *Adv. Mater.* **2004,** *16* (2), 115-118.
5. Jacobs, H. O.; Whitesides, G. M., *Science* **2001,** *291* (5509), 1763-1766.
6. Thurn-Albrecht, T.; Schotter, J.; Kästle, G. A.; Emley, N.; Shibauchi, T.; Krusin-Elbaum, L.; Guarini, K.; Black, C. T.; Tuominen, M. T.; Russell, T. P., *Science* **2000,** *290* (5499), 2126-2129.
7. Ostuni, E.; Chen, C. S.; Ingber, D. E.; Whitesides, G. M., *Langmuir.* **2001,** *17* (9), 2828-2834.
8. Whitesides, G. M.; Grzybowski, B., *Science* **2002,** *295* (5564), 2418-2421.
9. Philp, D.; Stoddart, J. F., *Angew. Chem. Int. Ed.* **1996,** *35* (11), 1155-1196.
10. Deegan, R. D.; Bakajin, O.; Dupont, T. F.; Huber, G.; Nagel, S. R.; Witten, T. A., *Nature* **1997,** *389* (6653), 827-829.
11. Deegan, R. D.; Bakajin, O.; Dupont, T. F.; Huber, G.; Nagel, S. R.; Witten, T. A., *Physical Review E* **2000,** *62* (1), 756-765.
12. Rabani, E.; Reichman, D. R.; Geissler, P. L.; Brus, L. E., *Nature* **2003,** *426* (6964), 271-274.
13. Byun, M.; Bowden, N. B.; Lin, Z., *Nano Lett.* **2010,** *10* (8), 3111-3117.
14. Byun, M.; Han, W.; Qiu, F.; Bowden, N. B.; Lin, Z., *Small* **2010,** *6* (20), 2250-2255.
15. Hong, S. W.; Jeong, W.; Ko, H.; Kessler, M. R.; Tsukruk, V. V.; Lin, Z. Q., *Adv. Funct. Mater.* **2008,** *18* (14), 2114-2122.
16. Hong, S. W.; Giri, S.; Lin, V. S. Y.; Lin, Z. Q., *Chem. Mater.* **2006,** *18* (22), 5164-5166.
17. Hong, S. W.; Wang, J.; Lin, Z. Q., *Angew. Chem. Int. Ed.* **2009,** *48* (44), 8356-8360.
18. Hong, S. W.; Xia, J. F.; Byun, M.; Zou, Q. Z.; Lin, Z. Q., *Macromolecules* **2007,** *40* (8), 2831-2836.
19. Hong, S. W.; Xia, J. F.; Lin, Z. Q., *Adv. Mater.* **2007,** *19* (10), 1413-+.
20. Hong, S. W.; Xu, J.; Xia, J. F.; Lin, Z. Q.; Qiu, F.; Yang, Y. L., *Chem. Mater.* **2005,** *17* (25), 6223-6226.
21. Xu, J.; Xia, J. F.; Lin, Z. Q., *Angew. Chem. Int. Ed.* **2007,** *46* (11), 1860-1863.
22. Xu, J.; Xia, J. F.; Hong, S. W.; Lin, Z. Q.; Qiu, F.; Yang, Y. L., *Phys. Rev. Lett.* **2006,** *96* (6).
23. Byun, M.; Laskowski, R. L.; He, M.; Qiu, F.; Jeffries-El, M.; Lin, Z. Q., *Soft Matter* **2009,** *5* (8), 1583-1586.
24. Hong, S. W.; Xu, J.; Lin, Z. Q., *Nano Lett.* **2006,** *6* (12), 2949-2954.
25. Lin, Z., *Journal of Polymer Science Part B: Polymer Physics* **2010,** *48* (24), 2552-2557.
26. Lin, Z. Q.; Granick, S., *J. Am. Chem. Soc.* **2005,** *127* (9), 2816-2817.
27. Kim, B. H.; Shin, D. O.; Jeong, S.-J.; Koo, C. M.; Jeon, S. C.; Hwang, W. J.; Lee, S.; Lee, M. G.; Kim, S. O., *Adv. Mater.* **2008,** *20*, 2303.
28. Han, W.; Byun, M.; Lin, Z., *Journal of Materials Chemistry* **2011,** *21* (42).

29. Yan, Q.; Gao, L.; Sharma, V.; Chiang, Y.-M.; Wong, C. C., *Langmuir.* **2008,** *24* (20), 11518-11522.
30. Ray, M. A.; Kim, H.; Jia, L., *Langmuir.* **2005,** *21* (11), 4786-4789.
31. Zhang, J.; Li, Y.; Zhang, X.; Yang, B., *Adv. Mater.* **2010,** *22* (38), 4249-4269.
32. Xia, Y.; Yin, Y.; Lu, Y.; McLellan, J., *Adv. Funct. Mater.* **2003,** *13* (12), 907-918.
33. Rycenga, M.; Camargo, P. H. C.; Xia, Y., *Soft Matter* **2009,** *5* (6).
34. Allain, C.; Limat, L., *Phys. Rev. Lett.* **1995,** *74* (15), 2981-2984.
35. Dufresne, E. R.; Corwin, E. I.; Greenblatt, N. A.; Ashmore, J.; Wang, D. Y.; Dinsmore, A. D.; Cheng, J. X.; Xie, X. S.; Hutchinson, J. W.; Weitz, D. A., *Phys. Rev. Lett.* **2003,** *91* (22), 224501.
36. Pauchard, L.; Adda-Bedia, M.; Allain, C.; Couder, Y., *Phys. Rev. E* **2003,** *67* (2), 027103.
37. Shorlin, K. A.; de Bruyn, J. R.; Graham, M.; Morris, S. W., *Phys. Rev. E* **2000,** *61* (6), 6950-6957.
38. Tirumkudulu, M. S.; Russel, W. B., *Langmuir.* **2005,** *21* (11), 4938-4948.
39. Johnson, K. L.; Kendall, K.; Roberts, A. D., *Proceedings of the Royal Society of London. A. Mathematical and Physical Sciences* **1971,** *324* (1558), 301-313.
40. Routh, A. F.; Russel, W. B., *Langmuir.* **1999,** *15* (22), 7762-7773.
41. Routh, A.; Russel, W.; Tang, J.; El-Aasser, M., *J. Coating. Technol.* **2001,** *73* (916), 41-48.
42. Skjeltorp, A. T.; Meakin, P., *Nature* **1988,** *335* (6189), 424-426.
43. Pauchard, L.; Parisse, F.; Allain, C., *Phys. Rev. E* **1999,** *59* (3), 3737-3740.
44. Colina, H.; Roux, S., *The European Physical Journal E: Soft Matter and Biological Physics* **2000,** *1* (2), 189-194.
45. Ngo, A. T.; Richardi, J.; Pileni, M. P., *Nano Lett.* **2008,** *8* (8), 2485-2489.
46. Néda, Z.; Leung, K. t.; Józsa, L.; Ravasz, M., *Phys. Rev. Lett.* **2002,** *88* (9), 095502.
47. Hull, D.; Caddock, B. D., *J. Mater. Sci.* **1999,** *34* (23), 5707-5720.
48. Smith, M. I.; Sharp, J. S., *Langmuir.* **2011,** *27* (13), 8009-8017.
49. Han, W.; Lin, Z., *Angew. Chem. Int. Ed.* **2012,** *51* (7), 1534-1546.

CHAPTER 10. SUMMARY AND OUTLOOK

This simple, cheap yet controllable and robust preparative strategy based on *CESA* of confined solutions has been used to assemble various soft and hard materials, including polymers, biomolecules, nanoparticles, etc., into spatially ordered structures with engineered properties and functionality over large surface areas. The confined geometry imparts a unique environment for exquisite control over the flow within the drying droplet, which in turn promotes the formation of highly regular complex structures. The scope of potential applications for such structures is vast, encompassing combinatorial chemistry, inkjet printing, electronics, optical coatings with selective or enhanced transmittance, optical materials, photonics, optoelectronics, energy conversion and storage, microfluidic devices, magnetic materials, information processing and data storage devices, multifunctional materials and devices, nanotechnology, sensors, DNA/RNA microarrays, gene mapping of DNA, high-throughput drug discovery, and biotechnology. Future work in this extraordinarily rich and exciting field will likely include the following directions: theory and simulations on deposition patterns, three dimensional assemblies, hierarchically ordered structures, and *in-situ* visualization on structural anisotropy and assembly/crystallization process.

The ability to predict the length scales of periodicity, height, and width as a functional of a wealth of variables noted in Section 3, and then compare them with experimental observations, is key to understanding the mechanisms of structure formation via *CESA* in confined geometries. Clearly, the rich deposition patterns resulted from controlled evaporation require aggressive theoretical studies and computer simulations to provide a basis for fully understanding the assembly process and identifying assembly pathways to produce controllable and consistent depositions in confined geometries. This remains challenging as the determination of the evaporation profile with these nonconventional boundary geometries, rather than a simple geometry (i.e., spherical cap in a sessile droplet) is one of the primary obstacles for rigorously solving the deposition problem.

It is noteworthy that 1D and 2D ordered structures can be readily achieved by current state-of-art *CESA* approaches. By contrast, effective methods to prepare 3D structures are rather few and limited in scope. In principle, it is highly desirable to create 3D structures for many potential applications such as photonic crystals, electronics, MEMS, and so forth. Innovative approaches based on extremely simple evaporative assembly to rationally craft 3D structured materials and devices should be developed. One route that may lead to 3D assembly and ordering is to exploit patterned substrates of proper dimensions and aspect ratios, either simply physically or both chemically and physically patterned, to guide the transport of solutes to fill the patterns or situate in the vicinity of patterns. Furthermore, 3D structures may also be realized by performing staged or sequential assembly processes in the confined geometry.

Hierarchical structures are common in both nature and technology. The combination of *CESA* in confined geometries with smaller-scale molecular self-assembly (e.g., block copolymers) leads to hierarchically ordered structures with specific synergetic properties that would offer new opportunities for many applications in the areas of electronics, optics, and energy storage. We note the formation of the block copolymer-based hierarchical ordered structures often requires subsequent thermal annealing or selective solvent vapor annealing to achieve the ordering and orientation of nanodomains within the microstructure formed by *CESA*. In this context, it is of great interest to explore powerful and efficient methods to develop hierarchically ordered functional structures with precisely controlled dimension, function, and topology in *one-step*, eliminating the annealing treatments. This is of particular importance when block copolymer/nanoparticle mixtures are used as tremendous challenges remain in the *simultaneous* controllable incorporation of nanoparticles within the target block and the ordering and orientation of block copolymer within the *CESA*-induced microscopic structures to provide functions and forms at multiple scales and locations. It is worth noting that ordered hierarchical assembly composed of nanocrystlas (e.g., quantum dots, QDs) as building blocks has been achieved, however the QDs within submicron-to-micron wide patterns are often randomly arranged or aggregated. Recent advances in the synthesis of nanocrystals have allowed the growth of a variety of nanocrystals of different size, shapes and functionality. A possible route to assembling nanocrystals into ordered arrays (i.e.,

superlattice) within structured patterns by *CESA* (i.e., forming hierarchically assembled nanocrystals over multiple length scales) will be to expedite the controlled evaporation process (i.e., faster solvent evaporation rate) by tailoring viable variables discussed in Section 3. Future development of hierarchically ordered structures with greater functionality and complexity via *CESA* will likely involve the concurrent multicomponent self-assembly by deliberately capitalizing on the aspects of shape of solutes, intermolecular interactions, induced conformation changes of solutes, tailored solute/substrate interactions, phase segregation, external fields, and so forth.

The liquid evaporates from the droplet edge in confined geometries should largely affect the flow of fluid inside the droplet. Thus, the determination of flow profiles in the droplet will help understand the solute transport and/or redistribution under different experimental conditions by monitoring fluorescent solutes using the tool of particle image velocimetry. To map the flow profiles inside an evaporating droplet containing polymer chains that may crystallize or self-assemble into nanostructures during the course of solvent evaporation, it is vital to utilize or develop novel optical characterization techniques that can offer reliable and appropriate measurement. For example, fluorescence dynamics technique images the trajectory of polymer chains, *in-situ* angular dependent polarized Raman spectroscopy monitors the Raman shift as a function of time to provide information on evolution of the chain alignment, and rapid scan time-resolved infrared spectroscopy studies the *in-situ* crystallization induced by evaporation. Moreover, it would be invaluable to exploit state-of-art spectroscopic techniques to probe the simultaneous occurrence of phase segregation, assembly, and crystallization in the proximity of the moving three-phase contact lines in *real time*, which may remain as an active area of exploration.

BIBLIOGRAPHY

1) W. Han and Z. Lin*, “Learning from “Coffee Ring”: Ordered Structures Enabled by Controlled Evaporative Self-Assembly”, *Angewandte Chemie International Edition*, 51, 1534 (2012).

2) W. Han**,** M. Byun and Z. Lin*, "Assembling and positioning latex nanoparticles via controlled evaporative self-assembly”, *Journal of Materials Chemistry*, 21, 16968 (2011).

3) W. Han**,** M. Byun, L. Zhao, J. Rzayev and Z. Lin*, "Controlled evaporative self-assembly of hierarchically structured bottlebrush block copolymer with nanochannels”, *Journal of Materials Chemistry*, 21, 14248 (2011)

4) W. Han, M. He and Z. Lin*, “Controlled evaporative self-assembly of all-conjugated polymer with enhanced electric conductivity” (to be submitted)

5) W. Han, M. Byun and Z. Lin*, “Hierarchical ordering of PS-b-P4VP micelles via controlled evaporative self-assembly” (to be submitted)

6) W. Han, C. Tang, and Z. Lin*, “Simple route to metal oxide stripes via controlled evaporative self-assembly” (to be submitted)

7) W. Han, and Z. Lin*, “Magnetic field assisted self-assembly of magnetic nanoparticles” (to be submitted)

8) W. Han, M. Byun, and Z. Lin*, “Hierarchical ordering of polymer stripes and Au film mixture wrinkles” (to be submitted)

9) W. Han, and Z. Lin*, “Swelling-induced hierarchical structures” (to be submitted)

10) W. Han, B. Li and Z. Lin*, “Spontaneous formation of well-ordered microchannels via evaporative self-assembly” (to be submitted)

11) X. Xin, J. Wang, W. Han, M. Ye and Z. Lin*, "Dye-sensitized solar cells based on a nanoparticle/nanotube bilayer structure and their equivalent circuit analysis", *Nanoscale*, 4, 964 (2012).

12) M. He, W. Han, J. Ge,Y. L. Yang, F. Qiu, and Z. Lin*, "High efficiency all-conjugated poly(3-alkylthiophene) diblock copolymer-based bulk heterojunction solar cells with controlled molecular organization and nanoscale morphology", *Energy & Environmental Science*, 4, 2894 (2011).

13) M. He, W. Han, J. Ge, W. Yu, Y. L. Yang, F. Qiu, and Z. Lin*, "Annealing effects on the photovoltaic performance of all-conjugated poly(3-alkylthiophene) diblock copolymer-based bulk heterojunction solar cells", *Nanoscale*, 3, 3159 (2011).

14) X. Xin, M. He, W. Han, and Z. Lin*****, "Low-cost CZTS counter electrodes for high-efficiency dye sensitized solar cells", *Angewandte Chemie International Edition*, 50, 11739 (2011). (Selected as Very Important Paper (VIP); featured by Nanowerk; featured on the Front Cover of *Angewandte Chemie International Edition*).

15) M. Byun, W. Han, B. Li, S. Hong, J. Cho, Q. Zou, and Z. Lin*, "Guided organization of λ-DNA into microring arrays from liquid capillary bridge", *Small* 12, 1641 (2011). (Featured by *Materials Views*).

16) M. Byun, W. Han, F. Qiu, Ned B. Bowden, and Z. Lin*, "Self-assembly: Hierarchically Ordered Structures Enabled by Controlled Evaporative Self-Assembly", *Small* 20, 2250 (2010). (Featured as featured on the Inside Front Cover of *Small*; featured on materials science news site MaterialsViews.com)

17) M. He, L. Zhao, J. Wang, W. Han, Y. L. Yang, F. Qiu, and Z. Lin*, "Self-assembly of all-conjugated poly(3-alkylthiophene) diblock copolymer nanostructures from mixed selective solvents", *ACS Nano,* 4, 3241, (2010). (Featured as an In Nano selection).

18) B. Li, W. Han, and Z. Lin*, "Macroscopic Highly Ordered DNA Spokes Using Controlled Evaporative Self-assembly" (to be submitted)

ACKNOWLEDGEMENTS

I would like to take this opportunity to express my thanks to those who helped me with various aspects of conducting research and the writing of this thesis. First and foremost, Dr. Zhiqun Lin, as my primary supervisor, for his academic advice and guidance, patience and support throughout the whole research works and the writing of this thesis. His insights and words of encouragement have often raised me up, so I renewed my hopes and tided over big adversity for completing my graduate education.

I would also like to appreciate all the committee members, Prof. Surya K. Mallapragada, Prof. Sumit Chaudhary, Prof. Xinwei Wang, and Dr. Malika Jeffries-EL, for their efforts and contributions to this work.

I would like to give a special thanks to all group members; Dr. Xinchang Pang, Dr. Myunghwan Byun, Dr. Jun Wang, Dr. Lei Zhao, Dr. Ming He, Xukai Xin, Bo Li, Jaehan Jung and Chaowei Feng.

I would additionally like to thank my wife Lulu Chen and my parents for their support on my research and my life over these years.